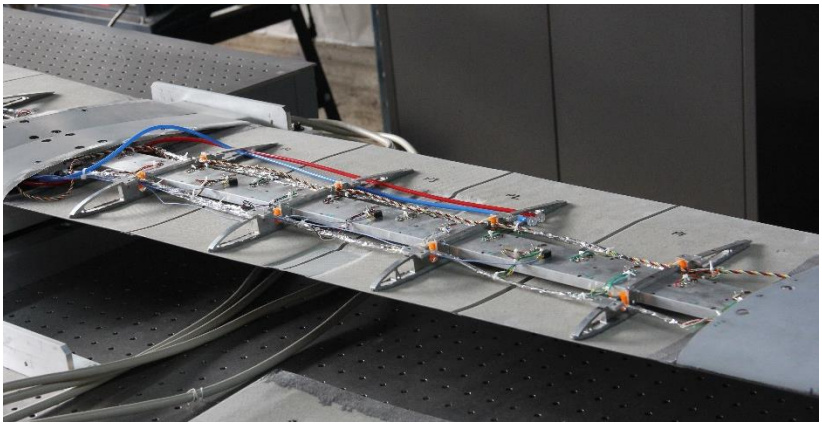

Measurement of Aeroelastic Wing Deflections on a Remotely Piloted Aircraft using Modal Strain Shapes

by

Stephen Daniel Wilfred Warwick
B.Eng., University of Victoria, 2012

A Thesis Submitted in Partial Fulfillment
of the Requirements for the Degree of

MASTER OF APPLIED SCIENCE

in the Department of Mechanical Engineering

Measurement of Aeroelastic Wing Deflections on a Remotely Piloted Aircraft using Modal Strain Shapes

by

Stephen Daniel Wilfred Warwick
B.Eng., University of Victoria, 2012

Supervisory Committee

Dr. Afzal Suleman, Supervisor
Department of Mechanical Engineering

Dr. Curran Crawford, Departmental Member
Department of Mechanical Engineering

Abstract

The aerospace industry endeavours to improve modern aircraft capabilities in efficiency, endurance, and comfort. One means of achieving these goals is through new enhancements in aerodynamics. Increased wing aspect ratio is an example of further improving efficiency. However, this comes with new challenges including possibly adverse aero-elastic and aero-servo-elastic (ASE) phenomena. New computational methods and tools are emerging and there is a need for experimental data for validation. University of Victoria's Centre for Aerospace Research (UVic CfAR) set out to design a 20kg ASE demonstrator using a remotely piloted aircraft (RPA). This aircraft was designed with the intent of exploring coupling between aero-elastic modes including coupling between the short period aerodynamic mode and the first out-of-plane elastic mode of the wing. This thesis discuses the implementation of instrumentation designed and integrated into the ASE RPA demonstrator to monitor the deformation of the elastic wing in-flight.

A strain based measurement technique was selected for integration into the ASE aircraft. This choice was made for several reasons including its reliability regardless of outdoor lighting, relatively lightweight processing requirements for real time applications, and suitable sampling bandwidth. To compute the wing deformation from strain, a method, sometimes referred to as strain pattern analysis (SPA), utilizing linear combinations of reference modal shapes fit against the measured strain, was used. Although this method is not new, to the author's knowledge, it is the first practical application to a reduced scale RPA demonstrator.

The deformation measurement system was validated against a series of distributed static load tests on the ground. Distributed load cases along the wing demonstrated good out-of-plane measurement performance. A case where only load is applied near the root of the wing resulted in the largest error in part as the mode shapes generated are less suited to approximate the resulting shape. In general errors in out-of-plane displacement at the end of the flexible wing portion can be expected to be less than 5%. The displacement at the tip of the wing can be as great as 11% for the left wing whereas the right wing is 4.7%. This suggest an asymmetry between the left and right wings requiring specifically tuned FE models for each to achieve best results. Twist angles presented in tests were relatively small for accurate comparison against the reference measurement, which was relatively noisy. Generally, the deformation measurement by SPA technique followed the same twist behaviours as the reference. A twist case, unlikely to be seen in flight, provided some insight into twist measurement robustness.

The work presented is merely a small step forward with many opportunities for further research. There is room for improvement of the FE model used to generate the mode shapes in the strain pattern analysis. Initial efforts focused on the flexible spar

portion of the wing. With more work improvements could be achieved for the estimation of the rigid wing. Additionally, there was some asymmetry between each wing semi-span, and with some focus on the left wing its results could be improved to at least match that of the right wing. A real-time implementation was not completed and would be particularly interesting for use as feedback for flight control. Study of load alleviation techniques may benefit. Another topic of study is the combination of this method with other measurements, such as accelerometers, to provide improved performance state estimation through sensor fusion.

Contents

List of Figures

List of Tables

List of Nomenclature

$[i_s]$	=	Strain Mode Shape
$[o_d]$	=	Displacement Mode Shape
{D}	=	Displacement Vector
{q}	=	Modal Coordinate Vector
{S}	=	Vector of Strain Values
m	=	Number of Mode Shapes
ADC	=	Analogue to Digital Conversion
AR	=	Aspect-Ratio
ASE	=	Aero-servo-elastic
CAE	=	Computer Aided Engineering
CfAR	=	Centre for Aerospace Research
CLAS	=	Conformal Load Bearing Antenna Structure
CMM	=	Coordinate Measurement Machine
COTS	=	Commercial Off the Shelf
DOF	=	Degree of Freedom
EMA	=	Experimental Modal Analysis
FBG	=	Fibre Bragg Grating
FDMS	=	Flight Deflection Measurement System
FE	=	Finite Element
FOSS	=	Fibre Optic Sensing System
FPGA	=	Field Programmable Gate Array
FRF	=	Frequency Response Function
GVT	=	Ground Vibration Testing
HALE	=	High Altitude Long Endurance
LED	=	Light Emitting Diode
MAC	=	Modal Assurance Criterion
ONERA	=	Office National d'Études et Recherche Aérospatiales
RPA	=	Remotely Piloted Aircraft
RPAS	=	Remotely Piloted Aircraft System
SEAMAC	=	Sensor Elimination using MAC
SIMO	=	Single Input Multiple Output
SISO	=	Single Input Single Output
SPA	=	Strain Pattern Analysis
TC	=	Transport Canada
UAV	=	Unmanned Autonomous Vehicle
UVic	=	University of Victoria
VMD	=	Videogrammetric Model Deformation

Acknowledgements

I would like to acknowledge all the individuals who supported me in completing this Thesis. Much has happened in the last several years and completion of this thesis was only possible as a result of the contributions and support from many people. I will do my best to express my thanks and acknowledge everyone here. To begin, I would like to thank Professor Afzal Suleman for providing this opportunity. I am grateful for the trust and support (logistical and technical) afforded me while offering me this fascinating opportunity to grow, and discover new things in a variety of topics while engaging with so many wonderful people.

Thank you to Dr. Jenner Richards, for providing technical guidance and support throughout the project. Willem, the mechanical design lead and chief test pilot for the ASE project provided many hours of discussion in a variety of topics, and a spare pair of eyes to review my work, while patiently accommodating numerous requests to make this work possible. Likewise, Mario, who did a large amount of simulation and modelling in the ASE project, worked with me to accommodate this work in his efforts. Mario also spent some of his precious free time installing strain gauges. Peter provided many hours walking me through electrical design and assisted with the fabrication, assembly, and testing of the delicate strain instrumentation. Josh provided many hours assisting in questions relating to CAD surface modelling, assisted applying strain gauges, ground testing, and flight testing. Brayden, and Ben, my thanks for many hours installing strain gauges (perhaps a common theme, hundreds of precise gauges were installed in this project). Eldad, thank you for your guidance in helping plan this project. I wish to thank Justin for his help developing and testing the real-time and FPGA Labview software for the flight data recorder. Also, Dr. Maxym Rukosuyev thank you for your kind introduction to Professor Suleman and Dr. Richards.

The ground vibration testing (GVT) of this project was completed with a significant amount of assistance from Nuno Mocho. Nuno came in on weekends and spent a great deal of time in the preparation and completion of GVT (with which he completed his masters in GVT of a small remotely piloted aircraft). João Mara and Ana Meinicke, thank you for coming to visit from Embraer and share your insight and experience with us in the GVT of this aircraft. Jury Mura provided assistance preparing the second set of static load tests with inclusion of higher fidelity metrology reference displacement data (with which he completed his Masters focusing on single camera videogrammetry on a small remotely piloted aircraft). José Carregado, provided guidance in the use of the FEMtools model updating environment.

I wish to extend my thanks to those I have not directly mentioned here but who work (past and present) just as hard, if not harder than myself, at the University of Victoria's Centre for Aerospace Research (UVic CfAR). Thank you for your support and having

made this such an interesting and exciting place to study and work. I sincerely appreciate your camaraderie.

Last, but not least, I must provide acknowledgement to my family and friends who provided the solid foundation of my support. Mom and Dad always made themselves available to listen, provided encouragement, and never ending support. My partner, Ali, provided emotional support, encouragement, and a great deal of patience. I would have been lost without you.

Dedication

I dedicate this work to my family. Thank you for all your support from start, present, and beyond. I would not be here without you. Love, Stephen

Chapter 1 - INTRODUCTION

1.1 INTRODUCTION

Current aero-elastic computational codes are relatively new and their ability to predict aeroelastic phenomena in high aspect ratio wings requires validation. There is a limited amount of data suitable for such validation. To enable further development there is a need for experimental data sets demonstrating aeroelastic behaviours in-flight.

University of Victoria's Centre for Aerospace Research (UVic CfAR) set out to design and build a 20kg remotely piloted aero servo elastic (ASE) flight test vehicle to generate a database of aero-servo-elastic responses to validate analytical aeroelastic models. An existing remotely piloted aircraft (RPA), the QT1, with conventional 3.4m wingspan rigid wings was used as the basis for the work. The rigid wings were replaced with a set of custom designed, flexible wings, and the aircraft was designated QT1.3. The flexible wings were designed to exhibit a predetermined, high degree of coupling between the first elastic bending mode and the short period aerodynamic mode of the aircraft.

A research objective of this work was to understand the wing deformation as a result of aerodynamic forces interacting with the structural elasticity. To enable this investigation a method to measure the wing shape while flying was necessary.

The focus of this thesis is the design, integration, and operation of a system to measure the displacement shape of the wing on the ASE flexible aircraft QT1.3.

1.2 UNIVERSITY OF VICTORIA CENTRE FOR AEROSPACE RESEARCH

This project was completed in collaboration with the University of Victoria's (UVic) Centre for Aerospace Research (CfAR). UVic is on the forefront of aerospace research where CfAR specializes in the application of remotely piloted aircraft systems (RPAS).

RPAS refers inclusively to equipment for the ground station, communications, on-board payloads, autopilots, and airframe of the remotely piloted aircraft (RPA). Formerly referred to as unmanned aerial systems (UAS) or unmanned aerial vehicles (UAV), public perception, international trends, and movements towards a gender inclusive industry, Transport Canada (TC) has formally adopted the term RPAS for legal and regulatory purposes as of 2019. In Canada the term "drone" is still used for public communication.

CfAR has partnered with different organizations and companies including but not limited to Airbus, Boeing, Bombardier, Embraer, Mitsubishi, and Defense Research and

Development Canada (DRDC). CfAR has provided a wide range of research assistance from theoretical models and conceptual design to experimental prototypes including operational testing.

UVic CfAR has specialized in the experimental testing of unconventional aircraft through the use of RPA. Some configurations include, high aspect ratio sailplanes, joined wing aircraft, blended bodies, and wing in ground effect vehicles. One example is the experimental investigation of Boeing's proposed Joined Wing "SensorCraft" (JWSC) using flexible reduced scale flight test vehicles. The 3m wingspan flight test vehicle (FTV) of the JWSC prior to its first flight over the Saanich Peninsula is shown in Figure 1.

Figure 1: UVic CfAR 3m JWSC scaled flight test RPA

Another example includes the use of a high aspect ratio winged sailplane with a wing span of 3.4metres and a mass under 25KG for the experimental exploration of highly aero-elastic wings, seen in Figure 2. The goal of the aero-servo-elastic (ASE) demonstrator was to take these results and use them for validation of aero-elastic computational frameworks. The wing deflection monitoring system implemented in this project is the basis of the author's thesis application.

Figure 2: ASE QT1.3 RPA equipped with flexible wing.

1.3 MOTIVATION

The pursuit of more efficient platforms has been collectively agreed as an important objective for the aerospace industry to reduce cost and environmental impact. Different methods are being investigated to make these improvements including new materials (such as composites), better propulsion (improved engine efficiencies and new hybrid-electric propulsion [1], [2]) , and enhanced aerodynamics.

Growth in the civil aerospace sector (passenger, and transport) is pushing innovation. From 1999 to 2018 the number of passengers carried by airlines has increased from roughly 1.67 billion to 4.23 billion. It is expected that the number of passengers who travel by air will increase to roughly 8.2 billion worldwide by 2037 [3]. Growth is expected worldwide with largest changes in China and India. In North America the FAA expects air transportation to increase by 25% from 2019 to 2039 [4].To meet the expected growth airlines will need to purchase over 40,000 new aircraft over the next 20 years [5].

Environmental factors including, noise, air pollution, and climate change are well documented and described in literature [6]. These factors play an important role in growth of civil aviation. In the year 2000, an estimated 677 megatons of carbon dioxide are estimated to have been emitted by the aviation sector, which is was ~2-3% of that generated by humanity that year [7]. A reminder that in the conventional fuel combustion process the following greenhouse emissions are generated; carbon dioxide (CO_2), nitrogen oxides (NO_X), as well as wasted unburned hydrocarbons.

Commercial aviation is not only motivated by environmental objectives. Fuel burned transporting passengers and cargo represents between roughly 20-30% of the direct operating cost (DOC) for airlines [8]. Consider a drag reduction of 1% can lead to decrease in DOC of 0.2%. Other alternate trade-offs which correspond to a 1% drag reduction could be 1.6tons of operating weight or 10 passengers for large transport aircraft [9].

One way of improving aerodynamics is through the aspect ratio of wings. Looking at current commercial transport aircraft one can observe that their wings aspect ratios have been steadily increasing. This may be attributed to the reduction in induced drag resulting in greater lift-to-drag and longer range flight [10]. Induced drag normally makes for roughly 43% of the overall drag in large transport aircraft [11].There are gains to be expected for lower speeds as well. Higher aspect ratio wing's benefits are not limited to more conventional planar wing aircraft but also lends to other configurations, such as but not limited to a joined wing [12] or a blended wing body. Several example next generation concept aircraft with high aspect ratio wings are shown in Figure 3.

Figure 3: A joined wing concept from NASA and Lockheed Martin (Top Left) [13]. The Boeing SUGAR high aspect ratio truss braced wing (Top Right) [14]. The Boeing blended wing body concept aircraft (Bottom Left) [15]. The NASA, MIT, and Aurora flight sciences D8 concept aircraft with double fuselage configuration and high aspect ratio wings (Bottom Right).

Unfortunately, although potentially beneficial, there are issues with the design of high aspect ratio wings. These wings must manage higher stress levels at their root, and there tends to be significantly higher structural flexibility. Higher flexibility will result in greater deflections. This change in shape may affect dynamic behaviour (modal properties) and consequently the aeroelastic behaviour. This can result in aeroelastic instabilities at lower speeds than a comparable stiff wing [16].

High aspect ratio wing aircraft designs have pushed the boundaries of traditional linear methods and are no longer suitable to model non-linear behaviour. Unexpected aeroelastic phenomena can occur in flexible structures which are not captured in existing models [16]. An example of requirement for a better aeroelastic model was the NASA Helios Prototype, a high-altitude long-endurance (HALE) solar-electric HEP ultra-light flying wing RPA developed in the late 1990s and early 2000s, shown in Figure 4. The aircraft was lost after breaking up in flight, highlighting the need for more robust tools in the design and operation of such designs [17].

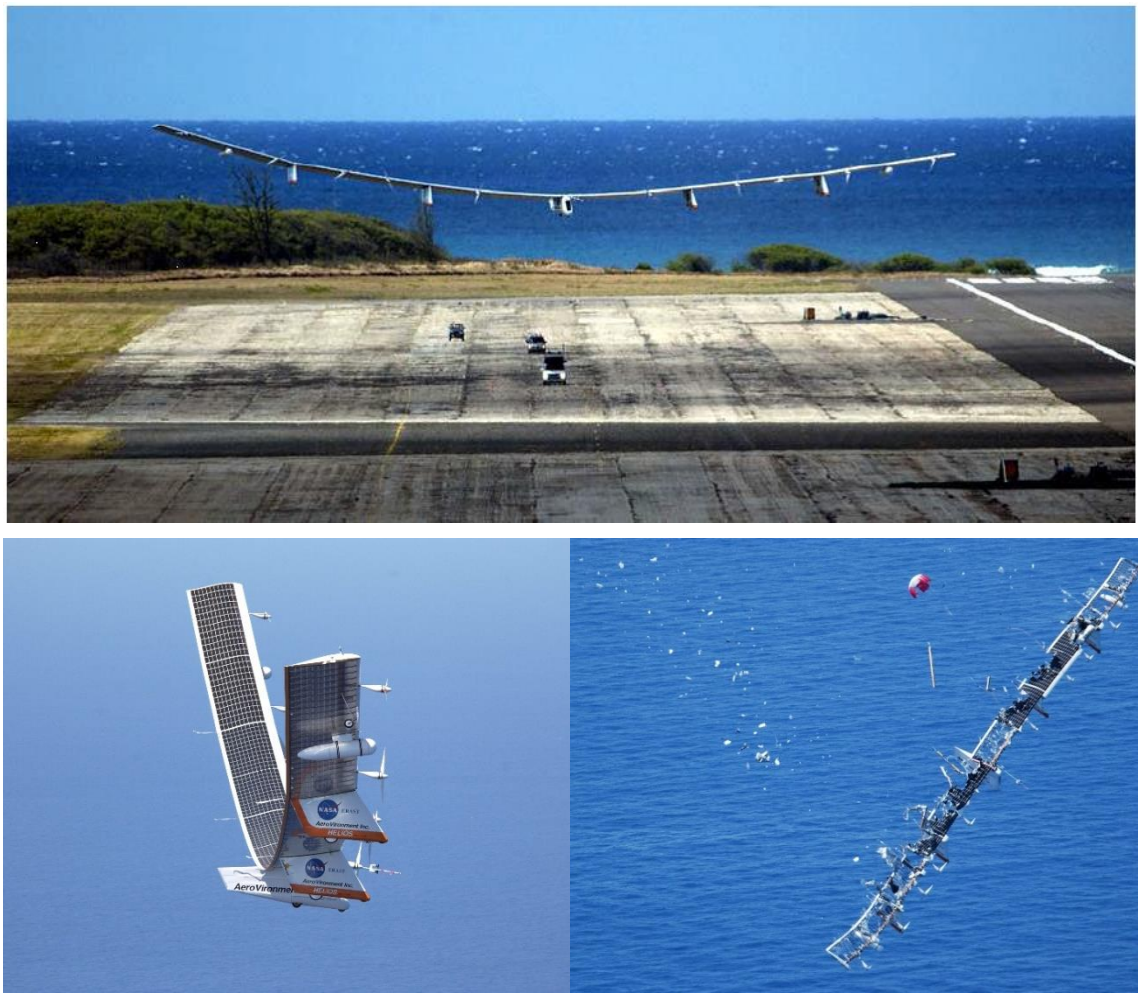

Figure 4: The NASA Helios project in collaboration with AeroVironment built a high altitude high endurance aircraft prototype powered by solar electric propulsion (Top). NASA Helios prototype before (Left) and after (Right) in-flight breakup in 2003 [17].

Because current aero-elastic computational codes are relatively new, their ability to predict full-scale aeroelastic performance of aircraft requires validation. There is a need for experimental data sets demonstrating the behaviour of elastic aircraft in-flight for tuning such models [12], [18], [19]. In response to this need, optical and strain methods have been employed for use in both wind tunnels, on the ground, and in flight testing to provide deflection information.

The motivation of the author's research was to develop and implement a method to measure the displacement of a small RPA wing in flight. This was a sub-project supporting an effort focused on gathering data sets for validation of aeroelastic frameworks. Small scale RPAs provide a low cost and effective means to investigate aero-elasticity and aero-servo-elasticity for validation of existing computational models [20]. This method of displacement measurement is unique in that it was a mix of

technologies which allowed deployment on a small RPA (less than 25KG). This method may thus be prototyped in small scale at a low risk while also being able to be scaled up if the need arises.

New opportunities for application of structural shape monitoring exist further to aeroelastic experimentation. Gust loads on flexible aircraft resulting in degraded flying qualities, ride comfort, and increased structural loads could be potentially alleviated by means of active suppression [21]. Availability of feedback regarding the deformation shape of an aircraft's wing would provide an opportunity as means of feedback for control.

Additional to use as feedback for aeroelastic research and control, in-flight displacement measurement can potentially benefit antennas in aerospace. Conformal and structure integrated antennas have a critical importance in the near future with regard to airborne wireless applications including, communication, navigation and radar, Intelligence, surveillance and reconnaissance systems. Conventional antenna design varies from small-sized fairings and blades, in which dipoles or monopoles are encapsulated, to large aperture antennas such as the Multi-role Electronically Scanned Array (MESA) mounted on the top of aircraft like the Boeing 737 Early Warning Aircraft [22]. These current generation, parasitic (non-load bearing) antennas are limited in size and installation location by vehicle airframe and flight characteristics. Typical mission scope is adversely impacted by weight, aerodynamic drag, reduced electrical/structural efficiency and overall RF performance [23]. Structure integrated and conformal antennas on the other hand are part of the aircraft structure and are integrated into the skin greatly improving antenna mission performance. Another area of interest is in Conformal Load Bearing Antenna Structures (CLAS). Using this multifunctional CLAS structure contributes to a significant weight savings by functioning as an antenna array and structural support. The antenna structure provides structural support by using several different materials with known strengths and mechanical properties to develop a structure that provides support for the specific loads that it will encounter, as well as provide the outer skin of the aircraft antenna locations. One such example was recently investigated for use on the United States Air Force Sensorcraft concept [24]. This application saw the proposed use of a three-layer configuration of Astroquartz, Honeycomb, and Graphite Epoxy (Figure 5). The Astroquartz is an electromagnetically transparent material allowing the radar to transmit and receive, as well as act as the outer shell of the skin, providing protection from the environment and external factors. Inside of this is the Honeycomb Core. This layer serves to house the radar antennas and acts to carry much of the compressive load. The core layer also serves to provide reinforcement against panel buckling. The bottom layer is the Graphite Epoxy layer which serves to bear the majority of the load incurred on the CLAS. The radar components are also mounted onto this layer [25].

There does exist a trade-off however. Array antennas, which could be integrated onto structures of aircraft and Unmanned Aerial Vehicles (UAVs), are subject to unsteady aerodynamic loads. Mechanical forces and aerodynamic loads would cause deformation of the antenna supporting structure as a consequence. This introduces the challenge of an antenna with phased array elements which changes positions and orientations. The relative phases of the respective signals feeding the antennas would vary, and as a consequence the antenna radiation pattern would be affected: the main beam direction can change and the beam width and/or side lobe levels could increase. The influence of deformations and vibrations would be most significant on array antennas which are large in terms of wavelength (high gain antennas). However, these negative effects could be suppressed by means of synthetic beam forming [25]. To this end the phase differences between the antenna elements on the deformed and undistorted structure would have to be determined instantaneously. This requires the measurement of out-of-plane variations by appropriate sensors.

1.4 BACKGROUND

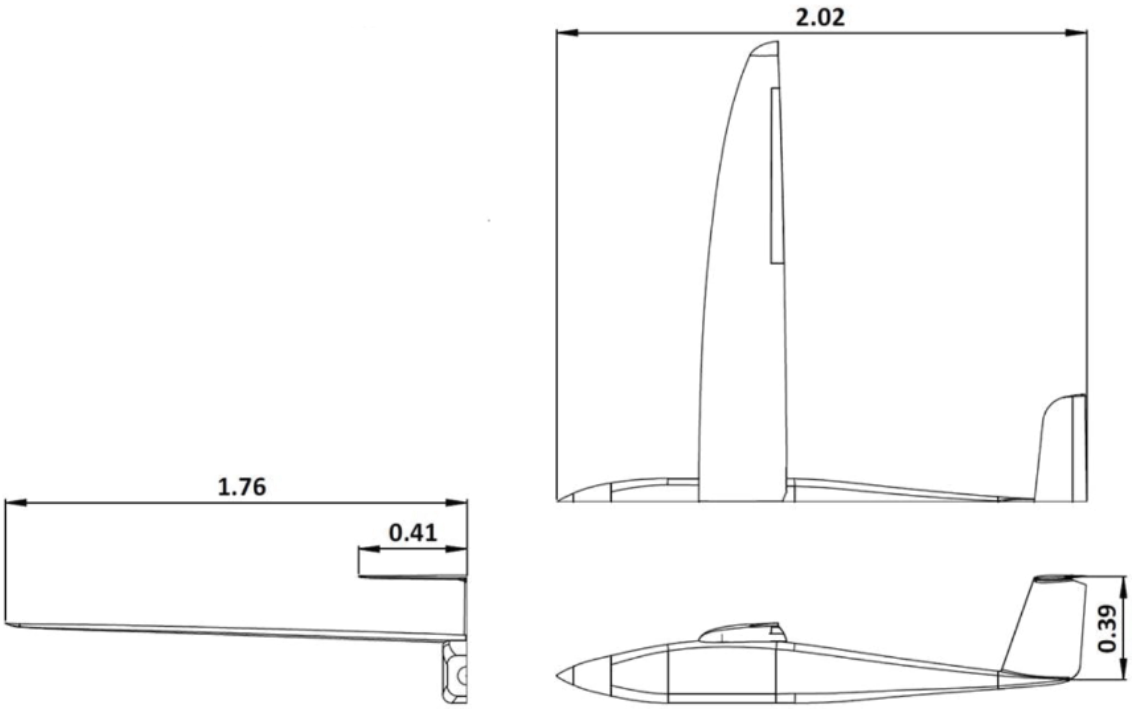

Figure 5: 3 view drawing of baseline QT 1 RPA.

The primary goal of this project was to generate experimental data sets for aeroelastic and aeroservoelastic analysis and validation. The method was to take an existing conventional planar wing sailplane RPA with a relatively high aspect ratio wing

and modify it to capture desired aeroelastic phenomena with a comparable pseudo-rigid baseline to compare against. The flight test vehicle (FTV) would be ground tested, including structural dynamics with which tools could be validated against. A flight testing regime would provide the fundamental validation elements for the program, with a pseudo rigid wing, and a flexible wing design.

Figure 6: QT 1.1 Aircraft in base configuration

The proposed RPA for the project, the QT1 (seen in Figure 5 and Figure 6), was selected for this project as it had already been designed, built and flown at UVic CfAR. General baseline specifications are listed in Table 1.

Table 1: QT 1 baseline specifications

Wing Span	2.93 m
Length	1.9 m
Wing Area	1.03 m^3
Propulsion	3KW DC Brushless
TO Weight	15-22KG
Altitude Max	122 m (Limited by TC at time of testing)
Stall/Cruise/Max Speed	45/75/150 km/hr
Control Method	Manual RC, Autopilot Assist, Autonomous Waypoint Tracking
Take-Off/Landing Method	Manual, Autonomous, Catapult Assist
Landing Type	Manual, Autonomous, Belly Landing
Max Flight Time	2 Hours (depends on Configuration)
Construction	Composite (Carbon, Fibre-Glass)

The baseline aircraft was retrofitted with an instrumentation system to collect applicable in-flight measurements. Note that to reduce cost, the existing wings outer mold design (OML) for the pseudo rigid configuration remained unchanged and instrumentation designed for the flexible aircraft was not installed in the baseline wings including strain gauges, and wing mounted accelerometers.

The flexible wing aircraft was equipped with strain gauges and a method was employed to estimate the static and dynamic shape of the wing in flight.

1.5 Thesis Outline

Chapter 1 - Introduction

The introduction section of this thesis informs on the background and motivation behind the ASE project. First a short summary of UVic CfAR including past and present projects with focus around sub-scale low risk models for validation of theoretical models. Aerospace industry motivations are touched upon with illustration of several growing sectors driving a need to for more efficient platforms to reduce emissions, operational costs, improve comfort, and achieve greater safety. It is suggested that efficiency can be heightened through means of enhanced aerodynamics such as higher aspect ratio wings. Current aero-elastic and aero-servo-elastic solvers are still relatively

new and there is a need for ASE data for validation. UVic CfAR has designed a flexible wing ASE demonstrator based on an existing platform the QT1 aircraft. Part of the ASE demonstrator's requirements is the ability to monitor wing shape in-flight, the focus of this thesis.

Chapter 2 - State of the Art

The State of the Art section starts with a review of methods used in the past and present to monitor the shape of aircraft wings. An emphasis is made for techniques which can be applied in flight testing and not just for use in static or wind tunnels. A strain based technique is selected for integration into the ASE aircraft due to reliability regardless of outdoor lighting. The selected method, sometimes referred to as strain pattern analysis (SPA) utilizes linear combinations of reference modal shapes to identify wing deformation. Methods for practical strain measurement are reviewed, primarily conventional resistive foil strain gauge technology as well as the relatively new fibre optic sensing system (FOSS) technology Fibre Bragg Gratings (FBG). The SPA method used here uses modal shapes of the wing for shape estimation, which leads to a short summary in structural dynamics, numerical modelling, and experimental measurement techniques applied in this project.

Chapter 3 - Design, Modelling, and Simulation

Design behind the implementation is discussed here. First a general method for workflow is discussed. Here the idea of building a FE structural model to estimate numerical solutions to use as the reference modal patterns, determine sensor locations, and select appropriate mode shapes is commented on. Next the FE model design is discussed. A brief summary of the acquisition hardware used in the aircraft with emphasis regarding strain measurement. Some of the challenges and solutions found using a COTS programmable cRIO real-time computer and FPGA target from National Instruments are presented. Gauge locations, bridge type, and orientation selection importance is discussed and considerations listed. Simulations of the proposed system using static strain and displacement solutions resulting from hypothetical load cases to be completed in following chapters are shared verifying the system will function as intended.

Chapter 4 – Experimental Testing

Experimental tests conducted on the built test articles are discussed. Ground tests included static load tests, ground vibration testing, component wise mass measurement, and flight testing. The FE model updating is incorporated in this section following discussion of all ground tests, as these results are used to validate and drive updates of the FE model to validate and improve deformation measurement capability. FE model updates, which include, component mass and inertia updates, grouped element stiffness updates were correlated against static tests, and inertia and stiffness

updates correlated against experimentally measured modal peak frequencies and modal shapes. Flight testing comments on system set up to measure strains for calculating wing deformation.

Chapter 5 – Deformation Measurement Results

Deformation measurement by SPA is investigated in this section. Here a series of static load tests and mode shapes from the updated FE model from Chapter 4 are inspected. Deformation out-of-plane in the wings is observed for distributed load cases, or cases where the load is applied to the rigid wing section when compared against reference deformation measurement taken by metrology grade optical CMM. Data sets taken do not show large twists applied to wing and reference information is relatively noisy but wing demonstrates tracking of wing twist in the instrumented sections. The modal least squares fits, although adequate for the intended purpose, leave room for improvement. Tuning of as built sensor locations, orientation, better suited mode/reference shapes as well as possibly scheduling different shapes for different loads to better adapt to large deflection non-linearities are suggested for future improvement.

Chapter 6 – Conclusions and Recommendations

In this section the achievements of this project are discussed. A critical summary of results is concluded on. Additionally, recommendations for future follow on work are suggested.

1.6 COLLABORATION

The author would like to acknowledge the support provided by the NSERC Discovery grant. The research work was carried out in the framework of a research collaboration with Embraer S.A. (Brazil) and Quaternion Engineering.

Chapter 2 - State of the Art

2.1 Deformation Measurement Methods

Deformation measurements are in reference to the change in shape of an aircraft generally as a result to aerodynamic loads. Here deformation is generally in reference to the change of shape of an aircraft's wings due to these loads, unless otherwise specified. Note also in this context deformation and displacement are sometimes used interchangeably, as is seen in literature concerning this topic. Deformation measurement techniques are generally not routine in commercial aircraft. These methods are saved for experimental purposes, although, there are potential benefits including but not limited to applications in aerodynamics, flight control, structural health monitoring, and other payloads benefits.

2.1.1 Optical Deformation Methods

There are several noteworthy optical methods which have been successfully applied to larger aircraft and wind tunnel models. Videogrammetric model deformation (VMD) has been explored at NASA and UVic CfAR for both ground testing [26], [27], and flight testing [28].

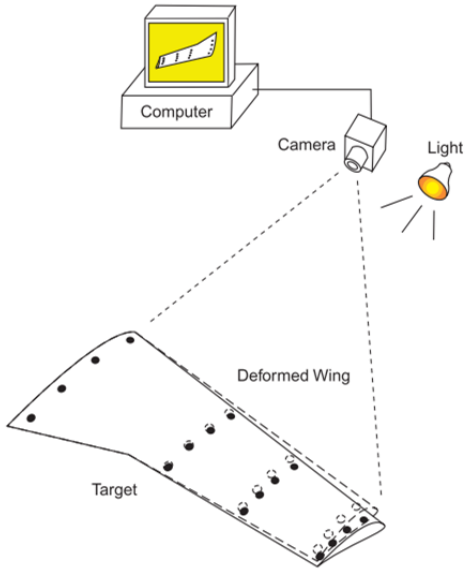

Figure 7: Single camera VMD camera system schematic [29]

Figure 8: VMD tracking of bending and twist deformation of tail in CfAR flexible ASE JWSC project.

This technique may be used for the measurement of aeroelastic deformation of an aircraft. VMD, using close-range photogrammetry principles, may be used to estimate the spatial coordinates of targets on a model's surface from the analysis of target centroids in the image frames captured by a camera. VMD exploits the collinearity equations from the photogrammetry ideal pinhole camera model to transform a targets pixel position to a relevant 3D coordinate system.

Variations of this technique exist with single camera capture and multiple camera capture variations. The single camera or single view method has the caveat requiring that one of the target coordinates must be known. Multiple camera views can mitigate this with sufficient perspective to allow 3D spatial intersection to solve the remaining coordinate.

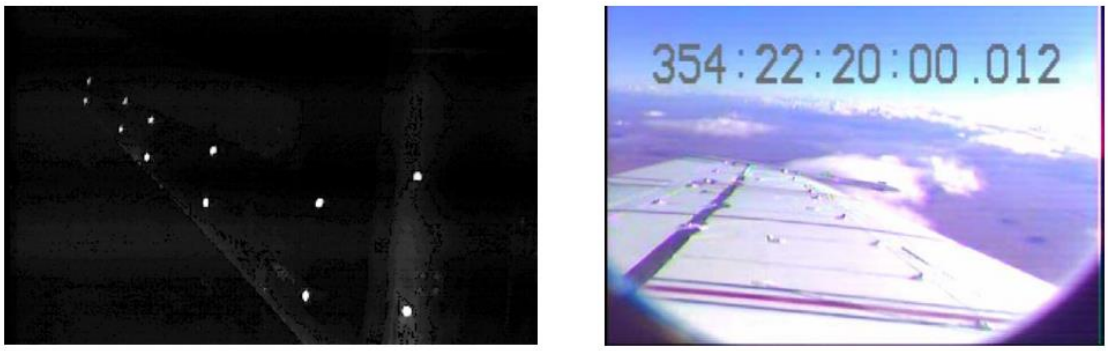

Figure 9: On the left is the relatively high contrast retro-reflective targets for VMD in a wind tunnel and on the right an image of the active aeroelastic wing F/A 18 VMD system [30].

Some other limitations exist with this method. For ground testing the use of retro-reflective tape targets, a fixed light source and an adequately large angle of incidence which allows for good contrast of targets can be easily employed. With outdoor flight test applications, lighting can vary throughout the test, and installation of the camera on the test vehicle often restricts the camera angle of incidence to a small angle all of

which reduces the contrast of target which creates potential for large variations in flight making consistent target capture challenging.

Projection moiré interferometry (PMI) is a video based deformation capture system which permits continuous model deformation measurements to be acquired over the entire field of view of the camera system. PMI relies on the projection of a grid of equi-distant parallel lines onto a surface to be scanned. As the model is loaded the distortion of the lines projection on the surface will change allowing the shape to be tracked relative to the aerodynamic loads. Typically, this system requires a projector for the parallel lines and a receiver. Subtraction of the reference pattern from the distorted patterns generates what is referred to as a fringe pattern, also known as Moiré's fringes, these patterns contain information to which displacements can be attributed.

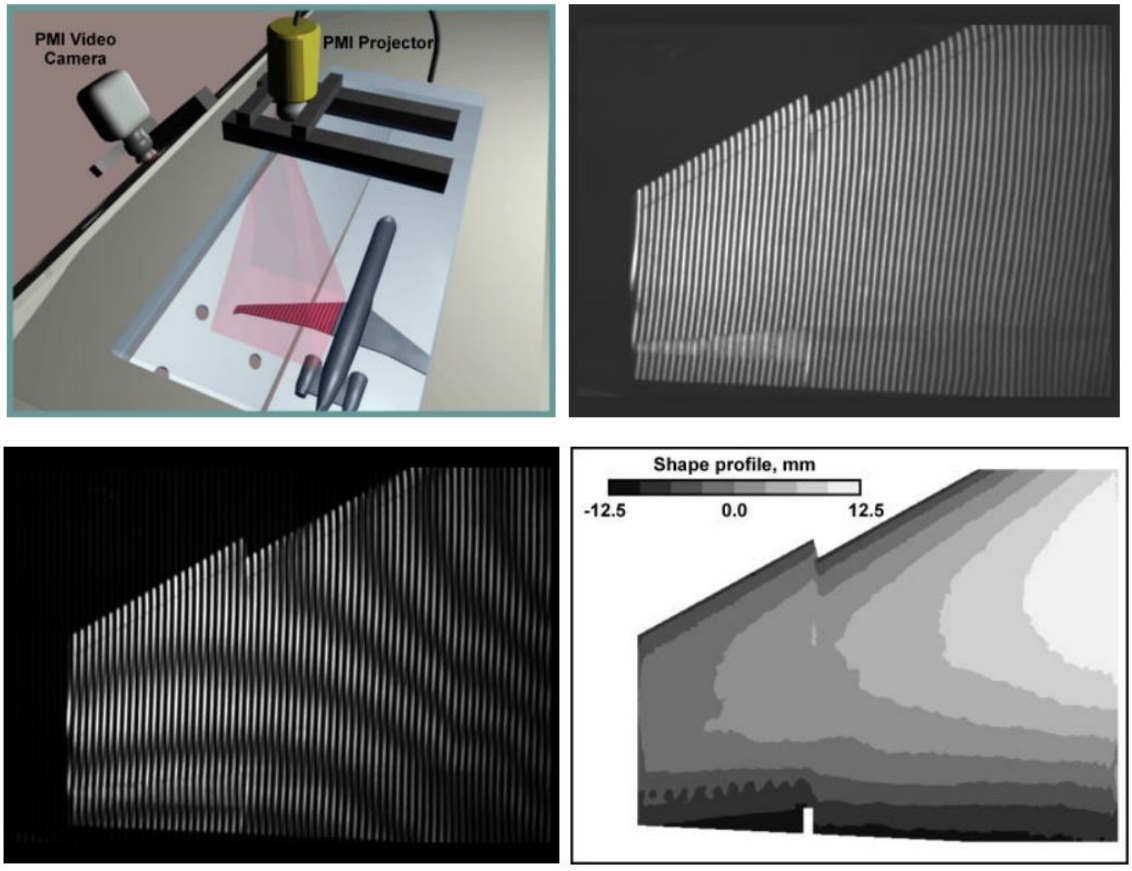

Figure 10: Top left PMI configuration, top right PMI image showing reference projected grid lines. Bottom left Moiré fringes after wing deformation, and bottom right, calibrated displacement topology. [31]

Restrictions in the positioning of the projector and video camera limits the use of PMI to the laboratory such as wind tunnels.

Systems such as the electro-optical flight deflection measurement system (FMDS) [32] or the commercially available Optotrak have been employed in the past for both ground and flight tests. These systems use photogrammetry of synchronized and discriminated infrared emitting diode (IRED) targets to determine three dimensional spatial coordinates. The Optotrak™ RH-2020, a commercial product developed by Northern Digital Inc. (NDI), was originally delivered to Boeing for aerospace research. It since has been sold for a variety of applications including industrial metrology. These systems are large, costly, and require holes and wiring to be routed through the wing for the IRED targets.

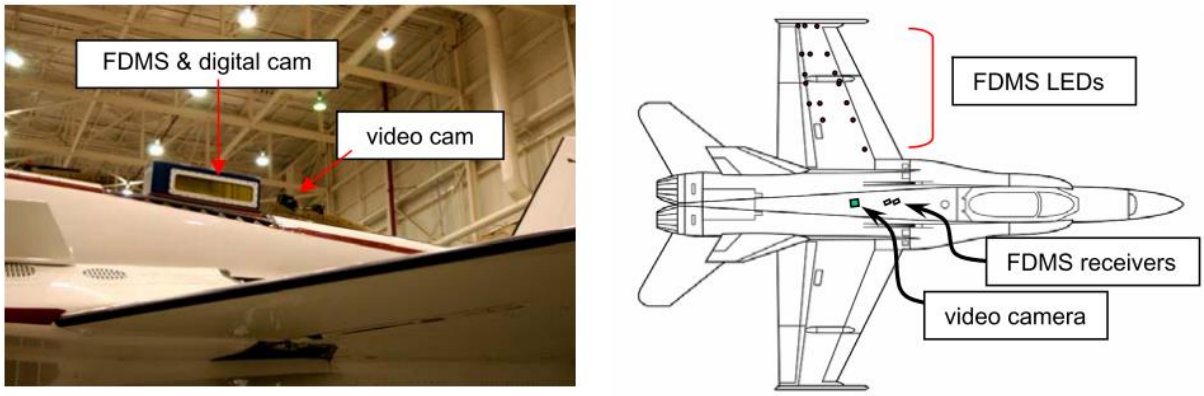

Figure 11:FDMS system and single camera VMD installed on NASA active aeroelastic wing F/A 18 [28].

2.1.2 Strain Deformation Methods

Classically, strain gauges have been used to infer load and shape. Presently there are two popular methods for estimating deformation of structures in aerospace today. One method uses a set of closed form equations built around classical beam theory to estimate slope, deflection, and cross-sectional twist angle for a beam. The equations are in terms of strain. This method, referred to as Ko's displacement theory [33] was originally developed for highly flexible aircraft wings such as the AeroVironment Helios. The method was first applied in a flight test on the NASA Ikhana[34], and subsequently on a number of other high aspect ratio wing and aeroelasticity projects [35]–[37]. Some reformulations of the original base equations have been suggested to improve the robustness of the method in real world experimental conditions [38].

Figure 12: NASA Ikhana aircraft procured to support Earth Science missions and advanced technology development. Note in Left) black tape along upper wing surface concealing Fiber Optic Sensing System fibres for strain measurement[34].

Alternatively, another method uses a set of strain and displacement modes to fit a measured strain pattern and estimate shape. Hassal and Gaukroger first developed and applied this method in the early 1970s at the Royal Aircraft Establishment [39] for use studying helicopter rotor blades. There initial application relied on creating mode shapes utilizing static measurements of approximate shapes. Later William Bousman investigated utilizing numerically estimated rotor flapwise modal shapes [40]. Other applications in aerospace have been considered for identification of structures shapes [41], [42]. Recently the method has also been investigated for civil structural health monitoring applications including bridges [43].

The method of strain pattern analysis (SPA) was adopted in this project [44] for several reasons including its ability to be used with a reduced set of measurement points, adequately small and affordable strain measurement equipment, reasonable processing overhead, and consistent measurement regardless of lighting. This method is further described in the following section 2.1.2.1.

2.1.2.1 Strain Pattern Analysis and Deformation Measurement

The assumption made by SPA for deformation measurement is that if a linear combination of truth strains can be made to fit a test article's deformed strain, then that same linear combination of truth deformations may be used to estimate the spatial deformation of the test article. By minimizing the sum of the least squares difference between the truth strains and measured strain a best fit is achieved which represents the deformation of the test article.

The proposed truth shapes used are the deformations and their matching strain patterns of the wings elastic modal shapes. With sufficient mode shapes, any linear deformation could be approximated. The maximum number of modes used to approximate the deformation is dependant on the number of measurements and their ability to remain linearly independent. A finite number of strain measurements is possible, and is particularly limited in this case with a small scale flying model where mass and volume are key constraints. In practice, with appropriate boundary conditions and shape selection a reasonably small number of mode shapes were required to estimate the structure deformation.

The method is described here. The principle of modal superposition is expressed as

$$D(p,t) = \sum_{i=1}^{m} \Phi_{D-i}(p) q_i(t) \tag{1}$$

where

$D(p,t)$ is the deflection of a point p at time t

$\Phi_{D-i}(p)$ is the deflection of mode i at point p

$q_i(t)$ is the unknown weighting function at time t

m is number of modes considered

Likewise the function may be written for strain as

$$S(p',t) = \sum_{i=1}^{m} \Phi_{S-i}(p') q_i(t) \tag{2}$$

where

$S(p',t)$ is the strain of a point p' at time t

$\Phi_{S-i}(p')$ is the strain of mode i at point p

$q_i(t)$ is the same unknown weighting function at time t

m is the same number of modes considered

Shifting to matrix form, equations (1) and (2),

$$\{D(p,t)\} = [\Phi_D(p)]\{q(t)\} \tag{3}$$

$$\{S(p,t)\} = [\Phi_S(p')]\{q(t)\} \tag{4}$$

Considering equation (4), if we make the equation equal to ϵ and then minimize this error we may solve the equation as,

$$\{q\} = \left[[\Phi_S]^T[\Phi_S]\right]^{-1}[\Phi_S]^T\{S\} \tag{5}$$

and from this we can determine the displacement as,

$$\{D\} = [\Phi_D]\{q\} \tag{6}$$

2.2 Strain Measurement Methods

As the name implies, strain gauges measure strain of an object to which it is attached. The most common type of strain gauge is the resistive foil strain gauge, whose invention is attributed to Edward E. Simmons, and Arthur C Ruge circa 1938 [45]. The foil gauge consists of a metallic foil pattern backed or encased in an insulating backing. The foil strain gauge functions by changing electrical resistance when deformed. Different methods exist for measuring the change in resistance, often this is done using a Wheatstone bridge. The change in resistance relative to the strain imposed is related using a quantity referred to as the gauge factor.

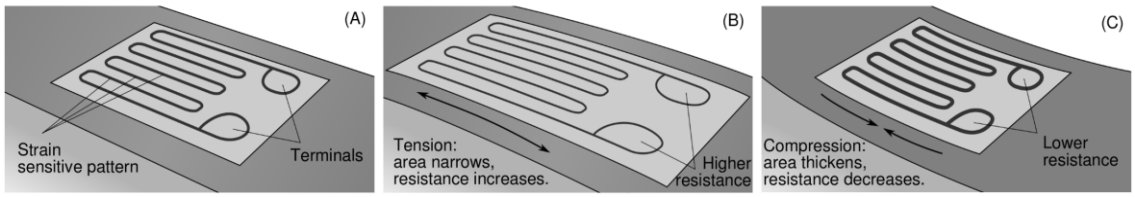

Figure 13: Conventional foil strain gauge with a zig-zag foil sensing pattern being deformed on a beam [46].

More recently new fibre optic sensing systems (FOSS), Fiber Bragg Gratings (FBGs) sensors, are becoming popular. First demonstration of an in-Fibre Bragg Grating was by Ken Hill in 1978 [47].

FBGs are a type of selective reflector, where specific wavelengths of light can be reflected while others are passed with minimal attenuation. This is achieved using periodic variations in the refractive index of an optical fiber's core. In telecommunications, this is commonly used as a band pass filter.

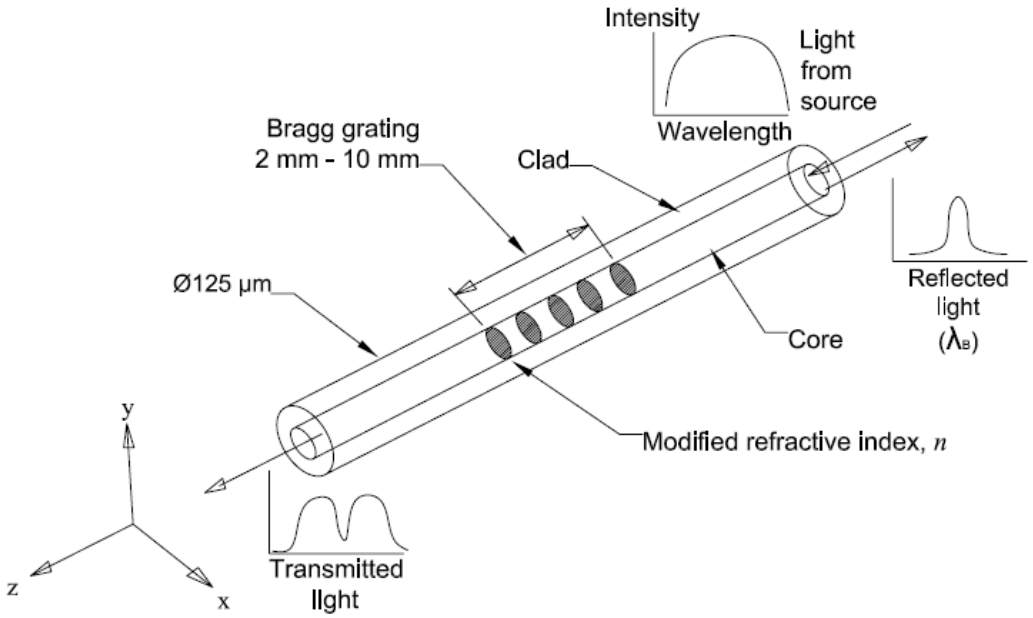

Figure 14: Optical fibre with FBG inscribed in middle. Note the wavelength λ reflected is functional to spacing between Bragg gratings.

FBG's offer a number of benefits including but not limited to,

- ability to daisy chain many sensors on one fibre (from 14 to thousands, depending on demodulation technology)
- Able to conduct measurement over great distances (>10km)
- Chemical and radiation resistive
- Electrically passive, and non-conductive

Cost of fibre optic sensing is still generally higher than that of equivalent foil strain gauge systems, however, cost is coming down. The cost of using this system mostly lies with the demodulation technology used to take measurements from the fibre.

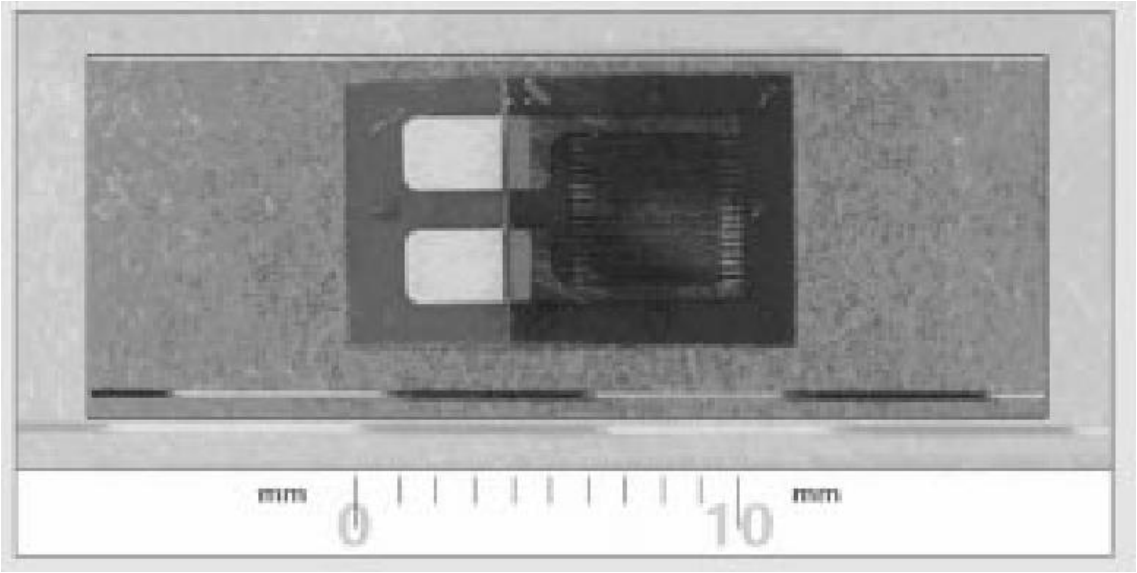

Figure 15: 5mm long FBG on 125µm optical fibre next to an equivalent 5mm long foil strain gauge.

Modern FBGs used for telecommunications systems and sensing applications are mostly made using a process where a UV laser interference pattern, which reacts with the glass changing the index of refraction, inscribes the Bragg grating onto a fiber such as standard telecommunication grade germanium doped single-mode fiber.

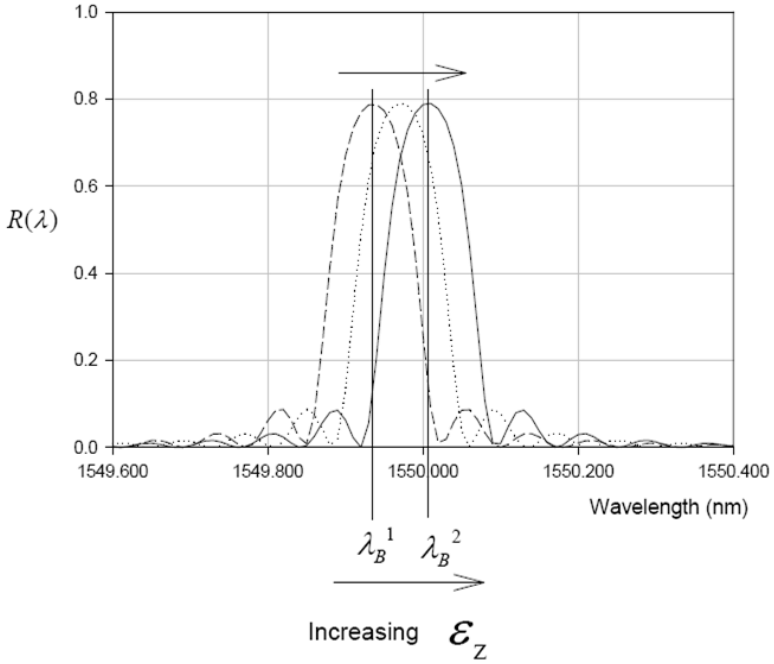

Figure 16: Reflected wavelength shift due to strain or temperature deformation of FBG sensor on an optical fibre.

The Bragg wavelength reflected by an FBG is sensitive to measure both strain and temperature changes. This is a result of the periodic Bragg grating being stretched or compressed. FBGs are used as both direct and indirect sensing. FBGs have been used in seismology, pressure sensors, oil, gas[48], and nuclear applications. FBGs also lend themselves to being embedded in composite structures, making for a robust and long lasting sensor network [36], [49]–[51]. Some difficulties can result from integration within composites such as small radius bridging resulting in significant signal attenuation, FBG birefringence, and even fibre failure [52], [53].

For measurements, different techniques exist for demodulation of the wavelength shifts in an FBG. Several common methods used today include, Edge filter demodulation, Wavelength Division Multiplexing (WDM), time domain multiplexing (TDM), and the relatively new optical frequency-domain reflectometry (OFDR). Currently most commercial systems are based on variations of the WDM demodulation where a laser sweeps spectrally over some wavelength span (often near the c-band between 1528nm and 1568nm).

Cost constraints, the large size and weight of optical interrogators (at time of project feasibility study in 2015) and the wing structure design in this project led to the adoption of conventional foil strain gauges.

2.3 Modal Analysis

Modal analysis is the study of structural dynamics with applications in noise and vibration. It is a large field of study encompassing many disciplines. Many comprehensive overviews of this topic have been published including a book by Brandt [54] emphasizing experimental measurement.

Modal shapes are a key element estimating the deflection shapes of the wing in-flight using the proposed strain pattern analysis method. This section will provide an overview of the fundamentals of modal analysis as it applies to linear cases pertinent in this work.

2.3.1 Analytical Model

For review, using Newton's second law, consider a mechanical vibrating system with multiple degrees of freedom (MDOF) modelled as a second order differential equation (ODE),

$$\boldsymbol{M}\ddot{x}(t) + \boldsymbol{C}\dot{x}(t) + \boldsymbol{K}x(t) = \boldsymbol{F}(t) \tag{7}$$

where **M**, **C** and **K** are each respectively the mass, damping, and stiffness matrices, $x(t)$, $\dot{x}(t)$, and $\ddot{x}(t)$ are the displacement, velocity, and acceleration vectors for each degree of freedom (DOF) in the system modeled. The equation is equal to F(t) which

describes an external excitation. From this point the nomenclature denoting time dependence will be dropped for brevity.

Equation (7) is re-written in state space form resulting in the equation.

$$\begin{bmatrix} C & M \\ M & 0 \end{bmatrix} \begin{Bmatrix} \dot{x} \\ \ddot{x} \end{Bmatrix} + \begin{bmatrix} K & 0 \\ 0 & -M \end{bmatrix} \begin{Bmatrix} x \\ \dot{x} \end{Bmatrix} = \begin{Bmatrix} F \\ 0 \end{Bmatrix} \tag{8}$$

Equation (8) may be further simplified as,

$$\boldsymbol{A\dot{u} + Bu = F'} \tag{9}$$

Where **A**, **B**, **F'**, $\boldsymbol{u}$, and $\dot{\boldsymbol{u}}$ are,

$$\boldsymbol{A} = \begin{bmatrix} C & M \\ M & 0 \end{bmatrix} \tag{10}$$

$$\boldsymbol{B} = \begin{bmatrix} K & 0 \\ 0 & -M \end{bmatrix} \tag{11}$$

$$\boldsymbol{F'} = \begin{Bmatrix} F \\ 0 \end{Bmatrix} \tag{12}$$

$$\begin{cases} \boldsymbol{u} = [x^T \quad \dot{x}^T]^T \\ \dot{\boldsymbol{u}} = [\dot{x}^T \quad \ddot{x}^T]^T \end{cases} \tag{13}$$

From equation (9) a first order ODE maybe be recognized. A generalized family of solutions exist of the form,

$$\boldsymbol{u} = \boldsymbol{\Phi} e^{\omega t} = \begin{Bmatrix} \phi \\ \lambda\phi \end{Bmatrix} e^{\omega t} \tag{14}$$

If equation (9) is set to equal 0, the free vibrations of the system may be solved. The Laplace transform of this is

$$|s\boldsymbol{A} + \boldsymbol{B}|\boldsymbol{U}(s) = 0 \tag{15}$$

If $\mathbf{A}^{-1}$ is multiplied through equation (15) and s=λ we may solve for the eigenvalues. This will lead to 2N eigenvalues and eigenvectors however, solutions may either be real or conjugate paired poles leading to N eigenvalue and eigenvectors. Real eigenvalues describe an over-damped pole. These poles describe modes of free vibration. A generalized solution for these modes may be written as,

$$s_m = \xi_m \omega_m + j\omega_m \sqrt{1 - \xi_m^2} \tag{16}$$

where m, some number from 1 to N, refers to the vibration mode, ω_m is the natural frequency, and ξ_m is the modal damping coefficient. These modes match with frequencies at which the structure will resonate.

The complex nature of the modes indicates that each DOF has a respective phase angle. Therefore, the motion of each DOF reaches its peak displacements at different instances in time. Here the term, mode complexity, defines the degree by which a mode diverges from the ideal undamped mode. A mode shape which does not resemble a standing wave, but instead appears to be traveling, moves a structure may be quantified by the modal phase collinearity criterion (MPC), where unity is the greatest value indicating a normal mode.

2.3.1.1 Undamped Case

Often the modal response of a structure begins with an undamped analysis. This is because of the inherent difficulties in modelling damping. These modes are often also referred to as normal modes. With normal modes there is a corresponding respective set of mode shapes. The mode shapes are unique for each given structure and boundary condition.

Setting the damping matrix **C** to zero in equation (7) for a freely vibrating system results in,

$$\boldsymbol{M}\ddot{x}(t) + \boldsymbol{K}x(t) = 0 \qquad (17)$$

This simplified equation's roots are a bit more straightforward to calculate for the Laplace transform. The poles for the undamped system are given by $s_m = j\omega_m$.

2.3.2 Numerical Solution

A brief overview of general numerical methods is relevant in its application in this work. Modal behaviour of the structure is predicted numerically and the resulting shapes are used to estimate the deformation of the wing in flight. There are variety of methods used to extract eigenvalues and their accompanying eigenvectors, several of which are based on the power method. Generally, this is a two-step process starting with simplification of the original stiffness matrix (for example, tridiagonalization) while retaining original eigenvectors. This then allows for an iterative solution technique for determination of a selective number of solutions starting with either the lowest or highest eigenvalue [55].

Modern commercial FEA packages, such as Ansys and FEMTools, generally offer a number of solution methods including but not limited to Givens, Modified Givens, Householder, Modified Householder, Inverse Power, Sturm, and Lanczos.

The Lanczos method was originally presented by Cornelius Lanczos in 1950 [56], however the original formulation had limited use due to numerical instability. Later, Ojalvo and Newman [57] made some adaptations to Lanczos' original method to enable

stability. Apart from some small changes, this method is widely used today. Unlike some methods, like the inverse Power Method, Lanczos allows the determination of a specific number and range of eigenvalues and eigenvectors. For models with a stiffness matrix composed a large number of degrees of freedom (such as used in this study), this reduces solution time considerably.

2.3.3 Ground Vibration Testing

Ground vibration testing (GVT) is the experimental measurement of an aircraft structures vibration modes including peak frequencies, damping, and mode shapes. This is also more generally referred to as experimental modal analysis (EMA). These measurements may be used in part to assure no adverse dynamic behaviours occur such as aeroelastic and aero-servo-elastic instability of a new or modified aircraft. GVT or EMA for an aircraft can provide support for flutter identification, detection of structural flaws, and identification of flight control dynamic problems.

2.3.3.1 Frequency Response Function

To identify the dynamics of a system the concept of a black box is considered. Here for a known input some output response will occur. For some output $y(t)$ over some input $x(t)$ we take the Laplace transform and their ratio as $H(s) = \frac{Y(s)}{X(s)}$, the transfer function (TF). The poles of this system define the modal frequencies, or frequencies at which the system vibrates freely. In experimental work the TF is more readily measured in the form $H(f) = \frac{Y(f)}{X(f)}$, the frequency response function (FRF). The FRF is obtained by evaluating the imaginary axis of the Laplace domain where $s = j\omega$.

The FRF function, $H(f)$, for a MDOF system contains all the receptance frequency responses for the system, that is to say for all the individual inputs q, and output responses p. Elements in this matrix can be written as every mode's residues divided by the complex conjugate poles of the system for that mode. This fractional expansion is known as the modal superposition equation [54], seen in equation (18) in TF form, and in equation (19) as the FRF.

$$H_{pq}(s) = \sum_{m=1}^{N} \frac{A_{pq,r}}{s - s_m} + \frac{A^*_{pq,m}}{s - s^*_m} \tag{18}$$

$$H_{pq}(j\omega) = \sum_{m=1}^{N} \frac{A_{pq,m}}{\xi_m \omega_m + j(\omega - \omega_m\sqrt{1 - \xi_m^2})} + \frac{A^*_{pq,m}}{\xi_m \omega_m + j(\omega - \omega_m\sqrt{1 - \xi_m^2})} \tag{19}$$

$A_{pq,r}$, and $A^*_{pq,m}$ are the residues, while ω_m and ξ_m are the same frequency and damping parameters previously defined for every mode m.

The FRF, unlike the TF, can be experimentally measured. Measurements are sampled in the time domain, such as but not limited to force or acceleration. These sampled measurands may then be transformed into the frequency domain using the Fourier Transform. Generally this is accomplished with a discrete variation of the Fourier transform known as the Fast Fourier Transform (FFT) method, first published by Cooley and Tukey [58] in 1965, although it has since been discovered that other mathematicians such as Gauss had discovered this roughly 150 years earlier [54].

The signals of interest originate as analog sources and require sampling, quantization before they can be passed through an FFT successfully. Consider that sampling refers to the timing at which signals are recorded. If a signal is not sampled at an adequately high frequency, the frequency phenomena of interested cannot be resolved possibly even resulting in aliasing. Quantization in this case refers to the accuracy of the sampled signals amplitude.

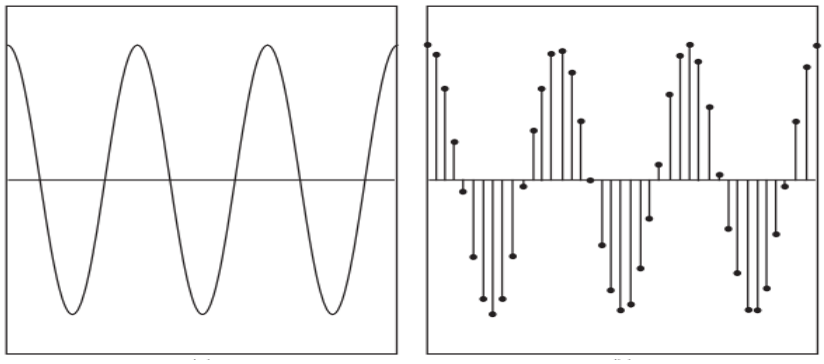

Figure 17 Analogue to digital conversion (ADC) of analogue signal, on left, to discrete digital signal, on right, [59].

The minimum sample rate to resolve a frequency of interest may be set using the Nyquist-Shannon sampling theorem, sample period must be at least half that of the signal of interest. To prevent aliasing of higher frequency signals a low pass filter should be applied to prevent signals with frequencies higher than half the sample rate from being misconstrued as lower frequencies.

After filtering, sampling/quantization of the analogue signal, the digital signal when passed through an FFT may still encounter significant errors. For an FFT to properly reproduce actual frequency spectra the time domain signal needs to be periodic over the sampled interval. If the signal is aperiodic incorrect estimates of frequency and amplitude result. This type of distortion is referred to as leakage. Several approaches exist to manage leakage including, averaging, increased frequency resolution, use of periodic/special excitation, and the of use of time domain windowing functions [59].

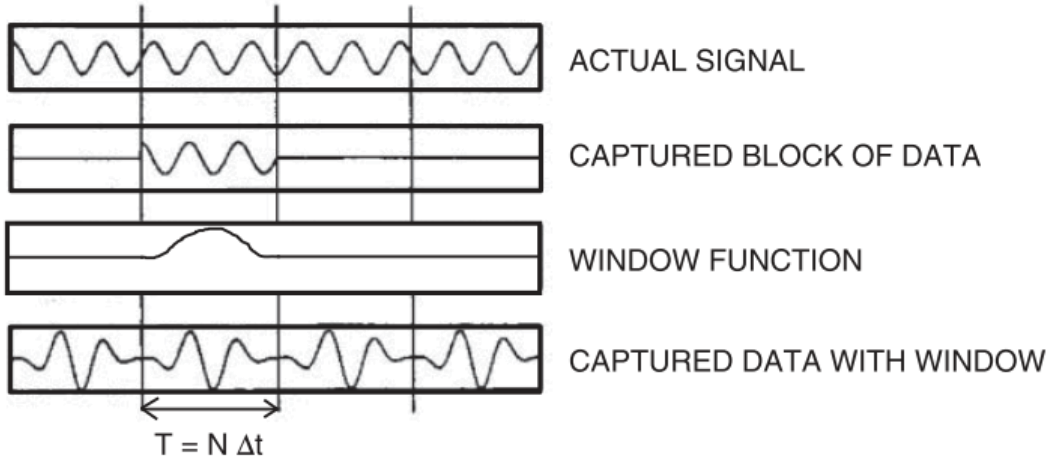

Figure 18: Application of a window function to a sampled analogue signal to reduce leakage prior to FFT [59].

The window function's goal is such that when applied to the sampled signal it better satisfies the periodic requirement of the FFT. Different window shapes have advantages or drawbacks depending on the type of signal being investigated. Several common windows used in EMA are the Hanning, rectangular, and exponential, windows.

Useful for the identification of issues in measurements taken for use in estimation of an FRF is the coherence between the input x(t) and output y(t) signals. The coherence for a linear system estimates the extent to which y(t) may be predicted from x(t). This assumes. The coherence is a real valued function defined as,

$$\mathrm{C}_{xy}(f) = \frac{\left|G_{xy}(f)\right|^2}{G_{xx}(f)G_{yy}(f)} \tag{20}$$

where $G_{xy}(f)$ is the cross-spectral density between x and y, and $G_{xx}(f)$ and $G_{yy}(f)$ are the spectral density of x and y respectively. Values of coherence will always satisfy $\mathrm{C}_{xy}(f) \leq 1$, the Cauchy-Schwarz inequality, provided an ideal linear system. An ideal, linear system with single input and single output would have a response of 1.

2.3.3.2 Modal Excitation

To study a structures response a quantifiable input is required. This input initiates the excitation for a response measurement. Two commonly used approaches for EMA are the use of impact testing and shaker testing. In each of these cases a force is dynamically applied to the structure. For these types of experiments, acceleration is normally measured using an accelerometer.

Impact testing is generally the most common excitation technique. The use of an impact hammer with force sensing transducer or impedance head is the basis of this

method. The impact hammer will generally have a set of replaceable tips with varying geometry and hardness to accommodate different structures excitation requirements.

A simple experiment may involve a single impact hammer and one accelerometer. The sampling of both the impedance transducer and accelerometer during an impact excitation would be adequate to measure a single degree of freedom.

The goal of the excitation technique is to excite all the modes of interest in the structure. The narrow pulse imparted by an impact allows for a broad frequency spectrum to be delivered to the structure. The more finite the impact the broader the energy content, as it approaches the ideal Dirac delta. This can be controlled by the hardness of the impact tip. The harder the tip the higher frequency content generally.

To maintain the validity of the modal experiment, measurements must generally be kept as linear as possible. Impacting to much energy in one point of the structure can result in non-linear dynamics to occur. There are several ways to avoid this, including lighter impacts, softer impact tips. Note that with these choices come trade-offs such as frequency range and signal to noise.

Shakers are preferable in some applications, offering more control in the input excitation than impact hammers. Some examples include heavily damped structures Shakers are generally either electromagnetic or electrohydraulic driven. The extra control afforded by shakers generally comes at the cost of more intricate experimental set-up and planning.

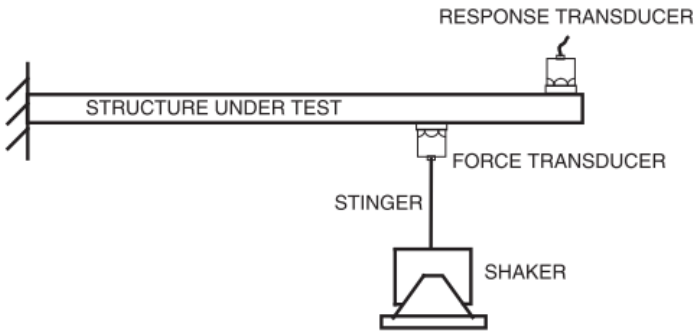

Figure 19: Shaker attachment to structure for testing [59].

A shaker setup is comprised generally with the shaker, stinger, force transduce, response transducer (accelerometer) and the test structure, as seen in Figure 19. The alignment of the shaker is important such that only axial forces are driven through the stinger. A means of testing for this is through reciprocity. This can be achieved either with a single shaker and impact hammer or a multi-shaker setup. Two points are selected on the structure, one the desired input location for the shaker, another some reference degree of freedom for measuring acceleration or input (impact or shake). If

properly setup, and non-linearities are not introduced, an FRF derived from DOF A to B or B to A will be the same.

Shakers allow flexibility in application of different signals into a structure. A wide variety of signals can be used including deterministic and non-deterministic signals. Deterministic signals include, stepped sine, and sine chirp signals, whereas non-deterministic signals include random and burst random noise.

A combination of impact and shaker testing was used for experimental modal analysis of the flexible wing structure presented. Impact testing was adequate for most frequencies above 6Hz, however it was challenging to achieve good measurement coherence for the low and highly damped first bending mode at roughly 3Hz. This first mode was of particular interest for this study and as such was verified using a shaker for which greater coherence was verified using sine chirps focused between 1-20Hz.

2.3.3.3 Test Strategy and Pre-Testing

The test strategy is driven by several different factors. These include the structure, modal properties of interest, available equipment, time and budget. A number of factors should be considered. There is no one way to conduct a test, and final strategy is often determined by the test engineer and their experience.

First the number of degrees of freedom needs to be chosen. The greater the number of measured degrees of freedom the better spatial resolution of the mode shapes. At minimum, for m mode shapes to be resolved, m DOFs need to be measured. If there is an insufficient number of DOFs measured, spatial aliasing can occur, however, peak frequencies could still be acquired. If there is priori knowledge of expected mode shapes, this enables positioning of sensors where they will be most effective. Consider that a transducer installed in a mode's node will be blind to vibrations of this mode.

Next sensor installation method should be considered. Will all DOFs be instrumented simultaneously or will a method of roving be applied. There can exist reasons for either option. Some general considerations are, is there sufficient budget to acquire enough transducers to equip all the DOFs simultaneously. Will mass loading, a condition where the dynamics of the structure change as a result of additional mass from mounting transducers to it, be significant? A common configuration is for a single output reference accelerometer, and a roving impact hammer input at multiple DOFs.

Another consideration is the number of references FRF determination. For simple structures generally one reference is sufficient. For more complex cases where modes are heavily coupled or have very close peak frequencies multiple spatially separated reference DOFs can be used to separate these mode shapes from each other [54]. Although not necessary for the simple cantilever wing in this project, the joined wing sensorcraft required multi-reference EMA to decouple the wings elastic modes [60].

2.3.3.4 Modal Parameter Extraction and Analysis

After collection of experimental data and creation of FRFs the next step would be the identification and extraction of modal parameters. This process is described in the context of workflow using the commercial EMA software tool MEscope by Vibrant Technology. This process may be divided into three stages,

1. Identification of the normal modes;
2. Curve-fit of FRFs to determine modal frequencies and damping;
3. Refined curve-fit and modal shapes.

The identification of normal modes can be achieved in several ways. Here two methods used in this project are discussed. For simpler structures without highly coupled modes these methods are effective

First a quick method to visualizing structural mode shapes is taking the operational displacement shapes (ODS) and selecting frequency which coincides with a captured FRF peak suggesting a normal mode frequency. This provides a sense of which FRF peaks are in fact a mode as well as providing feedback on whether a mode is normal or complex. Often the mode indicator function (MIF) is used to help identify modes. A variation is the complex MIF (CMIF). The CMIF is a sum of the magnitude of all FRFs imaginary part squared. This method operates on FRFs with one common reference. Multiple reference data requires a more sophisticated MIF, such as the multi-variate MIF (MMIF), however, for this work, modes where sufficiently decoupled that a single reference was found to be suitable. For more information regarding MIF Brandt offers a good summary [54]. Note this process was conducted in this project using a commercial software tool, MEscope by Vibrant Technology Inc with internally implemented CMIF and MMIF functions.

After identification of modes using the MIF function, in step two, a preliminary polynomial curve is fit over experimental FRF curves. From these polynomials and the identified modal peaks, damping and resonant frequencies are estimated. Two methods for accomplishing curve fits are the local polynomial and the global polynomial. Local polynomial fits are applied for each individual FRF, whereas the global methods are fitted simultaneously and is better suited to multi reference FRFs. From the curve fit, resonant frequency peaks, and damping are measured. The undamped natural frequency is calculated from the resonant frequencies and the damping.

In the third step another curve fit is performed to extract mode shapes. A curve fit of a rational fraction polynomial (RFP) of the form seen in equation (18) is performed using least squares. To better define the solution and minimize error, a global curve fitting method [61] is practised where the modal resonant frequencies and damping coefficients estimated in step 2 are used to better define the RFP fit. The residuals may then be exploited to define mode shapes.

Chapter 3- Design, Modelling, and Simulation

3.1 Application Workflow

The steps in Figure 20 are followed to apply the SPA method for deformation monitoring of the flexible ASE wing.

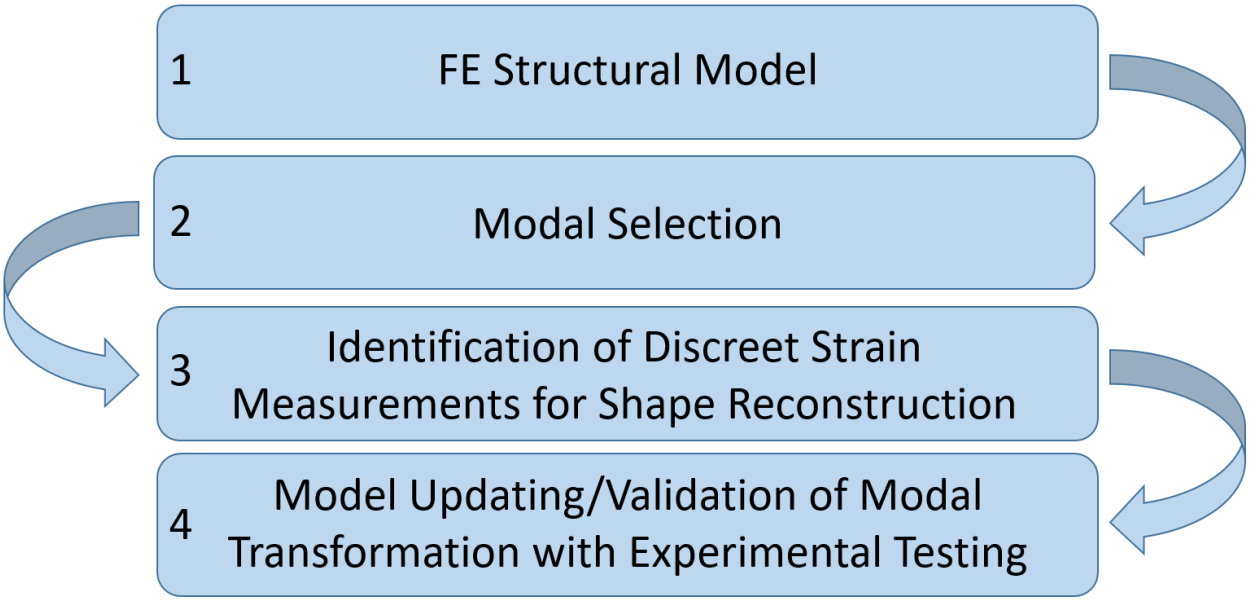

Figure 20: SPA application workflow flowchart

1) Finite Element model - An FE model of the wing is made representing the experimental structure. The strain patterns, including candidate gauge locations, is chosen based on outputs from this model. A static linear analysis was conducted with representative aerodynamics loads expected in flight and point loads for ground testing/model updating later. {S} and {D} are recorded for testing and verification of the chosen strain patterns.

2) Modal Selection - Using the FE model, modal responses are calculated. This analysis is done such that the boundary conditions of the model match conditions expected in operation. In this case an aero load was estimated with the aircraft cruising in a trimmed state. This reduces the number of modes required to minimize the fitting error ϵ. The resulting displacement shapes (Φ_D) and strain shapes (Φ_S) are saved.

3) Identification of Discreet Strain Measurements for Shape Reconstruction - To minimize error ϵ deformation shape reconstruction from SPA, steps 1-2 are iterated with

discreet gauge locations, bridge types to identify an appropriate configuration. Design and results are verified using simulated numerical results from the FE model.

4) Model Updating/Validation of Modal Transformation with Experimental Testing - Here the flexible ASE aircraft wing test article is experimentally tested for validation. Static load and GVT provide data for validation of the FE model used in steps 1-2. Discrepancy between the model and the test article are corrected through a model updating process using deformation measurements. The SPA transformation is validated using experimentally measured reference strains and static displacements.

3.2 Aeroelastic Aircraft Platform

This work was completed as part of an effort to develop a 20kg remotely piloted flight test vehicle to generate a database of aero-servo-elastic responses to validate analytical aeroelastic models. An existing UAV, the QT1.2, with conventional 3.4m wingspan rigid wings was used as the basis for the work. The rigid wings were replaced with a set of custom designed, flexible wings, and the aircraft was designated QT1.3 as seen in Figure 21.

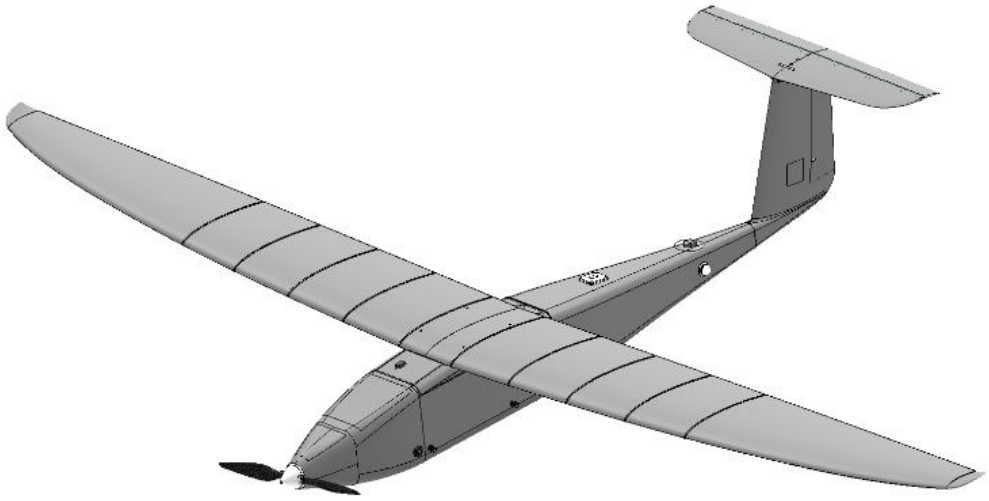

Figure 21: Flexible Aeroelastic Aircraft Platform QT1.3.

3.2.1 Aeroelastic Design

The flexible wings were designed to exhibit a predetermined high degree of coupling. A blend of two approaches was used to achieve this coupling: (i) the first approach was to try to bring the structural response frequencies to the same range as the aerodynamic responses. By doing so, a perturbation that could excite a given aerodynamic mode would also cause a structural response to occur. This can be achieved by means of a

perturbation in a control surface; and (ii) the second approach was to identify a body freedom flutter mode that would occur as a combination of a rigid body mode and an elastic mode. This would not require an external perturbation to produce an aerodynamic and structural response. The only requirement was to fly at a given speed that would cause that flutter mode to appear. By doing so, an interaction between a structural elastic mode and a rigid body mode could then be observed and captured. It was determined that the first elastic bending mode and the short period aerodynamic mode of the aircraft could be brought sufficiently close to allow the body freedom flutter as well as perturbation from control surfaces.

The goal of deformation of the wing measurements in this project was for aeroelastic tools evaluation with an emphasis around static deflection and the ability to look at dynamics of the wings regarding the aeroelastic modes of interest summarized in Table 2. Some example projected flexible wing shapes are shown in Figure 22 and Figure 23.

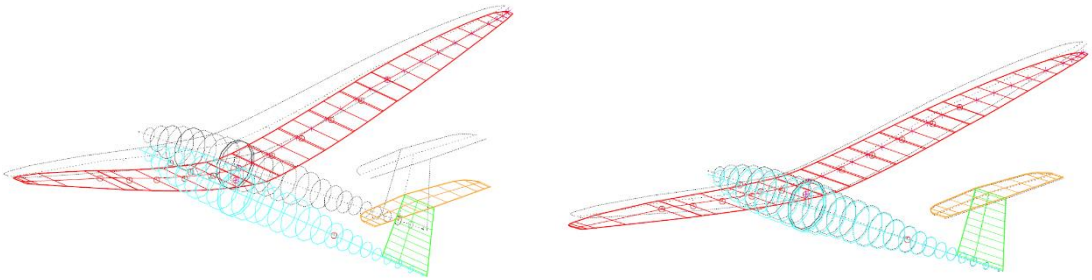

0 degree phase *90 degree phase*

Figure 22: Short Period mode shape plotted for two different phases an airspeed of 20m/s for the flexible QT1.3 aircraft.

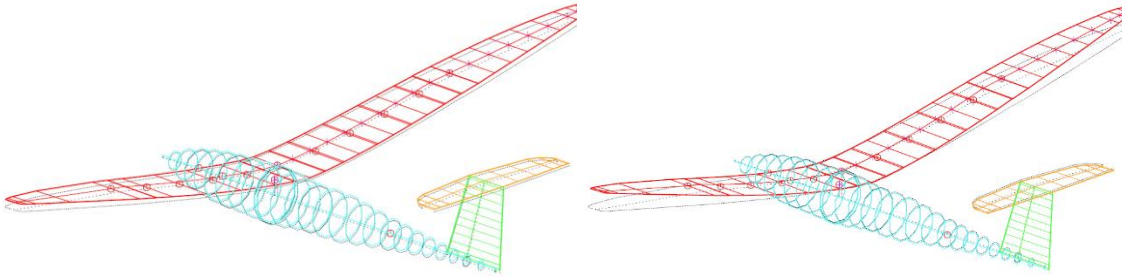

0 degree phase *90 degree phase*

Figure 23: The wing first bending mode shape plotted for two different phases at an airspeed of 20 m/s.

Table 2: Summary of aeroelastic modes of interest from final ASWing [62] model for the QT1.3 aircraft design. Note proximity between short-period mode and 1st Symmetric Bending mode at airspeed of 30 m/s.

Aeroelastic Modes Comparison				
Mode	Speed = 20 m/s		Speed = 30 m/s	
	Frequency [Hz]	Damping	Frequency [Hz]	Damping
Phugoid	0.0966	0.0635	0.0618	0.152029
Dutch-Roll	0.5141	0.126586	0.6975	0.117782
Short-Period	1.00200	0.461373	1.5684	0.479369
Wing 1st Symmetric Bending	2.71080	0.381353	1.6131	0.785061
Wing 1st Anti-symmetric Bending	10.27110	0.045863	10.2897	0.071245

3.2.2 Mechanical Design

The wing was redesigned, such that the inner 2/3 of the wing are flexible to alleviate difficulties in modelling and designing the effects of elasticity around the ailerons, seen in Figure 24.

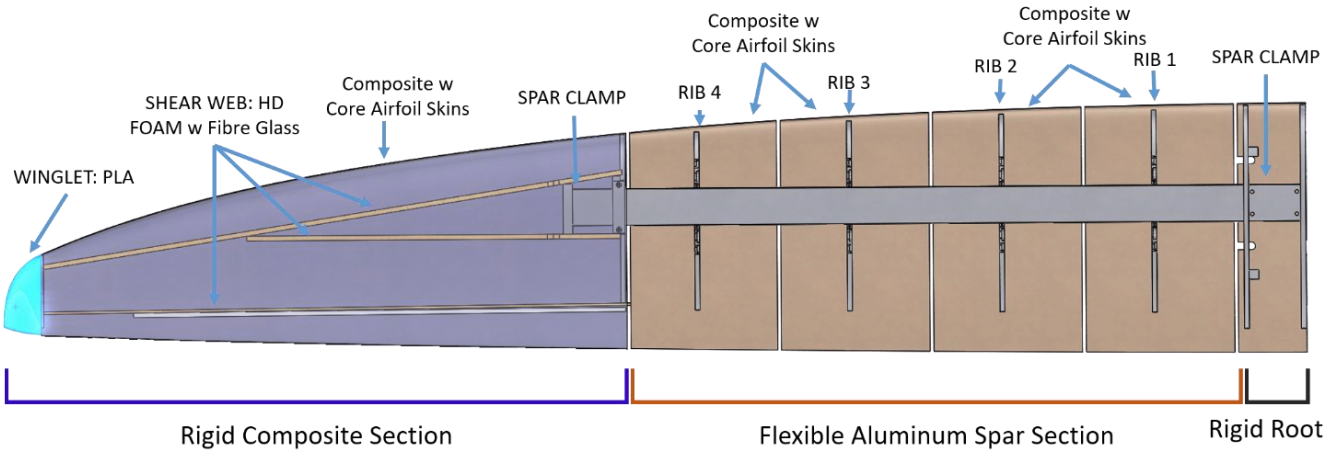

Figure 24: Layout of flexible wing.

The flexible portion of the wing has a spar made of a hollow aluminum extrusion custom sized to ensure that the first out-of-plane elastic bending mode shape coalesces with the QT1.3's aerodynamic short period mode (while cruising between 20m/s and 30m/s). The wing spar was designed so that its in-plane and torsional stiffness would prevent any interaction of their respective elastic modes in flight. The aerodynamic skins of the wing along the inner two-thirds of the wing are split into 4 sections, each attached

using a single aluminum rib clamped to the spar. This construction was used to limit stiffening of the spar via the skins, thereby simplifying the structural stiffness modelling.

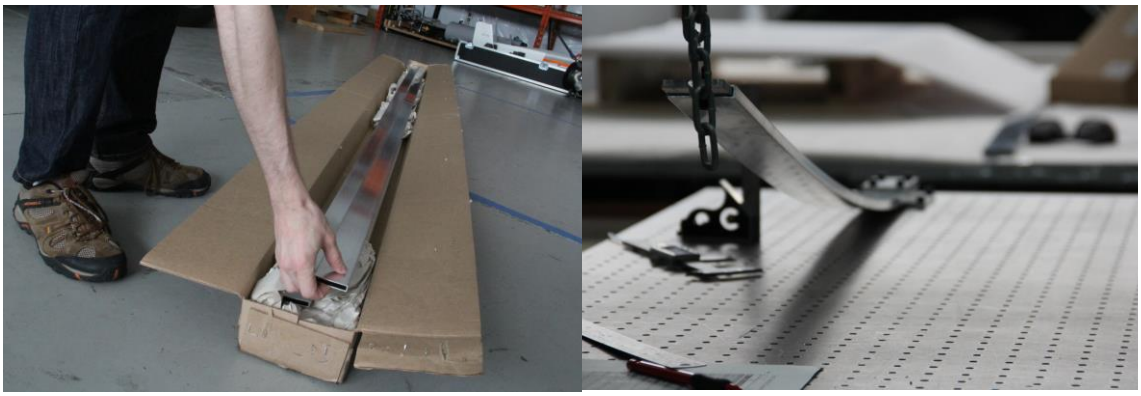

Figure 25: Custom hollow aluminum rectangular spar for use as main wing spar. Extrusion from 6065 Aluminum, annealed and heat treated t5.

The outboard 1/3 of the wing or the rigid part of the wing was made of a composite ply of 95gsm e-glass, 200gsm plain carbon, 3mm foam core, and 95gsm e-glass. This structure was intended to be very stiff and light. The upper and lower halves of the wings had several 3mm thick shear webs bonded between them to help stiffen them and prevent the halves from shearing apart or buckling. The composite wing layup is in Appendix A for further reference.

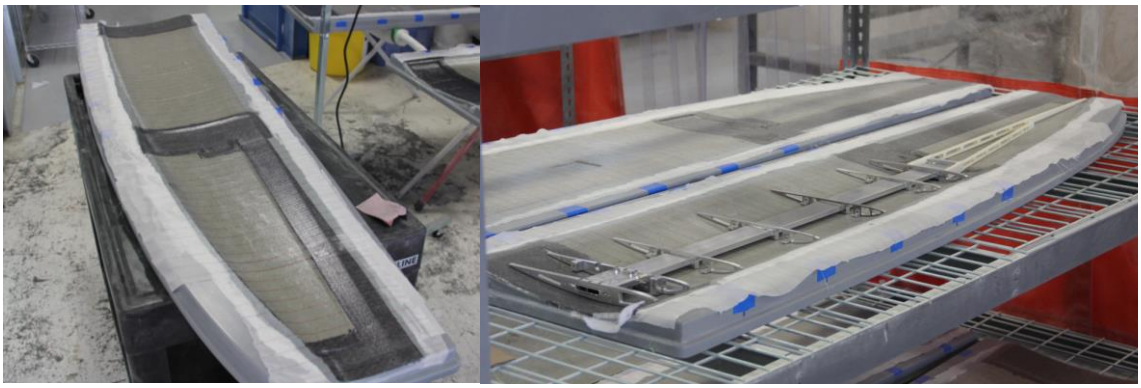

Figure 26: Left) Upper right semi-span wing composite skins. Note carbon stiffening of outboard wing section. Right) Dry fit of internal components including ribs, spar, clamping structure, and shear web for a semi-span of wing prior to bonding.

3.3 FE Model Design for SPA

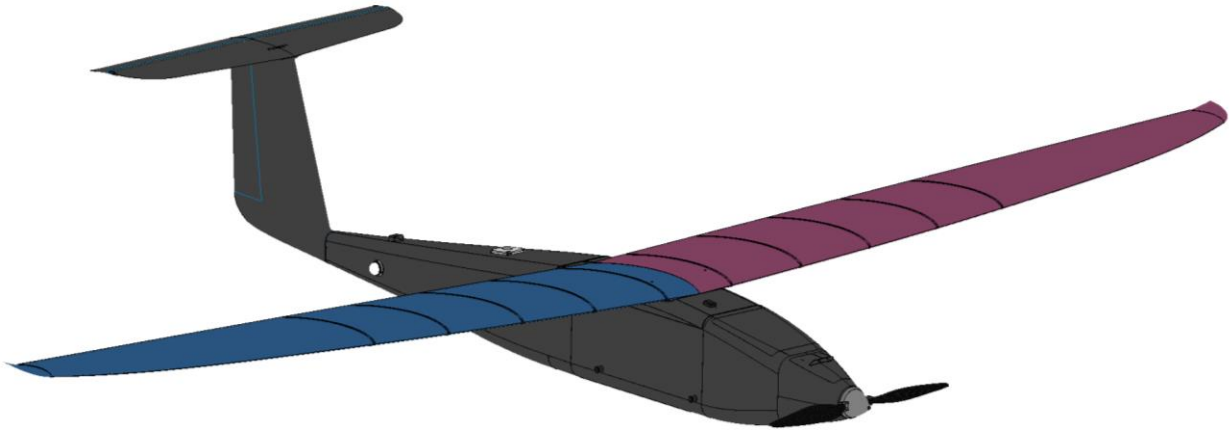

Figure 27: The Ansys FE structural model used for the SPA analysis focused on symmetric half of the wing. Symmetric modes were not required outputs for the SPA analysis requirements.

In this section the design of the FE model used to generate the numerical modal strain and deformation shapes is discussed. The ASE project in general resulted in the development of a number of different numerical models. Initial feasibility for coupling of elastic and aerodynamic modes was performed in ZAERO. This model was shortly thereafter replaced with an ASWing [62], [63] model which was used to size the flexible portion of the wing and to dimension the custom extruded aluminum spar. An equivalent NASTRAN beam model was also developed and benchmarked through the design and verification process to ensure that an equivalent elastic result was achieved in the more experimental ASWing tool.

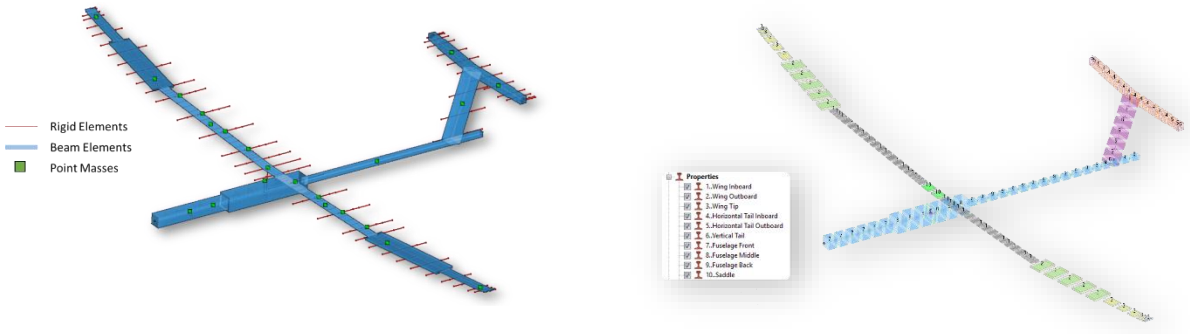

Figure 28: Left) Nastran structural model with rigid body elements. Right) Nastran model showing distinct beam locations

The 1d elements used to model the wing spars in the NASTRAN model were originally selected in an effort to minimize the complexity of the model to enable easier optimization and programme the generation of appropriate ASWing structural model. These elements however did not provide adequate strain field resolution for use in the SPA method.

Availability of a software license and familiarity with the alternative ANSYS tool led to the adoption of ANSYS for the implementation of the model used with SPA deformation measurement method. The ANSYS workspace project is pictured in Appendix B for reference.

3.3.1 Model Geometry

The FEM model was derived from the CAD used for design and manufacturing of the ASE flexible aircraft. The CAD was managed within Solidworks for this project, seen in Figure 29. The model is composed of individual parts mated inside assemblies. Components of this model were designed with an origin located at the leading of the wing root. This origin is common to the NASTRAN, and ASWING models, and is maintained in the ANSYS model for use in the SPA deformation measurements. The CAD model contains a variety of information relevant for manufacture including components to represent fasteners, wiring, and adhesives. Additionally, a number of features are present in structural parts for the purpose of manufacturing, including tolerances for fitment, alignment, and bonding. A configuration of this assembly required appropriate defeaturing prior to use in the FEM model.

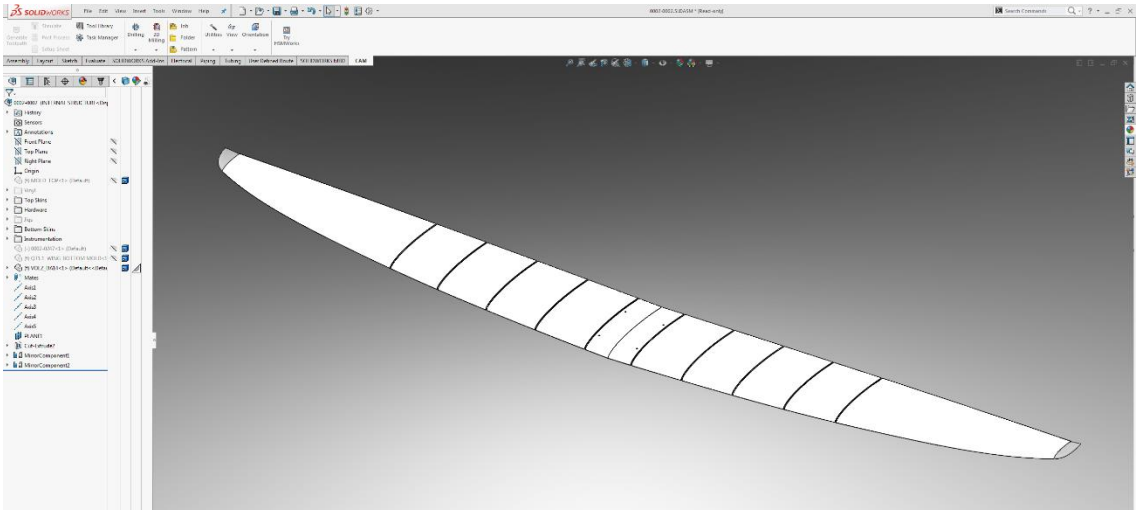

Figure 29: The Solidworks sub assembly of ASE flexible wing.

One of the boundary conditions considered is symmetry between the two semi-spans of the wing. With this in mind the right half of the model is removed. In the remaining half all fasteners and control horns, and other assorted hardware are removed.

The wing assembly was saved as a single Solidworks multi-body part. A variety of components including the composite rigid section, and the hollow aluminum spar were to be modelled using shell elements. This require surfaces as opposed to solid body models. Surfaces are copied and bodies are opened. Some bodies were not complete or fully knit together.

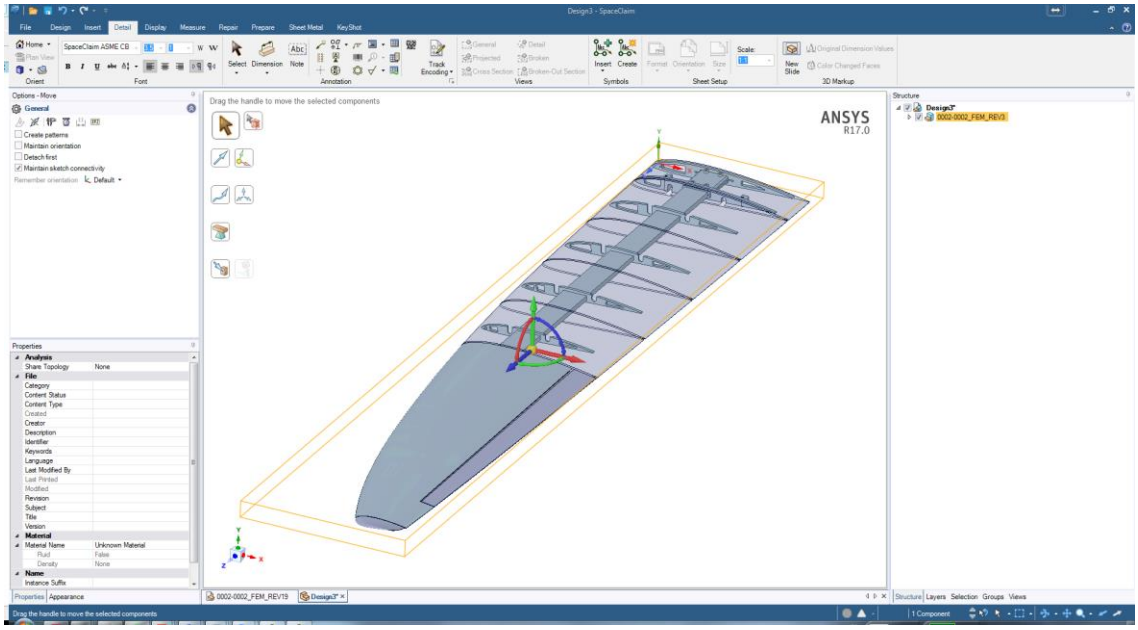

Figure 30: Initial geometry import into ANSYS Spaceclaim geometry editor.

The cutout in the ribs around the spar, fixturing holes for production and the overhead tab were patched using the fill extend, fill, and sketch patch tools. The shear webs inside the outer composite rigid wing were extended to meet the upper surface using the extend tool in the Spaceclaim.

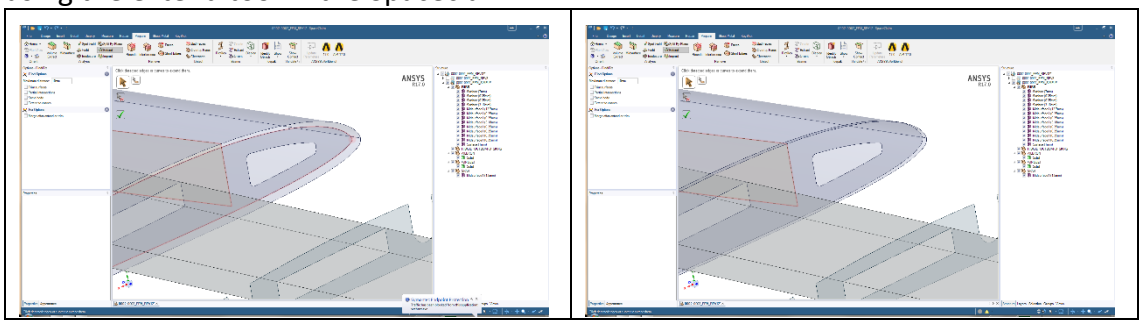

Figure 31: Left) Rib before extension with space for OML skin thickness and bond gap. Right) Rib after using extend tool to airfoil skins allowing mesh to be tied together. Note that red outlined shear web surface needs to be extended to skins and rib to be meshed together simulating being bonded.

The next step was to use the imprint tool in space claim to break intersecting surfaces intended to be meshed together latter. Following imprint of the the model, the individual surfaces where grouped into Spaceclaim assemblies. The spar, ribs, shear web, and airfoil skins were placed in an assembly group and a topology of "share" was set. The share topology indicates that grouped surfaces which intersect will be meshed together while maintaining their own discreet material properties. The winglet and aileron were kept in their own assemblies so they will not be meshed together. Single 1D element connections were defined for these components in the meshing editor.

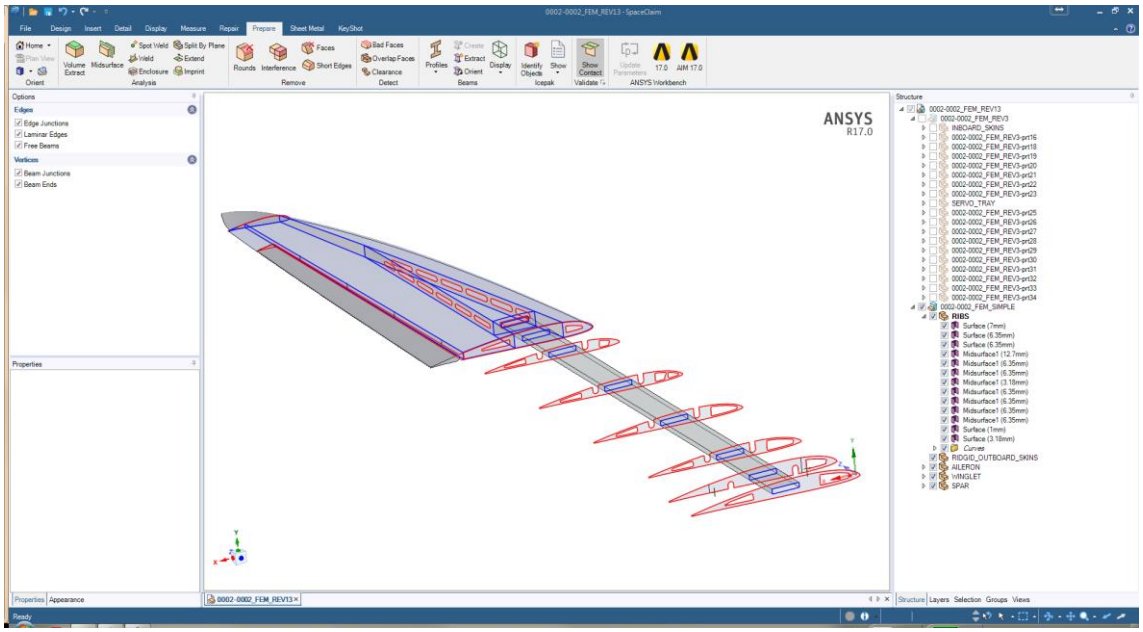

Figure 32: FEM with final topology contact set between bodies verified using show contact tool, ready for meshing. Blue lines indicated shared contacts between surfaces which will be meshed together.

3.3.2 MESHING

Meshing of the model was accomplished using the ANSYS MECHANICAL application. This step was coupled with beginning an ANSYS advanced composite model (ACP) group in the ANSYS workbench application. The composite material properties are defined later in Section 3.3.3.

Inside the meshing application all the appropriate surface and body connections were verified. The aileron and winglet were connected using single element and rigid body connections respectively, defined model surfaces prior to meshing. The ailerons were attached with 4 single elements representing the hinge points and given the ANSYS generic library value for aluminum stiffness.

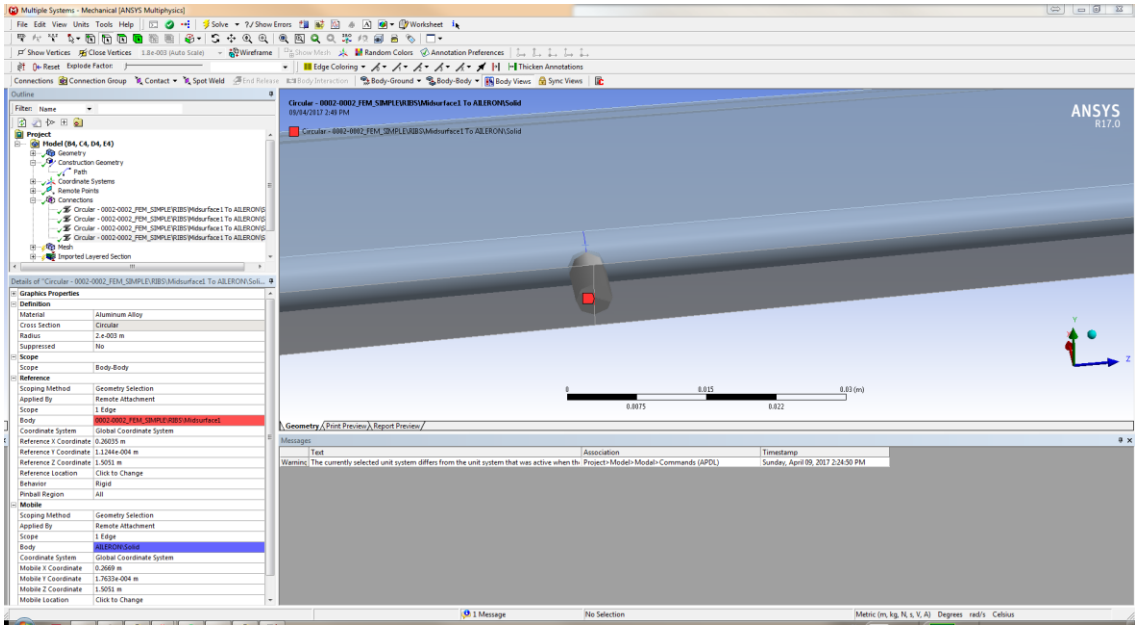

Figure 33: Aileron connection to wing

The winglet was attached by defining a rigid connection between the outermost rib surface and the winglet.

Several coordinate systems were added to the model including the following:

- Coordinate for each rib 1-4 where masses and inertia for wing skins are added
- Coordinate for gravity application. Note it is rotated to represent wings dihedral

Following addition of the coordinate system, masses representing the rib and composite panels was added at each of the appropriate coordinates and attached to the rib surfaces. Note the meshed ribs will be given a custom material property eliminating their mass so does not get summed twice. Some of the experimental tests were conducted with aerodynamic composite panels removed and for model comparison and fitting required the model to be able to be reconfigured with and without these components.

The model was meshed initially using the default adaptive mesh behaviour. It was found that this was unable to mesh the winglet with the initial tolerances set. Finer

meshes set in the curvature and proximity mode were found to form the best aspect ratio elements conforming nicely around the curves of the models skins and winglet, however they were unsurprisingly found to have a large element count. The defeaturing tolerance of the mesh application was set to a higher number allowing the mesh to not conform to the initial surfaces without failing. This appeared to only have an impact on the winglet and this feature was to be significantly more rigid than the remainder of the structure and this was acceptable.

A simple simulation of the structure where the root rib was bound with a fixed condition and a load was applied at the end of the cantilever rib in the Y axis (out of plane) was used to compare the meshes. Note that all material properties were aluminum with the exception of the winglet (custom material set to density to match weight of 13g, very stiff), aileron (custom material set to density to match weight of 120g, very stiff), rib 1-4 (weightless aluminum). The difference between these meshes was compared to evaluate difference in expected results pertaining to the meshes.

There are several mesh mode options in ANSYS MECHANICAL, and each have a number of parameters which change their behaviour. These values were tweaked and difference meshes configurations were explored. It was found that the greatest difference existed between the coarse mesh of Figure 42 and the fine mesh of Figure 43. The largest difference between the nodal displacements was 2%. The fine mesh however took over 100x longer to solve the static linear analysis and 30minutes to solve 6mode shapes using the ANSY lanczos modal solver.

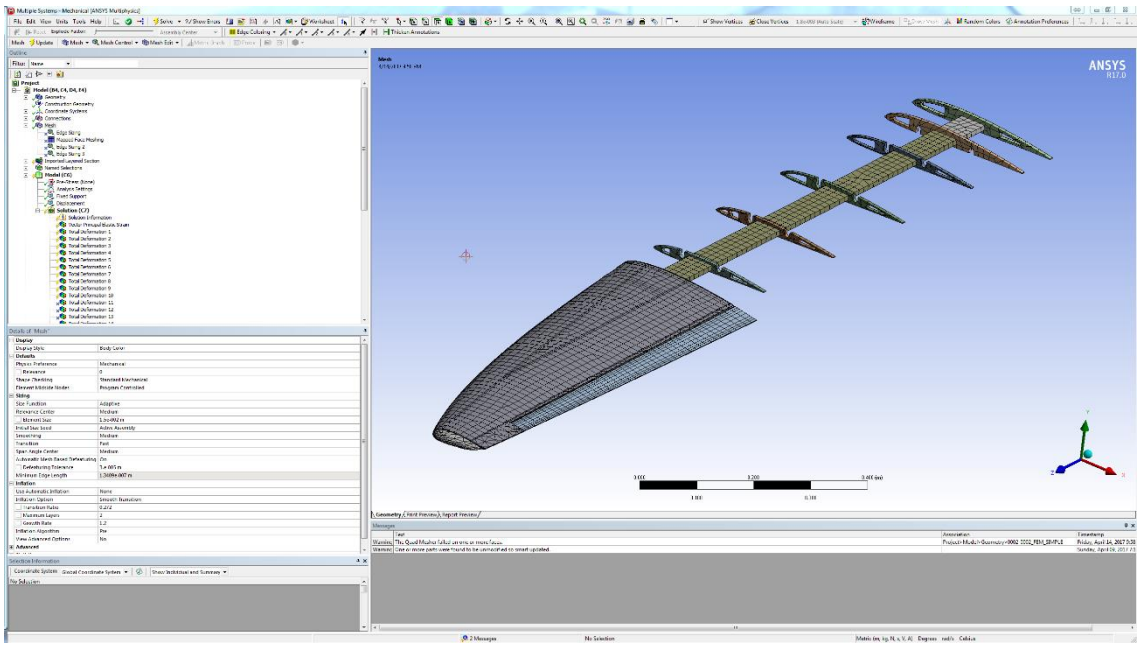

Figure 34: Sample coarse adaptive mesh results

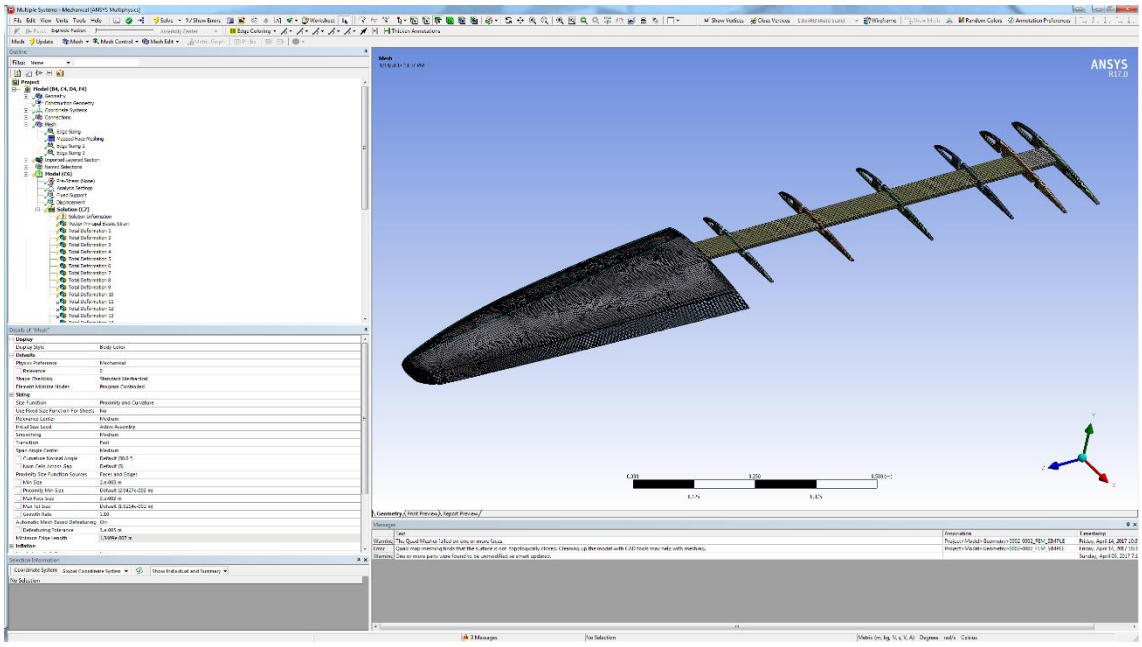

Figure 35: Sample fine curvature and proximity mesh

Ultimately a uniform mesh generation type was selected with a medium mesh density seen in Figure 44. This had a relatively close displacement <1% compared the Figure 43. Greater fidelity was required for strain in the aluminum spar to be used in implementing deformation measurement by SPA. This was accomplished by applying mapped quad elements mesh with edge sizing defined on the spar faces to increase the fidelity of strain results to be measured in latter experiments while maintaining a straightforward pattern to map for strain gauge implementation modelling.

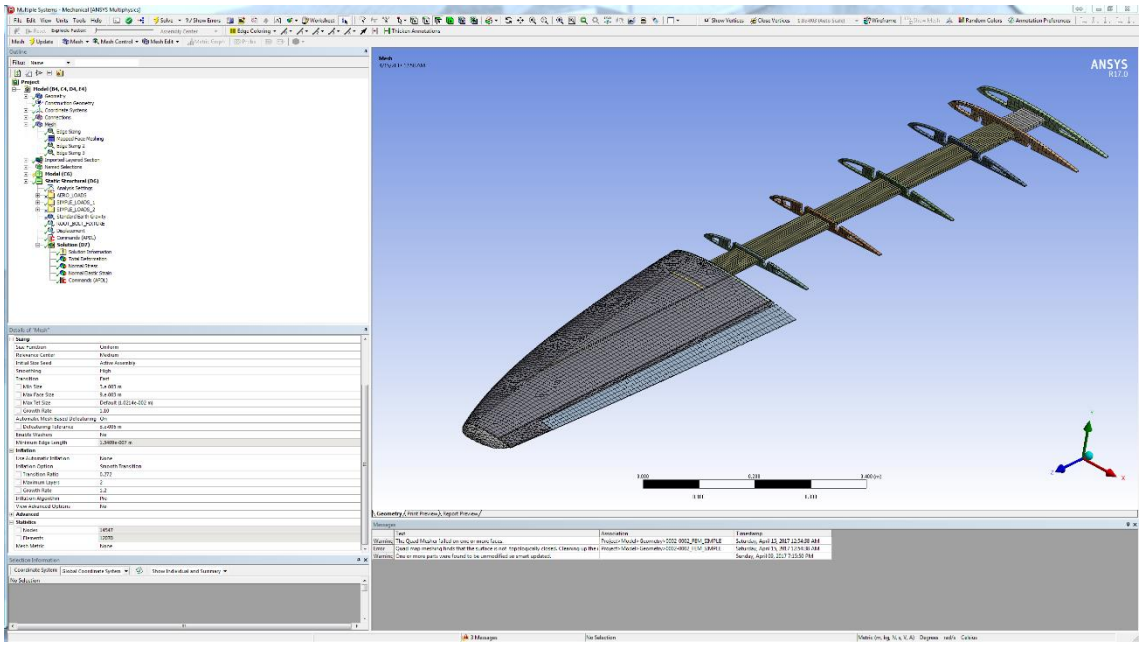

Figure 36: Final uniform coarse/medium mesh used in final FEM

The final mesh was comprised of quad shell elements along the spar, quad/triangle elements along the remaining surfaces, and tetrahedron elements in the winglet and aileron body.

Table 3: Mesh Quality Summary, Fine mesh used as quality (Q) baseline

Type	#Elements	Disp Q	Strain Q	Solution Time	Defeaturing Default
Coarse Adaptive	8917	2%	6%	1<min	relaxed
Fine Curvature/Proximity	158747	0	0	6min	Default
Medium Uniform with Mapped Spar	14547	0.5%	1%	1<min	Relaxed

3.3.3 Material Property Definition

The initial material properties applied in this model were either from default values inside the ANSYS database or input manually. A list of the materials are in Table 4.

Table 4: Initial material properties used in FE model design.

Material	Definition	E Type	E Final**	Density
Aluminum 6061 T6 (SAPA)	Matweb[64]	68.9GPa	65.0GPa	2770kg/m^3
Aluminum Alloy NO MASS	Matweb[64]*	68.9GPa	N/A	0.1 kg/m^3
ROOT_RIB_INNER_NO MASS	Matweb[64]*	68.9GPa	N/A	0.1 kg/m^3
ROOT_RIB_OUTER_NO MASS	Matweb[64]*	68.9GPa	68.7GPa	0.1 kg/m^3
ROOT_SPAR	Matweb[64]	68.9GPa	57.0GPa	2770 kg/m^3
STIFF WINGLET MASS	Estimate	50.0GPa	N/A	599 kg/m^3
STIFF_AILERON_MASS	Estimate	50.0GPa	N/A	1000 kg/m^3
Epoxy_Carbon_Woven_230GPa_Wet	CMH[65]	Ex59.2GPa Ey59.2GPa Ez	N/A	1451 kg/m^3
Epoxy-EGlass_Wet	CMH[65]	Ex35.0GPa Ey9.0 GPa Ez	N/A	1850 kg/m^3
SAN_Foam_103kgm3	ACP[66]	85.0MPa	N/A	103 kg/m^3

* Altered density to remove from model mass breakdown

**Material property altered to better fit the model to experimental data

The material aluminum is repeated in the material table for a couple of reasons. The first reasons was to allow “weightless” version to be applied to components such as ribs1-4 whose mass was accounted as a lump sum point mass. The inner rigid root section of the model was also not accounted for in mass as it was assumed this region would be rigidly bound. The second reason the material properties of aluminum was split was to allow the stiffness of individual parts to be tunable later in the optimization/update stage.

The STIFF WINGLET and STIFF AILERON properties were tailored so they could be applied to their namesake. This allowed final mass of the winglet and aileron to be matched with that of the part as built. This is how the density to volume was calculated.

The stiffness value was selected at random to be pretty stiff. Their stiffness had a small impact but could be tailored in the update/optimisation phase.

The composite materials were applied to the model using the ANSYS applied composite properties (ACP) toolkit. This toolkit requires that first the model be meshed with shell elements where composites are desired (quad or tri elements). ANSYS named selections, selected groups of elements, are defined for areas containing specific composite plys. With regard to the flexible ASE QT1.3 wing, the layup of the top and bottom was consistently the same. The shear webs had their own composite layup as well. Therefore, a named selection of surfaces was made of the upper rigid skins, bottom rigid skins, the trailing edges of the upper and lower skins, and the shear web components.

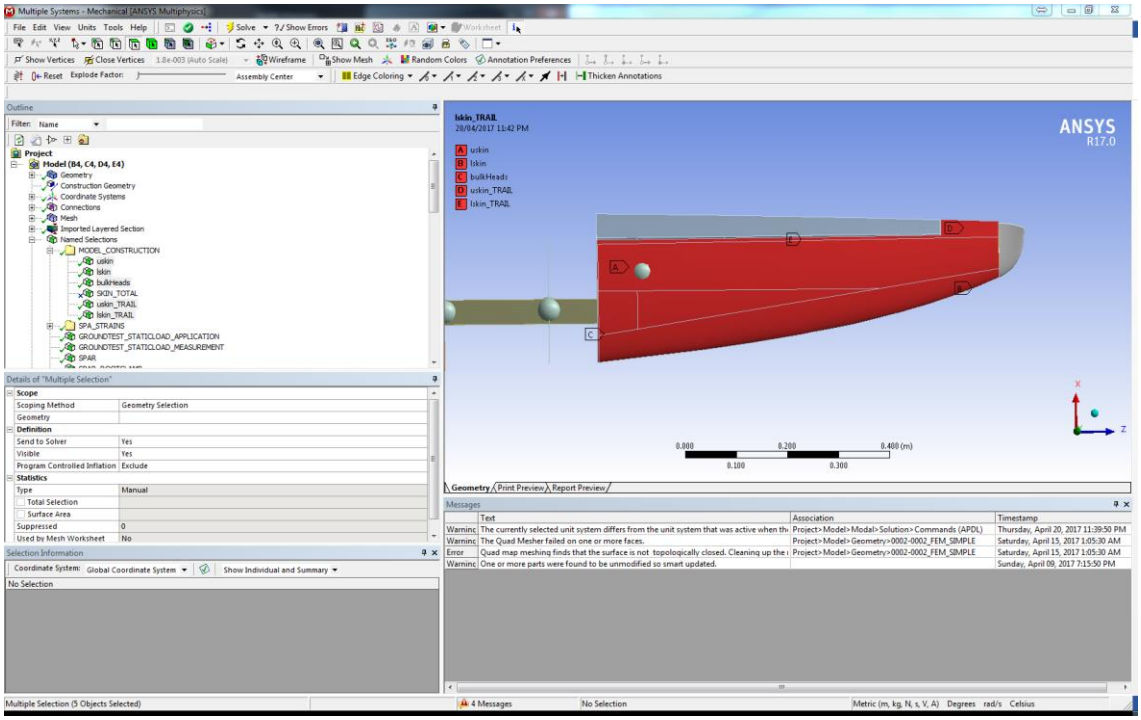

Figure 37: Named Selections for material definition in ACP

The ACP toolkit imports all the materials from the current project WORKBENCH, geometry and Named selections. The first step is to select the composite cloth materials to be used and define fabrics. The materials were given thicknesses in this step.

Layups respectively applied may be defined as a stackup. This is not necessary and is just an option to reduce repetition. Coordinate systems are referred to as “Rosettes” in ACP. The rosettes are imported from MECHANICAL. Additional rosettes may be added in ACP. They are used to define the orientation of the composites when applied.

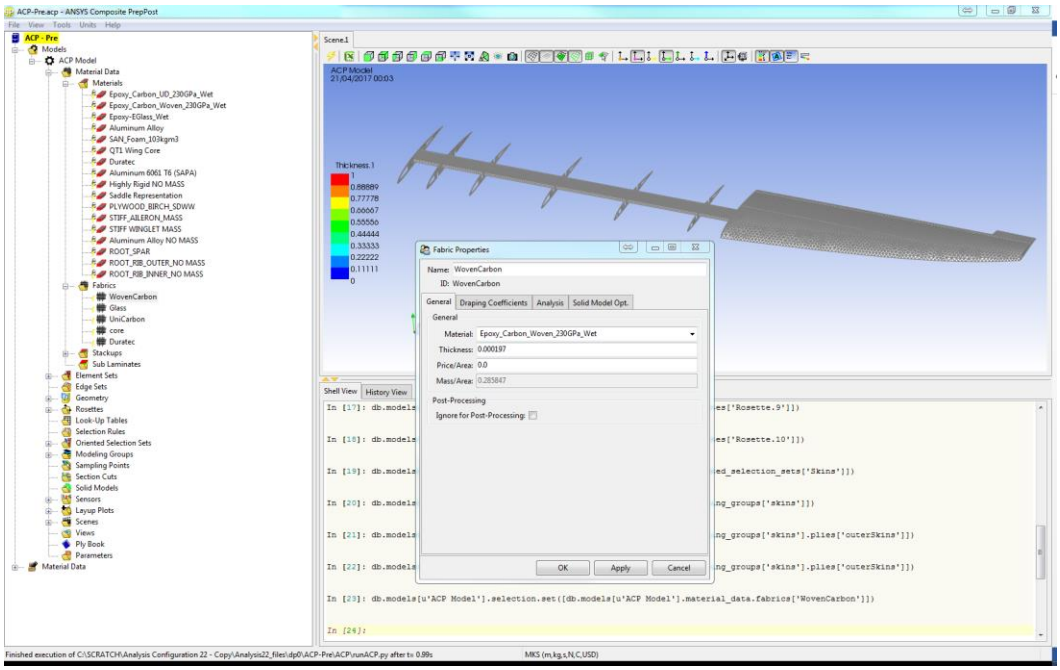

Figure 38: Composite fabrics defined prior to layup of plies

Oriented Selection Sets are made up of Named Selections of elements or surfaces which have been meshed, associated with a rosette for layup definition. An oriented selection set was made for the Skins (top and bottom), Skins_Trail, and shear web. Each set was made with respect to the global origin coordinate system rosette.

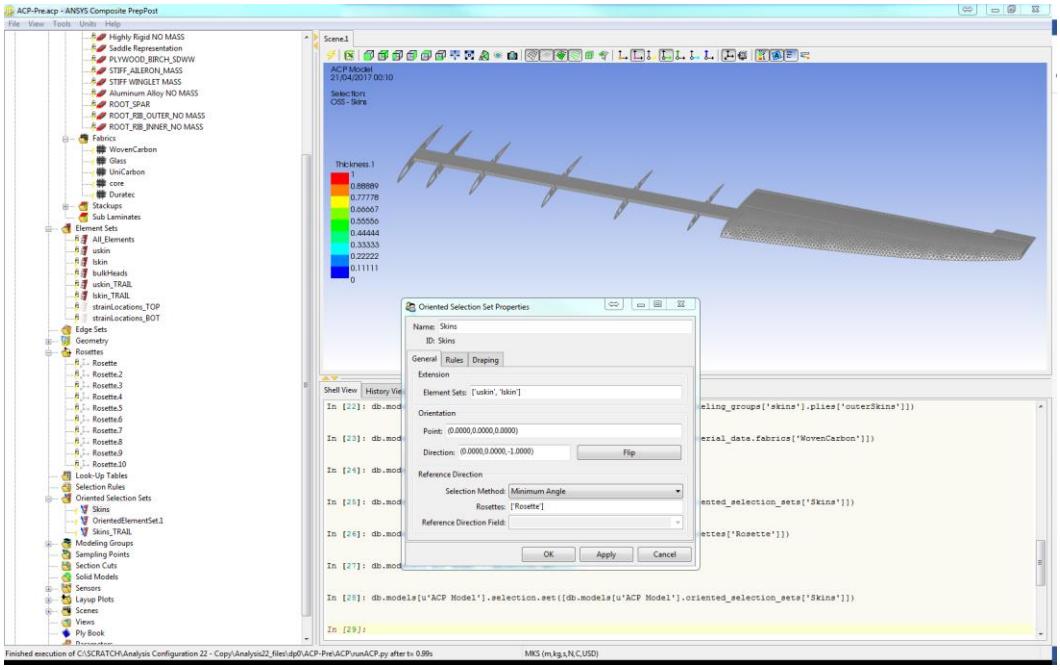

Figure 39: Oriented Selection Sets

The modelling groups tap is where individual layups or stackups are applied to Oriented strand sets. Here the plies are oriented relative to the applicable Oriented Selection Sets rosette.

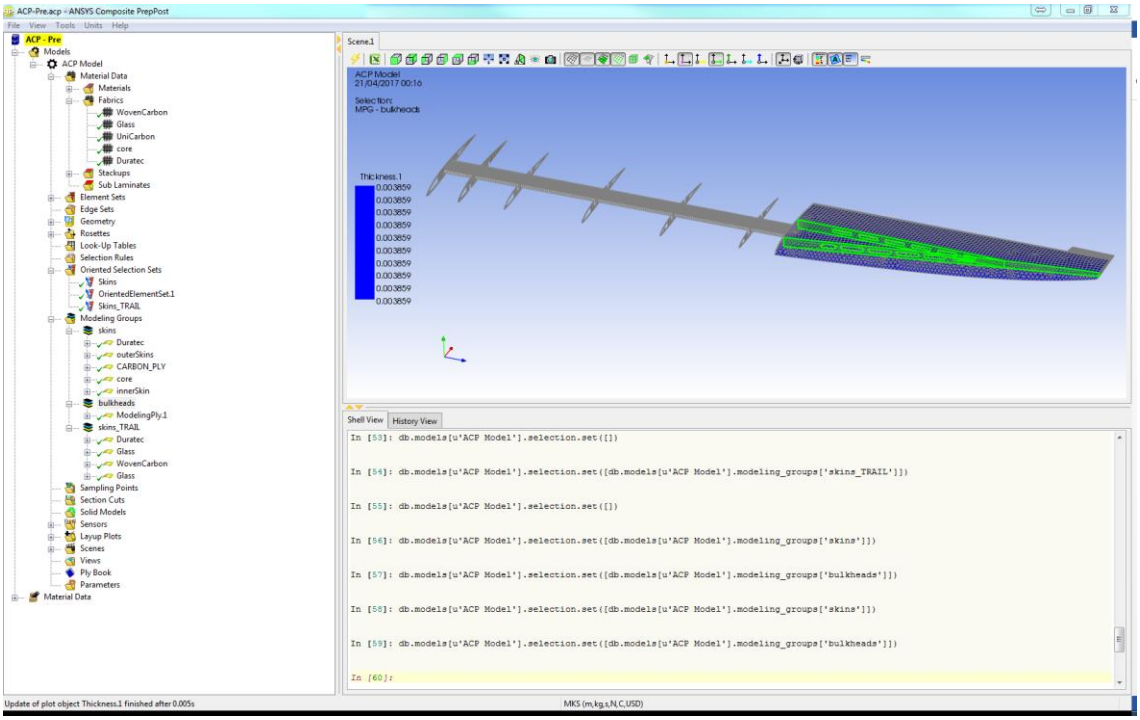

Figure 40: Modelling group of shear web layup

The final material layup schedule used (seen in Figure 46 modelling groups) may be found in Appendix A.

The sensor tab allows sensors to be placed to estimate weight, thickness, cost (if costing per yard added) and more. Additional tools not used appear to include tools for making documentation regarding the layup schedule, BOM, and costing.

3.3.4 Boundary Conditions

The boundary condition used in this model is that of a single fixed end cantilever beam. For experimental testing a segment of the fuselage of the aircraft was removed and bolted to a table for load testing of the wing and modal characterisation. Rather than model the segment of the fuselage, named the saddle, it was assumed to be an ideal rigid body. The rigid root portion of the wing had the following components constrained as,

1. Innermost rib had a fixed boundary (no displacement or rotation)
2. The second rib where the wing bolts attach the wing to the saddle had a displacement boundary in the x axis (no displacement in the in-plane axis)

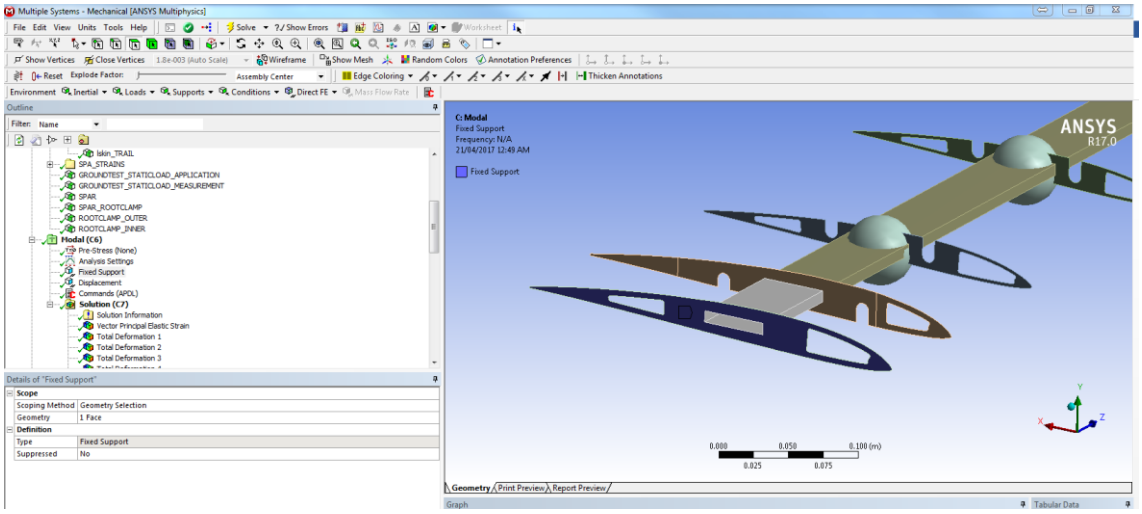

Figure 41: Fixed BC at the inner rigid root rib

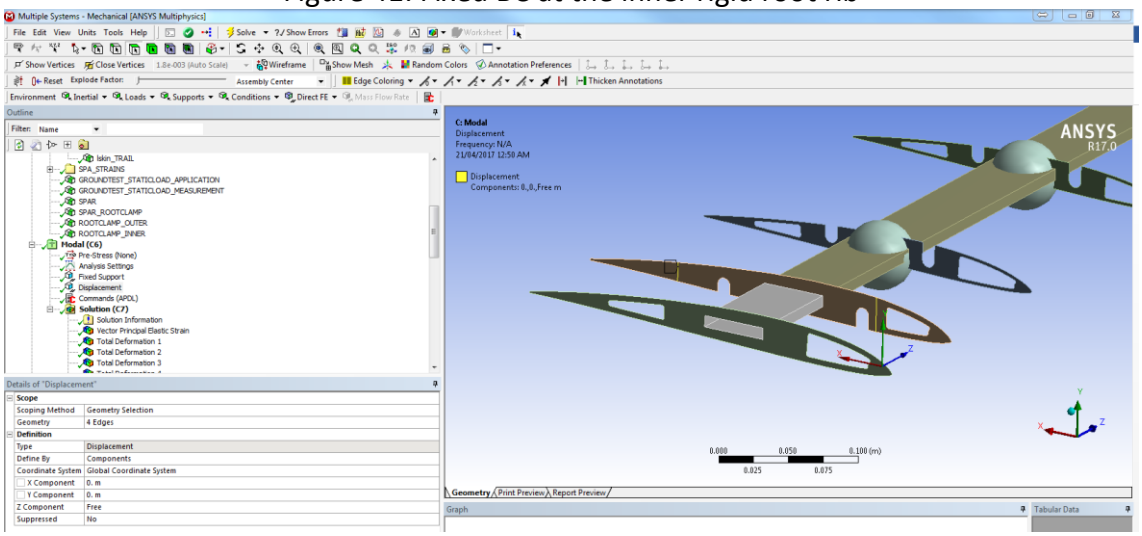

Figure 42: Displacement in X BC along outer root rib bolt lines

Note that the boundary conditions had been changed to better match the actual structural behaviours. Originally both conditions were fixed, but it turned out the saddle was not an ideal rigid body and does deform slightly when loaded. This caused a significant displacement error. By changing the boundaries to allow more compliance and adjusting stiffness of some parameters the model matched well (discussed further in Section 4.3).

Nodes in the model were selected for applying nodal loads were the static tests were conducted. These two nodes were saved and selected using a named selection. Note that all static load tests were loaded at these points.

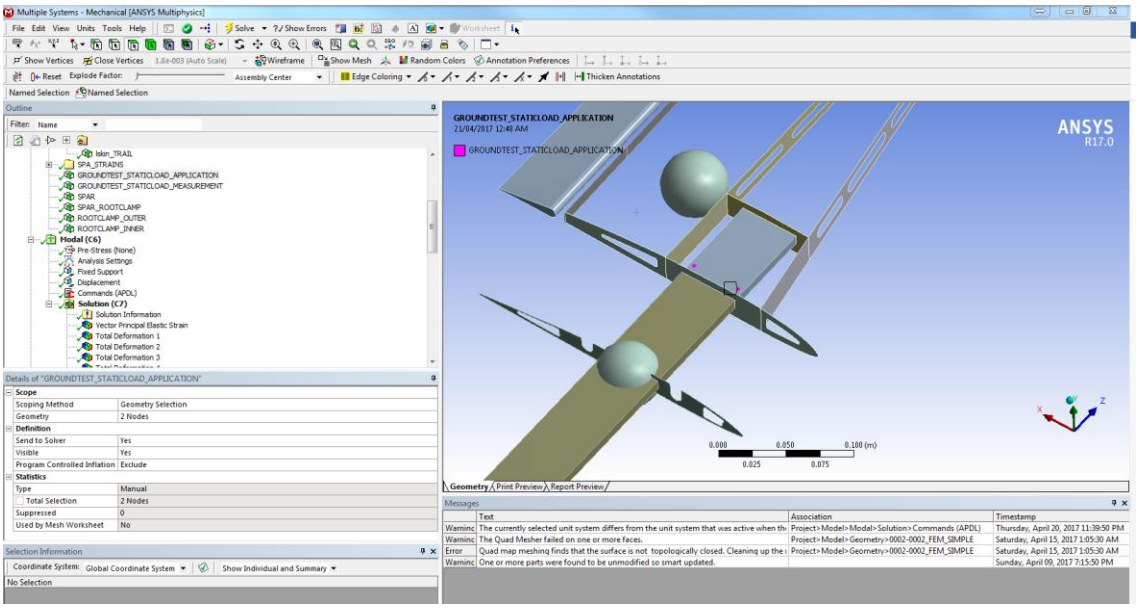

Figure 43: Named Selection of 2 elements for load application in static tests

3.3.5 STATIC AND DYNAMIC SOLUTIONS

The structural FE model was configured for a set of linear static solutions using a series of tests which would be later conducted experimentally. Simulated solutions were initially used to verify functionality of SPA method, and later validated model response against experimental results. Note that only the single load point test cases, described in section 4.1.1.1 were used for direct model validation and updating discussed in section 4.3.2. The output scripting for reference is in Appendix C.

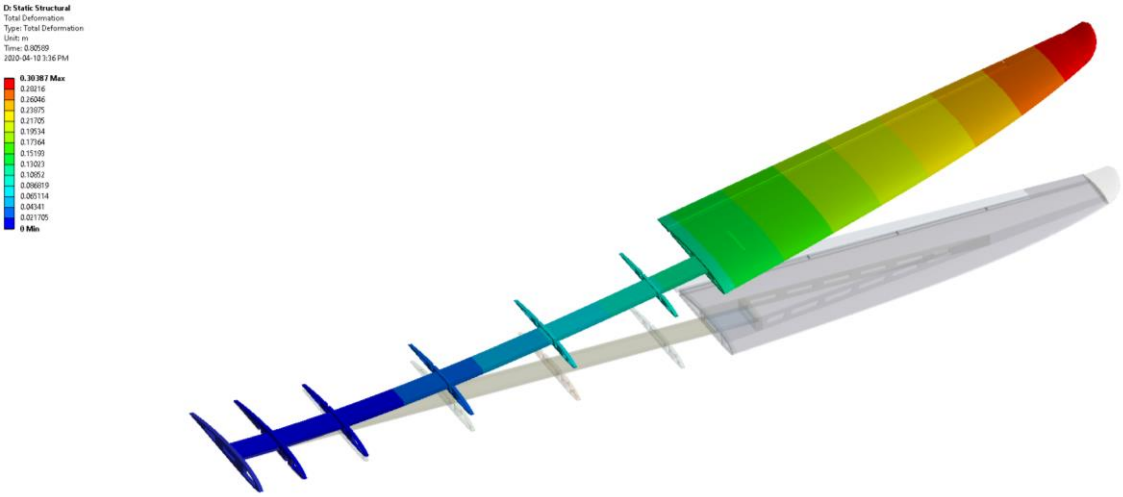

Figure 44: ANSYS FE model static solution. Distributed load condition similar to experimental distributed load case #5 described in section 4.1.1.2.

Likewise, modal solutions were completed using the same structural model using the ANSYS Block Lanczos method for the first 25 modal shapes. In practice less than 10 mode shapes were used to estimate the wing shape by SPA. Several modes are used to model validation and updating, discussed in section 4.3.3. The output scripting for reference is in Appendix D.

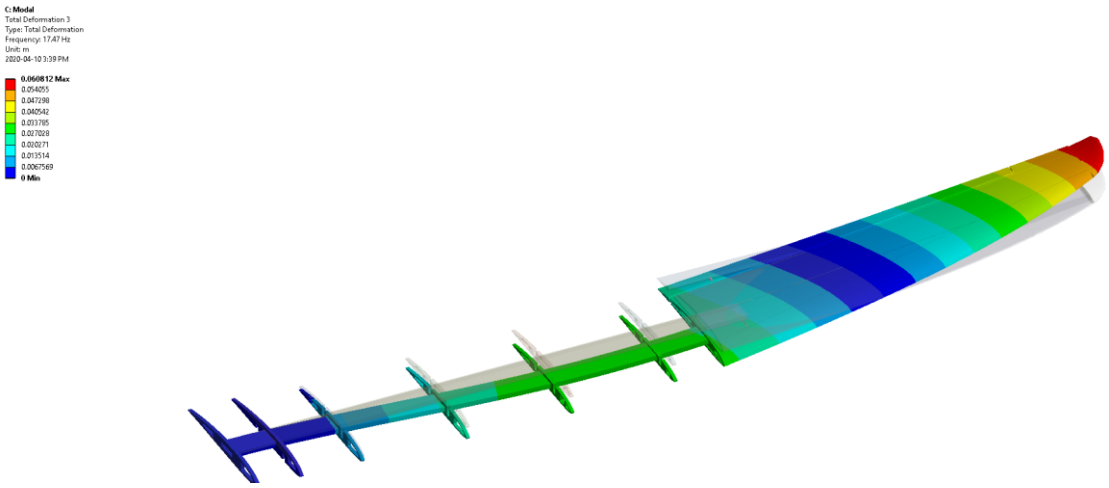

Figure 45: ANSYS FE model modal solution for the 2nd out-of-plane/flapping mode.

3.3.6 Post Processing

Named selections were made for nodes of interest to be written to files for use in both the deformation measurement by SPA and for model validation and updating. Primarily, groups of interest used for analysis included the upper and lower flexible spar surfaces (where strain measurements to drive the deformation measurement would be installed). Additionally, several specific nodes for experimental test correlation. These selections included five points along the spar, span wise, to validate displacement and allow model updating to optimize the FE models response. Note a selection of all nodal displacements were output to visualize the SPA deformation estimates at locations far from strain measurements, for example the wingtips.

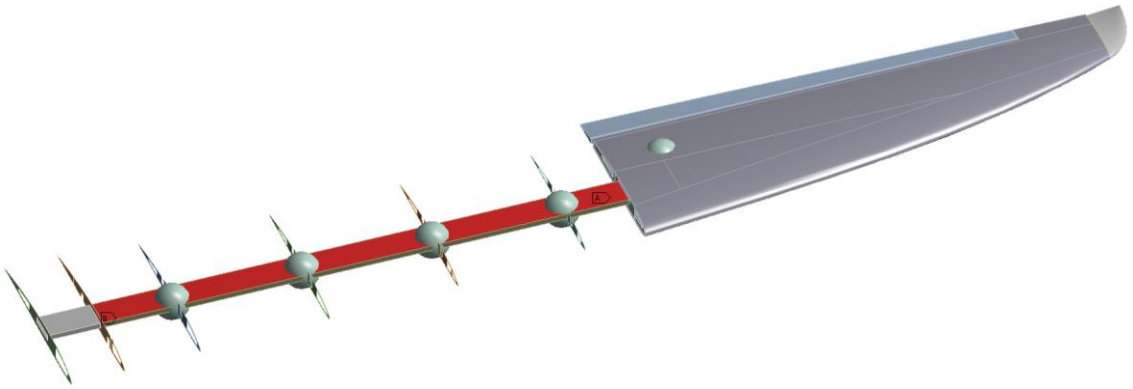

Figure 46: Name Selections of upper and lower surfaces on spar. These surfaces used to select and group both nodes and element selections for displacement and strain analysis outputs of specific model regions.

Commands were written to a script in ANSYS command line language APDL. These commands were intended for use in the post processor stage outputting nodes global coordinates relative to the origin, and the displacements of the nodes from the Named Selection in CSV format. Scripting used for writing outputs for static results are in Appendix C, whereas scripting for outputting simulated modal strain and displacement shapes is in Appendix D.

3.4 Instrumentation Flight Data Recorder

The selection and design of the instrumentation flight data recorder (FDR) was an important aspect of this project. Instrumentation had to not only meet the requirements for the deformation monitoring aspects but also acquire a number of other measurands, while remaining within the volume, weight, and budget constraints.

A platform based on National Instruments (NI) CompactRIO (cRIO) hardware was selected as the hardware core for the instrumentation system. The cRIO system is marketed as a controller with combination of onboard processor running a real time (RT) operating system (OS) and user programmable FPGA and generic expansion I/O slots which may be populated by NI, 3rd party, or the end user's own custom expansion cards. The NI product inventory for expansion cards, henceforward referred to simply as cards, offered a comprehensive set of I/O meeting the flexibility requirements for all the measurands types.

Measurands were from a diverse set of sources. Measurements included (but not limited to); conventional foil strain gauge bridges; IEPE accelerometers; serial stream from air data computer measuring angles of attach/sideslip; analogue voltages indicating control surface position feedback; and serial stream of body inertial

measurements. Measurements are highlighted in Figure 47. For a list of all measurands and their final specifications see Appendix E.

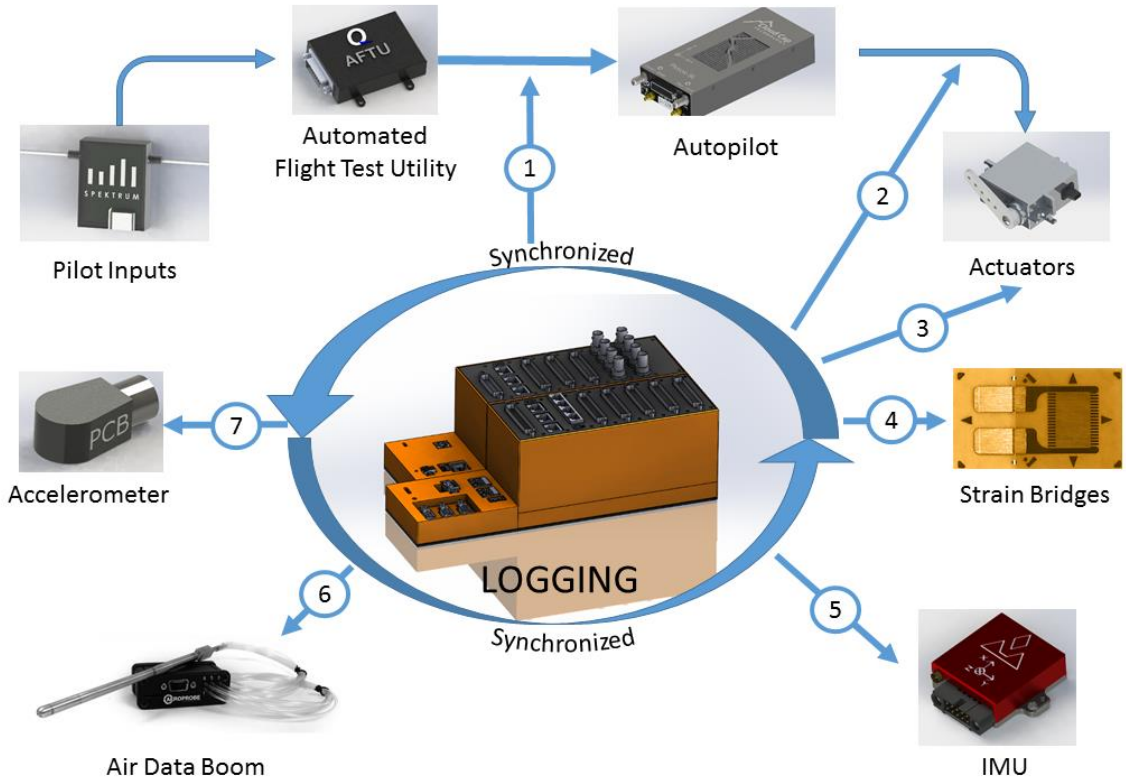

Figure 47: Measurand summary for ASE flexible wing aircraft instrumentation flight data recorder (FDR).

The FDR was programmed using several custom Labview applications developed specifically for this project. Primary applications included the RT, the FPGA, and Host applications. High level functionality such as external communication, control, and datalogging was built around a multi-threaded application using NI Labview RT which was compiled and deployed on the Linux operating system of the NI cRIO target. The FPGA, programmed using Labview FPGA, controlled the acquisition of measurements. The host provided user control and feedback. The software logic is depicted in Figure 48.

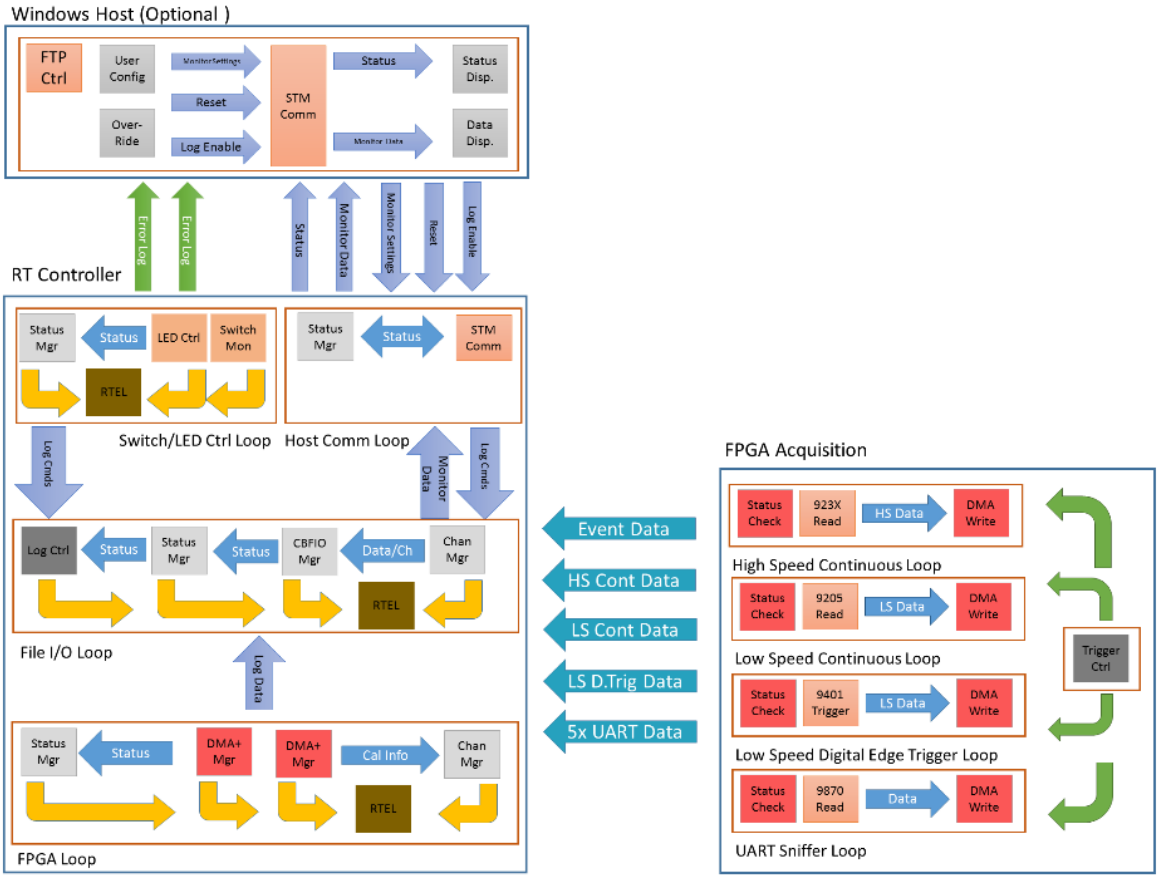

Figure 48: Instrumentation Flight Data Recorder acquisition application logic with remote host operation.

Strain and IEPE accelerometer acquisitions were designed to acquire data at 2KHz with all channels acquired simultaneously using a common synchronization clock source. Although the remaining measurements were not synchronized, all acquisitions were designed with time stamping based upon signal arrival in the FDR to enable easier comparison and analysis. An absolute time stamp was generated using the cRIO internal real-time clock (RTC) and the relative number of successive sampling loop counts. The RTC clock was reset from the linux real-time operating system using the network time protocol (NTP) daemon ntpd. From tests this maintained an absolute time source within <50ms over the course of 2hours. Even greater absolute time stamping was achieved by sampling the pulse per second (PPS) output from the autopilots global positioning system (GPS) sensor.

Control of the FDR was via one of two optional remote hosts, to enable a minimal low bandwidth interface or a higher bandwidth more feature rich interface. The low bandwidth option was over a serial port connection. This interface had a one second hearbeat message stating time, operating status, and operating mode. Controls included

starting/stopping logging, strain gauge measurement taring, and soft restart. This interface was passed through the aircrafts primary wireless communication link enabling remote operation from the ground during flight tests.

The higher bandwidth interface was over the FDR network controller. This enabled additional functionality including the ability to share/stream measurements, an FTP file server for downloading recorded data, and deployment/debugging of applications. This interface required attachment of a network umbilical cord which was used on the ground before and after flight tests to inspect instrumentation functioning properly.

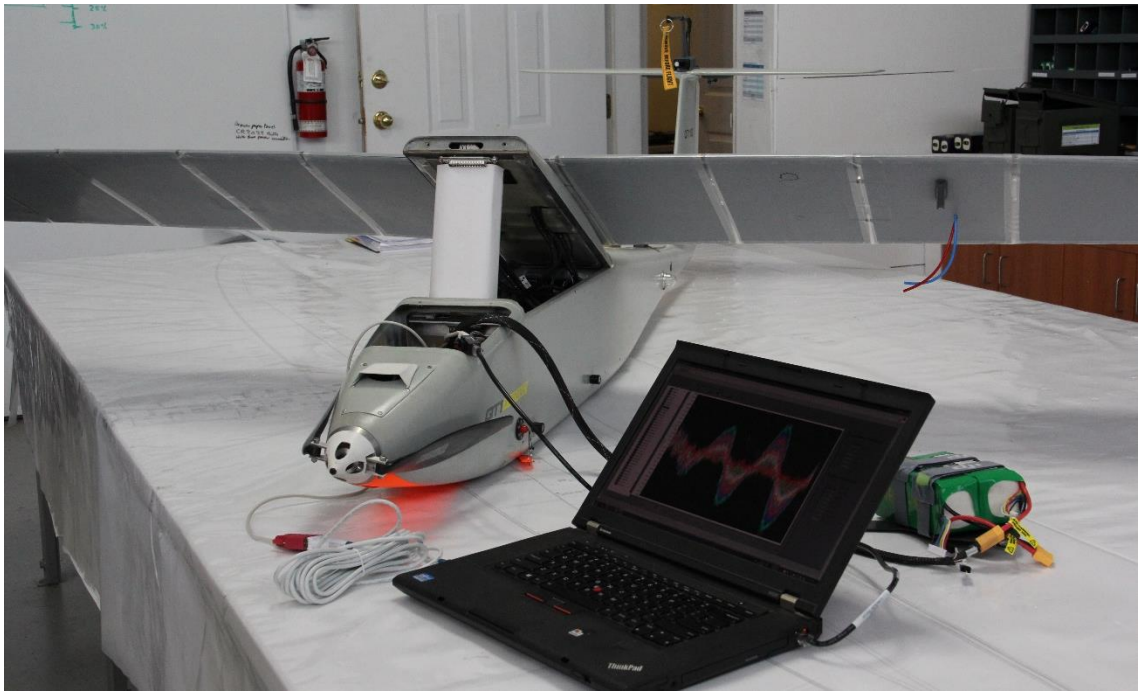

Figure 49: FDR test with live strain telemetry streamed via network connection to Host application on laptop. Note oscillations in strain indicating vibration in wings.

The enclosure for the FDR was redesigned to reduce weight and decrease the width sufficiently to allow installation of two cRIOs side by side in the QT 1.3 fuselage. The final design was rapid prototyped using 3D fused deposition modelling (FDM). Note that the final assembled part was finished in a conductive paint tied to the instrumentation ground plane, and analogue signal harness shields to protect against unwanted noise. Before and after renders from CAD of the FDR enclosure is seen in Figure 50.

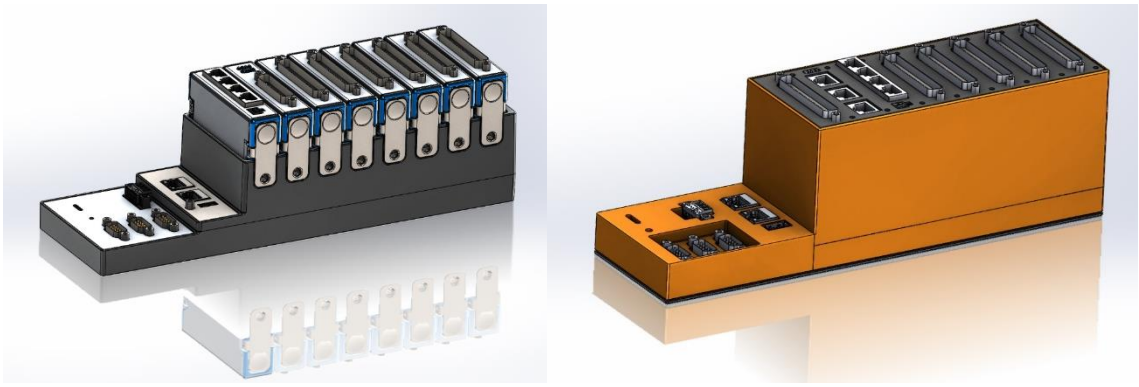

Figure 50: Custom FDR enclosure produced using 3D printing resulting in a 1KG reduction in weight.

3.5 Strain Measurement Design

A challenging aspect of SPA is avoiding potential pitfalls due to its sensitivity to ambiguity in the modal strain shapes. Achieving quality deflection measurements requires good modal strain identification. This is dependent on

1. Accuracy of the strain measurement,
2. Location of strain measurements and number of strain measuring locations,
3. Strain gauge bridge configuration.

These 3 elements form the properties necessary for the modal strain patterns.

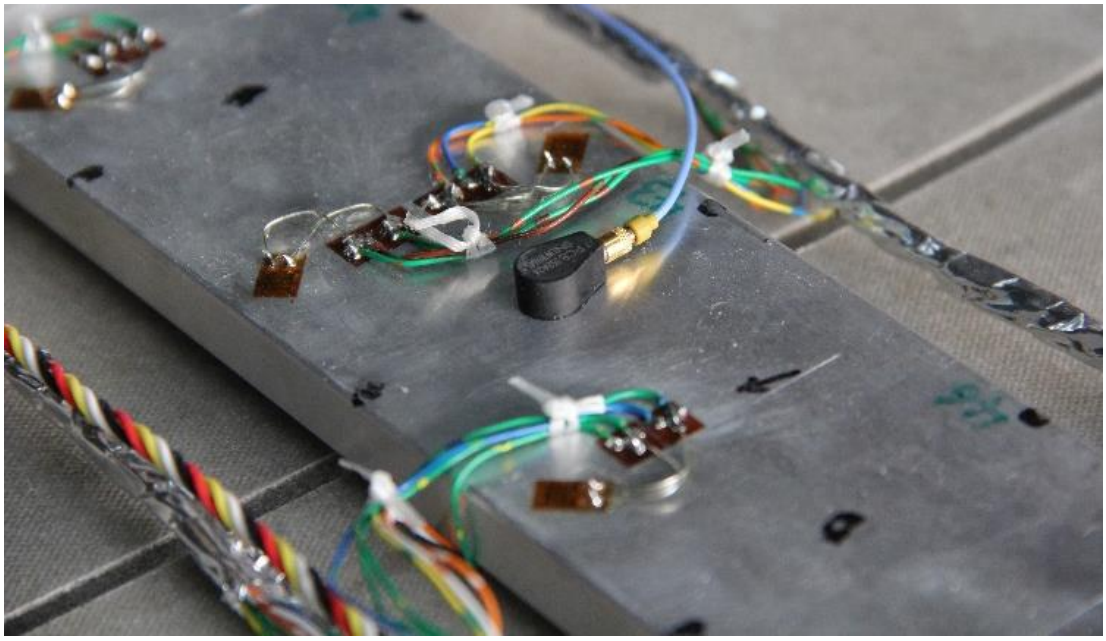

Figure 51: Foil strain gauge installation along flexible spar. Note application of conductive aluminum foil shielding around strain gauge harnesses which proved sensitive to RPA communication interference and required protection.

National Instruments 24 bit 50kS/s full bridge completion modules are used to attain strain measurements which are oversampled to attain ±1με resolution. These modules contain shunt resistors which are used to calibrate the bridges and account for harness resistance. Micro Measurement CEA-13-062UW-350 linear pattern foil strain gauges are used. The dimensions of the gauges are 5.59mm long x1.5mm wide seen in Figure 5. Note that only strain bridge configurations are considered with capacity to remove unwanted temperature effects are considered. Variations of a beam bending bridge is used, whose circuit implementation is described in Appendix F.

The design of the flexible portion of the wing results in most of the deformation of the wing to be the spar and not the skins. A limited amount of area is available along the spar for instrumentation. Four bridges are placed between each rib and equally spaced as a compromise due to limited space at this scale.

Although it was found that a reasonable number of mode shapes for rebuilding strain shapes could be achieved with 8 gauges, spacing constraints and redundancy in case a bridge failed in flight testing led to the adoption of the maximum number of 16 bridges. The additional 8 gauges results in improved shape resolution and lowered sensitivity to errors in measurements. Optimal location for bridges appears to be at mode anti-nodes. It was found that a gauges spread linearly spanwise aligned reasonaly for out-of-plane/flapping modes, and along leading or trailing edge was best for twist estimation.

Note that little emphasis was made to measure in-plane/lead-lag movement, and is presently ignored.

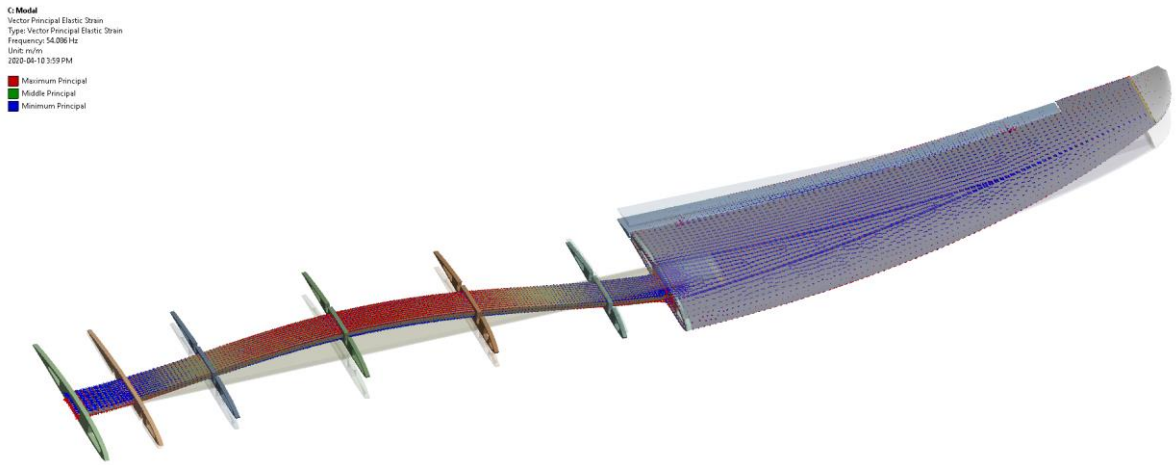

Figure 52: Peak strain locations for the 3rd out-of-plane/flapping mode. Consider absolute (ie both red-maximum, and blue-minimum) conditions as optimal measurement locations for this mode. All shapes favoured strain measurements near the wing root.

The last criterion, strain gauge bridge configuration, is useful in developing strain patterns which demonstrate linear independence. This is important in equation (5) while solving the least squares equation to develop an accurate displacement estimate. Consider if strain were measured along the spar sequentially using strain gauge bending bridges oriented parallel to the span of the spar the strain pattern would be as seen in Figure 53A. Note the ambiguity between the 1st out-of-plane and 1st torsional elastic modes.

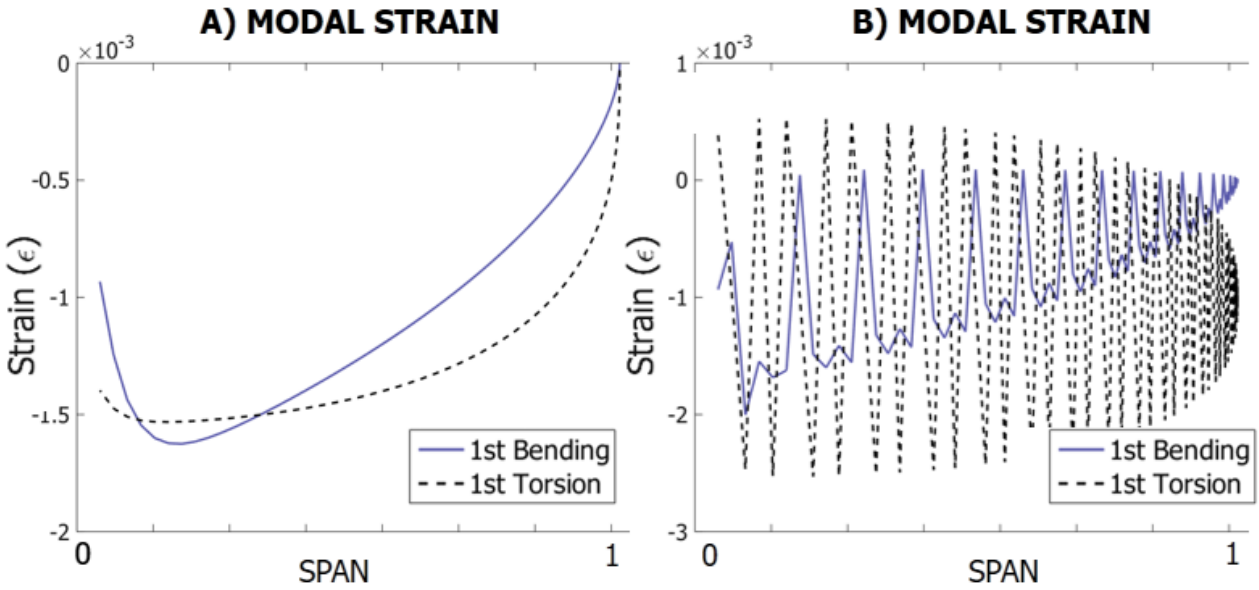

Figure 53: A) Modal Strain Patterns for fundamental 1st Bending and 1st Torsional elastic modes on spar with strain bending bridges parallel to span. B) Modal Strain Patterns for fundamental 1st Bending and 1st Torsional elastic modes with Gauges installed in repeating pattern shown in Figure 54.

To remedy this while maintaining sequential spanwise measurements the strain bending bridges are mounted on the wing spar with alternating rotational offsets as seen in Figure 54 and Figure 55. Here, strain gauge orientations are alternated ±90 degrees as originally proposed by Nicolas Tourjansky and Edmon Szechenyi [67]. As a result, a better, more uncoupled bend/twist strain pattern can be achieved as demonstrated in Figure 53B. (This corresponds to the installed configuration in which the gauges are installed on the wing with the following alternating pattern A-B-C-A-C). Note the schematic for the installation of all strain gauges is in Appendix G.

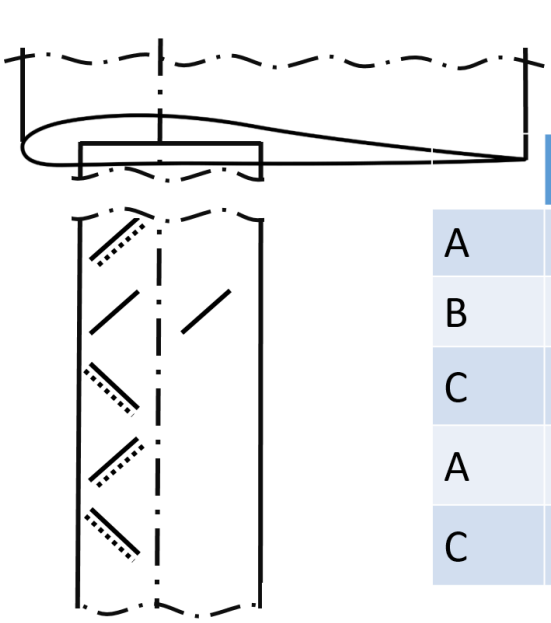

	In - Plane	Out of Plane	Torsion
A	0	-1	-1
B	1	0	0
C	0	1	1
A	0	-1	-1
C	0	1	1

Figure 54: Repeating strain bending bridge pattern applied to flexible wing.

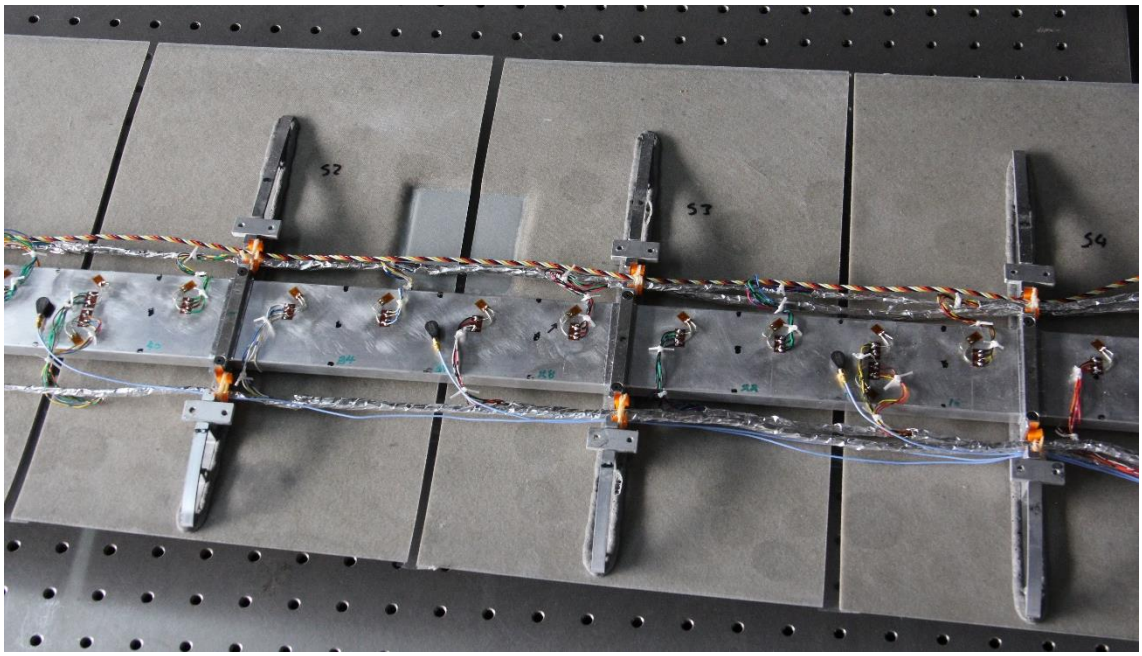

Figure 55: Repeating strain pattern as installed. Note installation of 3 single axis IEPE accelerometers for wing flapping measurements simultaneously with strain.

3.6 Deformation Measurement Simulation

The deformation measurement by SPA method implementation was iterated and verified using the same FE model designed to derive the required modal strain and displacement shapes. Dataset manipulation and implementation of the deformation measurement by SPA method was completed using Mathworks Matlab. An example script is referenced in Appendix H.

A number of static test cases were solved which were representative of experimental tests completed. Note that for this section, the static load cases have since been revised to match conditions experimentally tested. Cases presented here are those that align with single load point experimental cases (seen in section 4.1.1.1 Table 6).

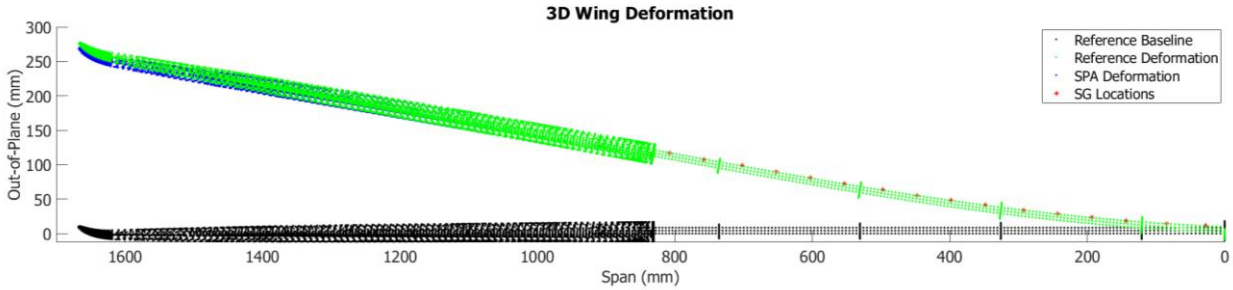

Figure 56: Front view projection of out-of-plane wing deformation by SPA using simulated FE model linear solver. Case presented is based on single load point, test 5, which is an equivalent bending moment applied at the flexible aluminum spar root for a 2g pull-up manoeuver. Note flexible spar aerodynamic skins not present in plot.

Reconstruction of the out-of-plane wing shape for the single load point test 5 is presented in Figure 56. The single load point cases 1-5 each have the same test conditions with an increasing applied static load. Note for this case the static solver in ANSYS was configured for linear solutions.

When considering out-of-plane load cases at the single load point good agreement is observed when comparing deformation by SPA estimation against the deformation reference (reference in this section referring to static deformation results numerically calculated from the FE model as opposed to experimental measurements). Deformation error is assessed as,

$$e = \delta z^{/} - \delta z \qquad (21)$$

where e is the absolute error (in millimeters), $\delta z^{/}$ is the reference change in out-of-plane displacement, and δz is the SPA estimated displacement delta. Percent error is e divided by $\delta z^{/}$.

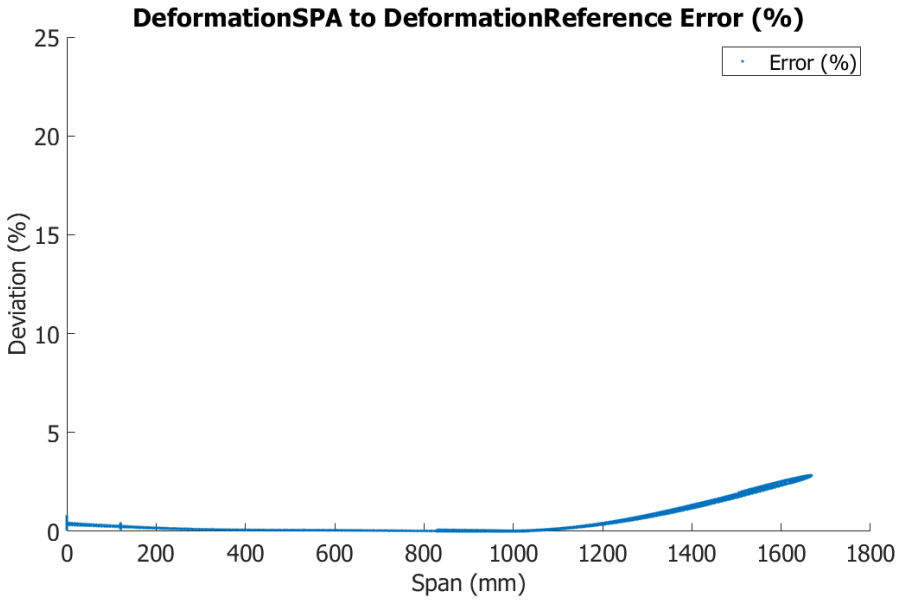

Figure 57: Deformation error % relative to reference displacement for out-of-plane/flap direction in simulated FE model single point load test 5. Note discontinuity in slope occurs where point load applied at start of rigid wing section.

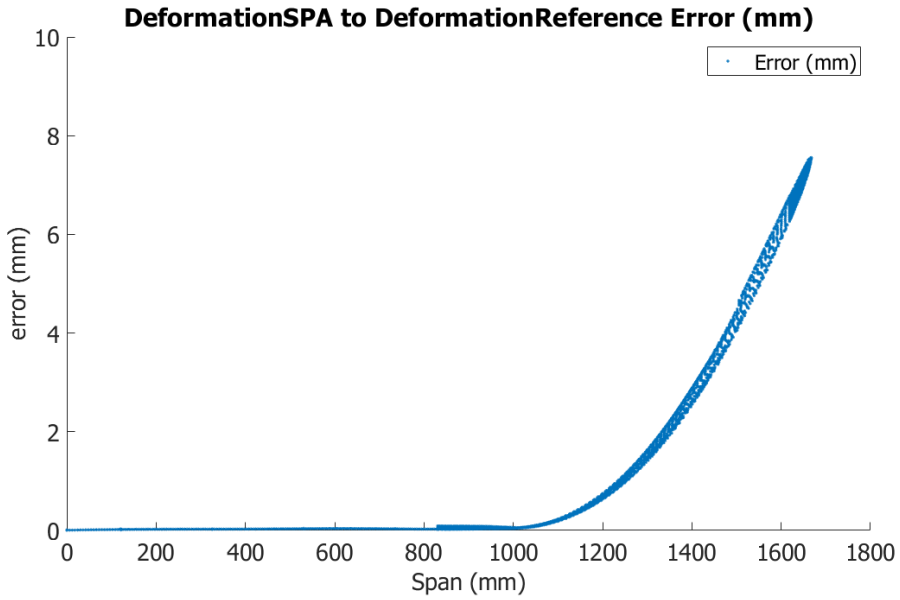

Figure 58: Deformation error in mm relative to reference displacement for out-of-plane/flap direction in simulated FE model single point load test 5.

Deformation error, Figure 57, and deformation error percent, Figure 58. Note best fit is achieved for the instrumented portion of the wing, the flexible aluminum spar. The single load point test case emphasizes the lack of load observation in the outboard wing where the error is greatest. Nonetheless the comparably rigid composite structure prevents accumulation of error greater than 5%.

Seven mode shapes are used for the linear combinations of equation (2). Strain pattern and fit for single load point test 5 is plotted in Figure 59. Best stability was found using the out-of-plane mode shapes and torsion/twist modes.

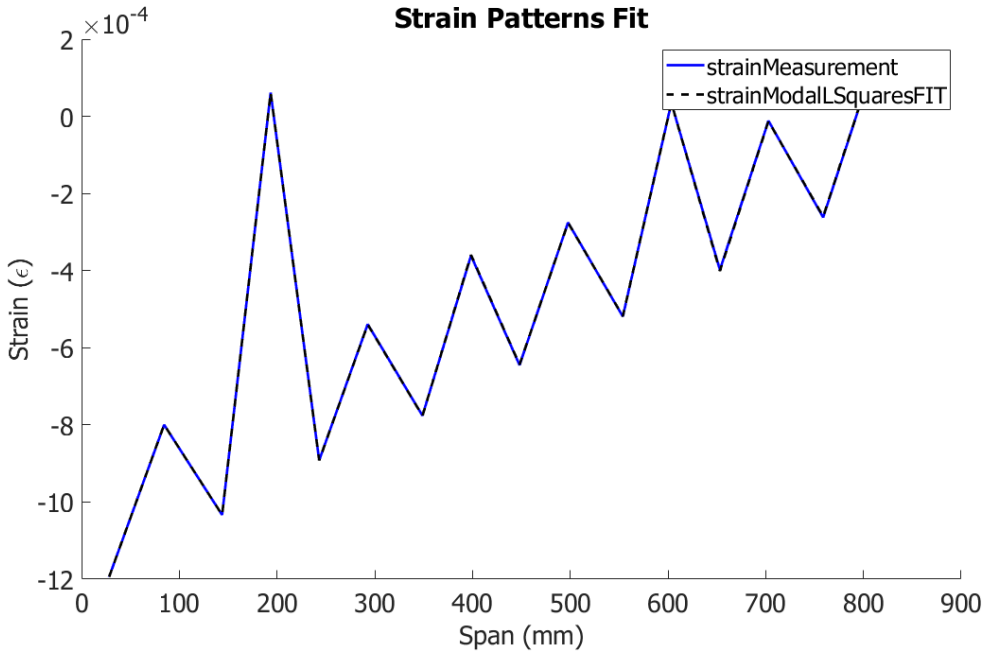

Figure 59: Strain modal linear combination fit relative to measured strain for the single point load test 5.

The five single point load static cases tested numerically using the FE behaved linearly. The percent error, normalized against the reference displacement is consistent for each test case. Results are summarized in Table 5.

Table 5: FE model verified Out-of-Plane/Flap deformation measurement at end of flexible aluminum spar and wing tip. Load cases are the static single load point cases 1-5. FE model static solutions are linear.

		Error (mm)		Error (%)	
#	**SP Load (g)**	Span 930mm	Span 1750mm	Span 930mm	Span 1750mm
0	0	0.00	0.00	0.00	0.00
1	0.4	0.006	1.50	0.02	2.90
2	0.8	0.012	3.10	0.02	2.90
3	1.2	0.017	4.50	0.02	2.90
4	1.6	0.020	6.00	0.02	2.90
5	2	0.028	7.50	0.02	2.90

Chapter 4- Experimental Testing

4.1 Static Load Testing

A series of static load tests were conducted on components of the ASE QT1.3 FTV to provide information for verification of the FE modelling and deformation sensing by SPA. In these experiments the structure was intentionally deformed in several configurations with varying loads and distributions. From these tests loads, deformations, and strains were all sampled. A series of static test cases using single point loads may be seen Figure 60.

Figure 60: Single load point, symmetric static load testing of the wing.

In each case the strain gauges on the wing were connected to a bench top National Instruments data logger, while the wing saddle was clamped to the test table. A Labview application was designed to record the measurements from all of the strain gauges on each wing semi-span. The data acquisition unit was tarred such that any measurement bias and gain errors were eliminated and a soft zeroing measurement was done in each case prior to applying any load.

Reference deformation results were compiled into a UFF58 format for comparison against FE static and modal results using a correlation and optimisation tool named FEMtools.

4.1.1 Load Cases

Tests conducted can be split into two different groups. The first group of tests was conducted with loads applied at a single point at the end of the flexible spar. The second group of load cases was conducted with distributed set of application points. Data from the single load point cases was primarily used for static structural updating, whereas the distributed load cases where used for validation of the deformation sensing using SPA.

4.1.1.1 Single Point Load

The single point load tests were designed to provide data for model validation and updating if required. For this test the wing roots were attached to the wing saddle, which was then fastened to a steel table top. The out of plane bending loads were applied at points (134.72mm, ± 943.57mm, 37.98mm) with the leading edge of the wing at the root being (0mm, 0mm, 0mm) as seen in Figure 61.

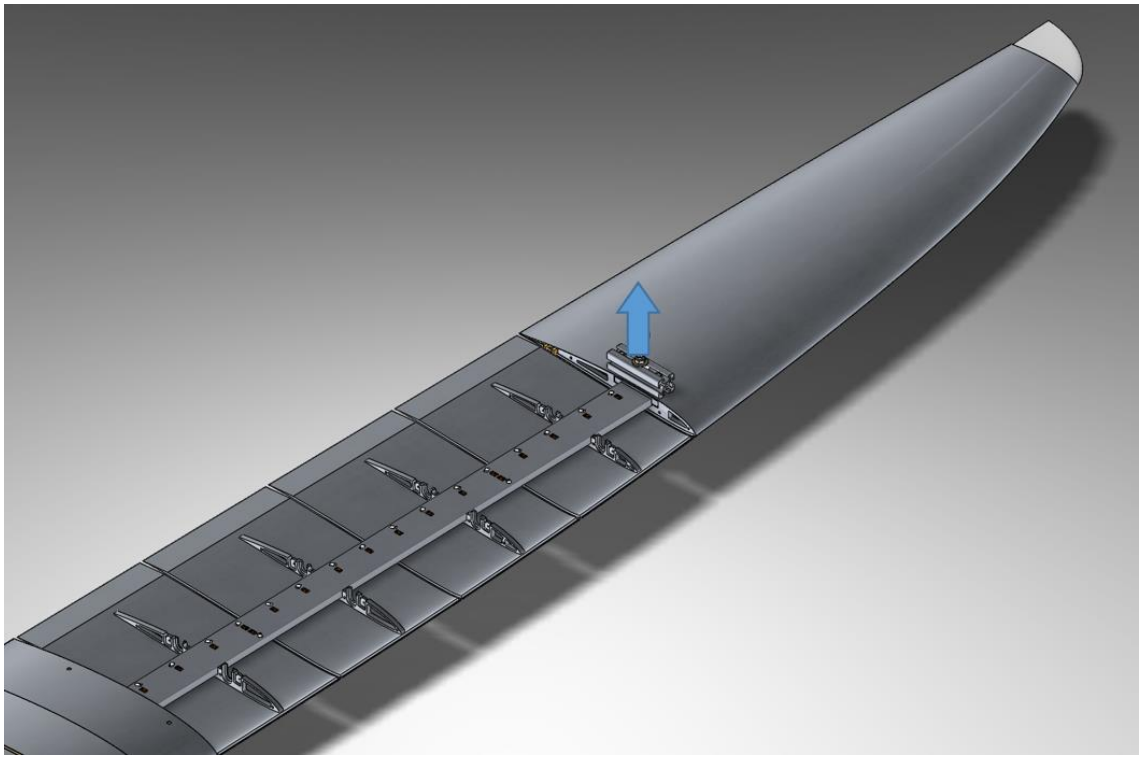

Figure 61: Single load application point sized using an equivalent bending moment at wing spar root.

Follower forces were not used and the load was always perpendicular to the test table. Six load cases from 0N to 78N (roughly equivalent to a 2.1g pull up maneuver bending moment at the wing root) were applied. These are listed in Table 6.

Table 6: List of single load application tests. Loads are scaled around an equivalent bending moment at the wing root. Test are pure out-of-plane/flap bending.

Test	Load\Max.Load		Equivalent Pull Up
0	0	%	0
1	20	%	0.4 g
2	40	%	0.8 g
3	60	%	1.2 g
4	80	%	1.6 g
5	100	%	2.0 g

Testing procedure started with the baseline shape, the 0N load. Reference displacement was determined by measuring the height of predetermined points of interest on each wing from the test table. In Subsequent tests, height relative to the table top was measured as seen in Figure 62.

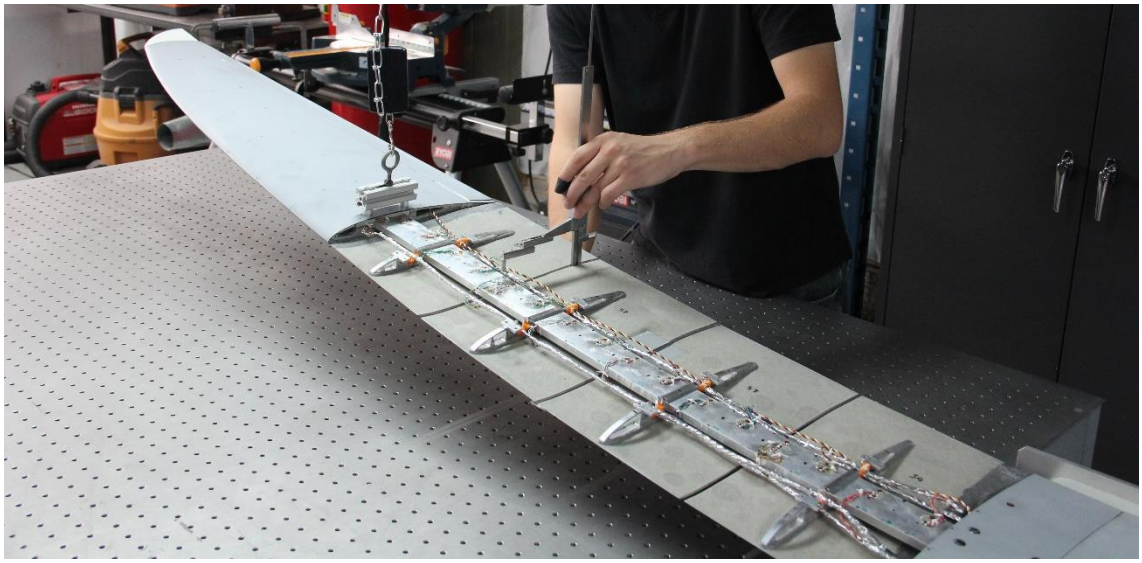

Figure 62: Deformation of wing measured as displacement of a point from table top using calipers.

4.1.1.2 Distributed Load Case

The distributed load cases were designed to further validate the deformation measurement system. The data sets provide a greater number of deformations closer to what is expected to be seen in flight. These data sets were also used for the validation of a single camera VMD displacement measuring method subsequently used at UVic CfAR for other project applications [27].

The tests were designed to have a maximum load equivalent to a 1.7g pull-up manoeuver. A limiting constraint was keeping the bending moment where the flexible spar interfaces the rigid root below its yield limit. A pseudo-elliptic lift distribution was used to approximate the lifting loads. The continuous lift distribution was then discretized into 5 span wise locations, 4 on the flexible spar and 1 on the rigid composite section. Each span wise location was split into two chord wise application points with a leading edge, and trailing edge application point as seen in Figure 63.

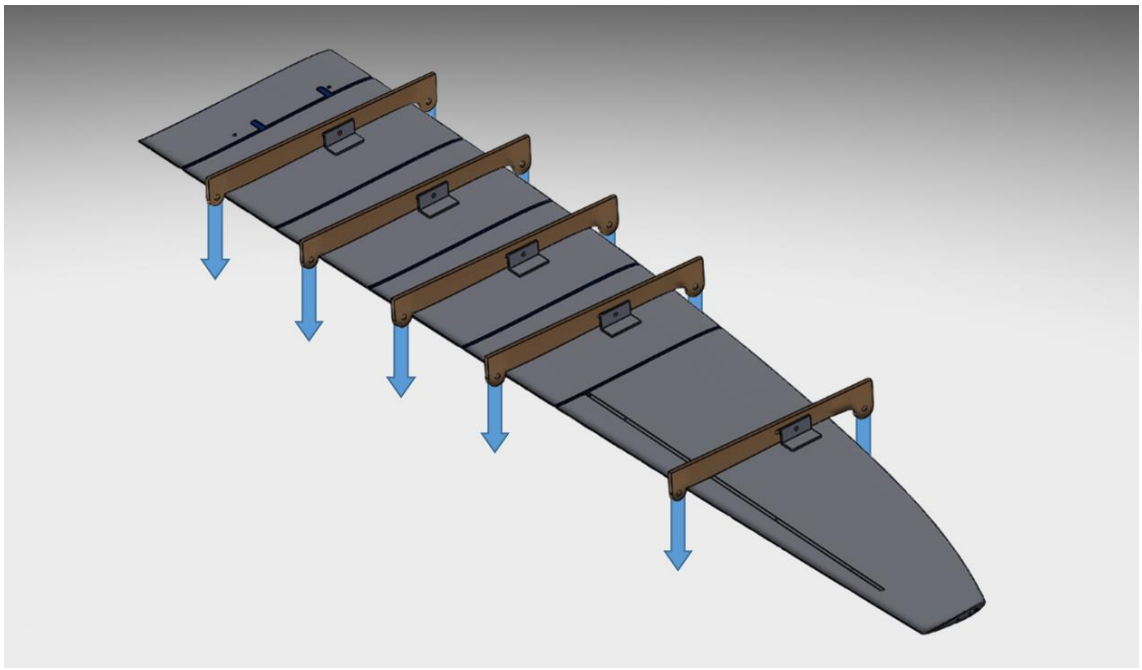

Figure 63: Distributed load test set up with 5 span wise by 2 chord wise load application points.

A total of nine distributed load test cases were completed. The pure bending test cases with discretized elliptical load profile are fractional cases to the maximum case of a 1.7g pull up equivalent manoeuver. These are listed in Table 7.

Table 7: Pure bending distributed load test cases with max load 1.7g equivalent pull up. Test 5 was not completed.

Test	Load\Max.Load		Equivalent Pull Up
0	0	%	0.0 g
1	40	%	0.7 g
2	55	%	0.9 g
3	70	%	1.2 g
4	85	%	1.4 g
~~**5***~~	~~100~~	~~%~~	~~1.7 g~~

Several additional tests cases, based on permutations of loads applied for test cases 1-5 were also conducted. This allowed several combined bending and torsion cases to be produced. All distributed test cases are in Table 8. Note test 5 was not completed due to concern in damaging the test article.

Table 8: Planned masses applied for individual test distributed test cases. Masses are in grams. Span 1 is closest the wing root. A mass of 0 indicates no mass applied. Test 5 was not completed.

Test	Span 1		Span 2		Span 3		Span 4		Span 5	
	LE	**TE**	**LE**	**TE**	**LE**	**TE**	**LE**	**TE**	**LE**	**TE**
0	0	0	0	0	0	0	0	0	0	0
1	378	303	249	184	224	151	195	125	249	128
2	688	552	471	348	434	293	397	225	840	430
3	998	800	692	511	645	435	599	385	1430	732
4	1308	1049	914	674	855	577	801	515	2020	1034
~~**5***~~	~~1618~~	~~1297~~	~~1135~~	~~838~~	~~1066~~	~~719~~	~~1003~~	~~645~~	~~2611~~	~~1336~~
6	998	800	0	0	0	0	0	0	0	0
7	0	0	0	0	0	0	0	0	1430	0
8	0	0	0	0	0	0	0	0	0	732
9	0	0	0	0	0	0	0	0	1430	732

The reference displacement measurements taken during the distributed load tests differ from the procedure in the single load cases. The reference deformation measurement of the structure was from scans of each load case using a Creaform metrology 3D scanner, an optical coordinate measuring machine (CMM). Capture of one of the tests was as seen in Figure 64.

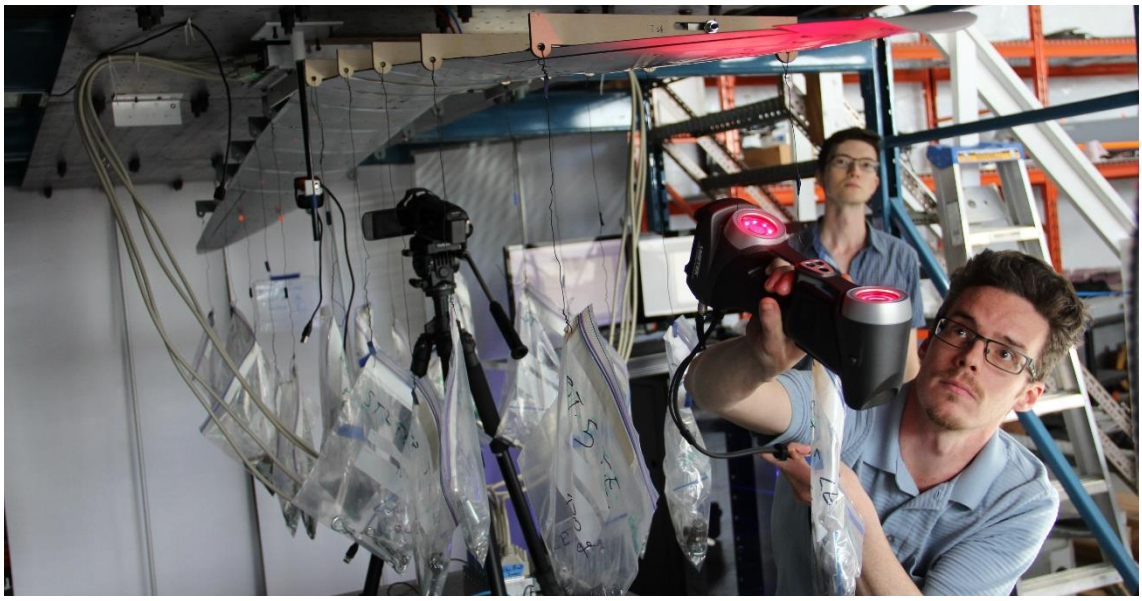

Figure 64: Distributed load test case with metrology 3D scanning for wing displacement reference measurement.

To enable easier data management a series of acquisition fiducials were placed on the structure at locations common to nodal positions in the Nastran FE modal. This allowed easier correlation between experimental and numerical model solutions as the captured fiducials were output as a cloud of points of interest (POI) consistently between tests. An example cloud of POI is seen in Figure 65.

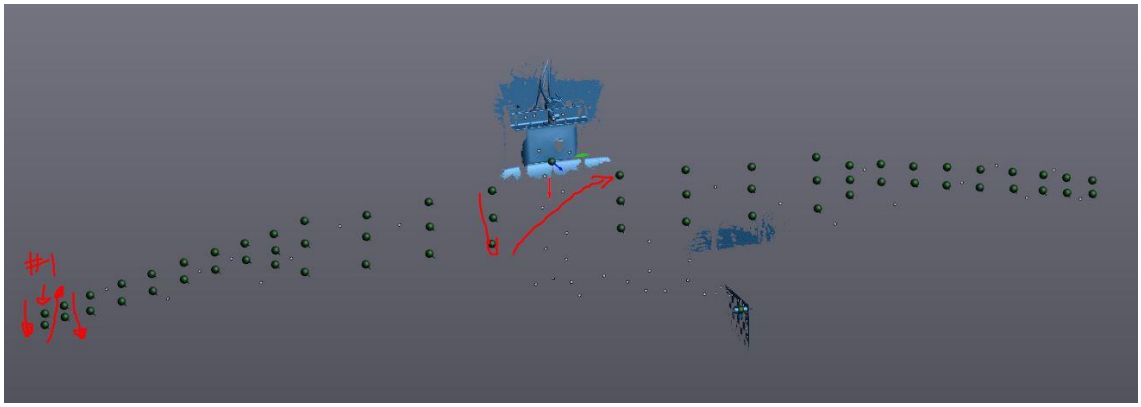

Figure 65: Point cloud of points of interest (POI) from 3D scanned fiducials. Note in centre of figure surface scan of saddle used to establish coordinate system datum at centre of wing leading edge.

4.1.1.3 Flip Load Case

Operationally, the wing of the RPA was removed for transport to and from the flight testing range. This required that the harness from the wing to the fuselage be re-assembled in the field every trip. Each time this was done the strain calibration for the strain gauges needed to be re-done. This resulted in a new set of bias which was compensated for by tarring measurements to zero. The procedure for this in the field was to place the vehicle on a level surface protected from wind. Note that due to the elasticity of the flexible spar, the wings drooped down significantly causing a bias in strain tarring process.

Figure 66: Strain compensation measurement to estimate wing droop following system tarring.

The bias in strain measurement from no deformation to the tarring position sitting on the ground was compensated with a bias compensation vector. This compensation was calculated in the shop by taking the fully configured RPA with the fuselage supported on a table upright, tarring the FDR strain measurements, and taking a 1 second log. Next the vehicle was carefully inverted, as seen in Figure 70, supported again by the fuselage and another log file was recorded. The mean of the time series for each log file captured was taken, then the difference between the two strain vectors was calculated and divided by two. The resulting strain vector was used to compensate the strain measurements taken for flight testing to get the absolute deformation of the wing in flight.

4.2 Ground Vibration Testing

Ground vibration testing of the aircraft was conducted to characterize the dynamic properties of the final flexible wing with instrumentation. This information was used for several aspects of the overall ASE project. In context of the SPA method for deformation measurements, GVT measurements were used to validate and update the FE numerical model used to generate all the mode strain and displacement shapes.

4.2.1 Impact Testing

Although both impact hammer and shaker methods were tested for exciting the structure. It was found that Impact testing was able to impart enough energy to excite a semi-wing span evenly, thus a single shaker input was used to excite the out-of-plane and torsion modes. Impact testing sufficiently excited the modes in-plane. Results from comparison between these methods is discussed in greater detail in another master thesis by Nuno Mocho [68].

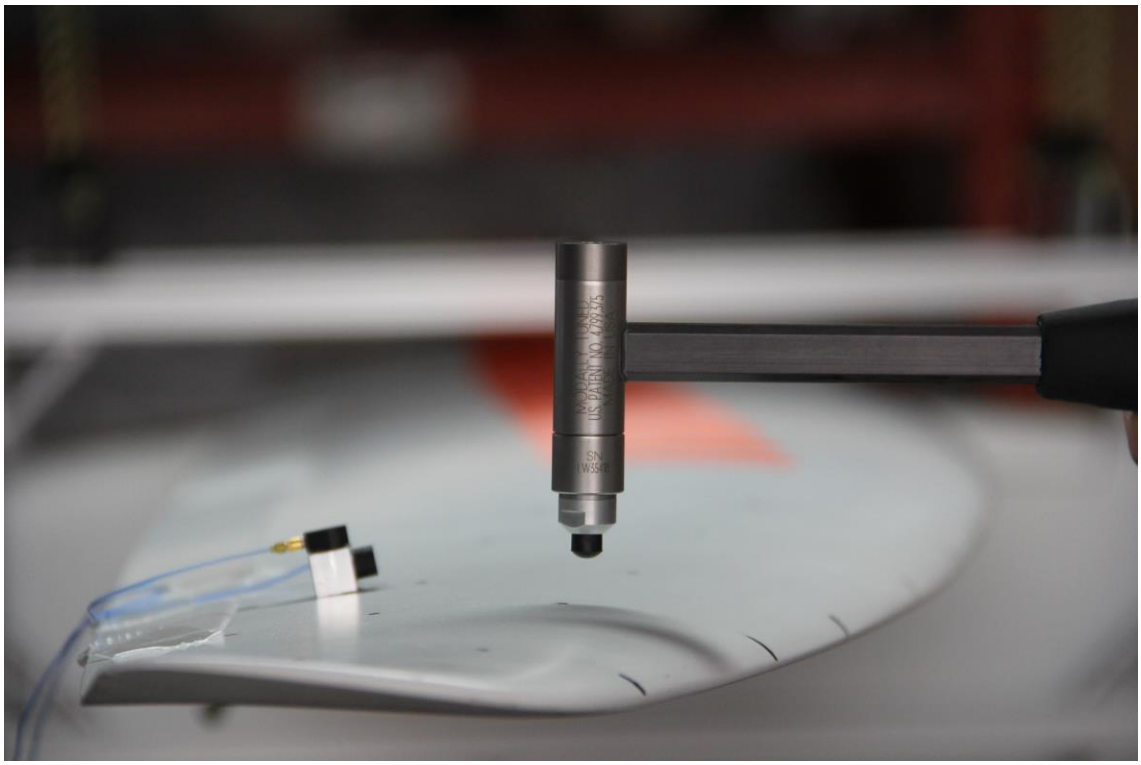

Figure 67: Impact hammer used, and fDOF location for accelerometers. Note use of 3 single axis accelerometers glued to aluminium cube attached with petrowax to structure. Black tip on modal hammer used as input for testing on QT1.2 pseudo-rigid baseline wings.

For Impact tests, a roving PCB model 086C03 hammer with the softest tip (red rubber) was used. The 3fDOF accelerometer was composed of three PCB 352A24 micro

accelerometers. Acquisition was accomplished using NI 9234 acquisition cards. No windowing was applied to the data prior to estimating the FRF as signal was pre-sampled prior to excitation and structural damping allowed signal to decay sufficiently during acquisition time.

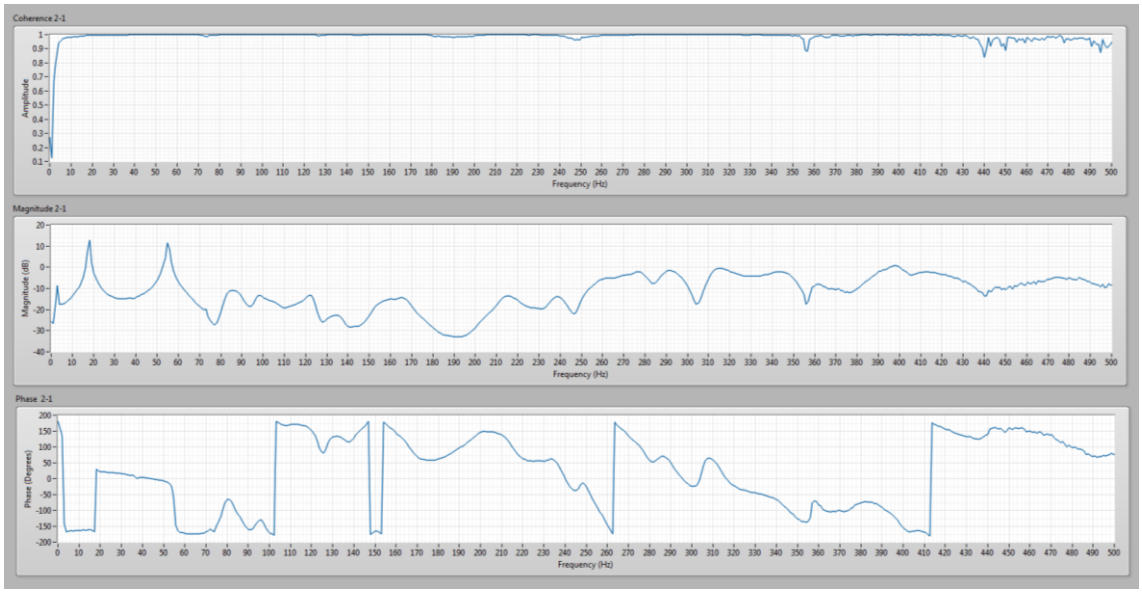

Figure 68: Averaged FRF measurement using software developed using NI Labview. Note poor correlation below 2Hz. The high elasticity of the structure made low frequency measurements around the first flapping mode challenging.

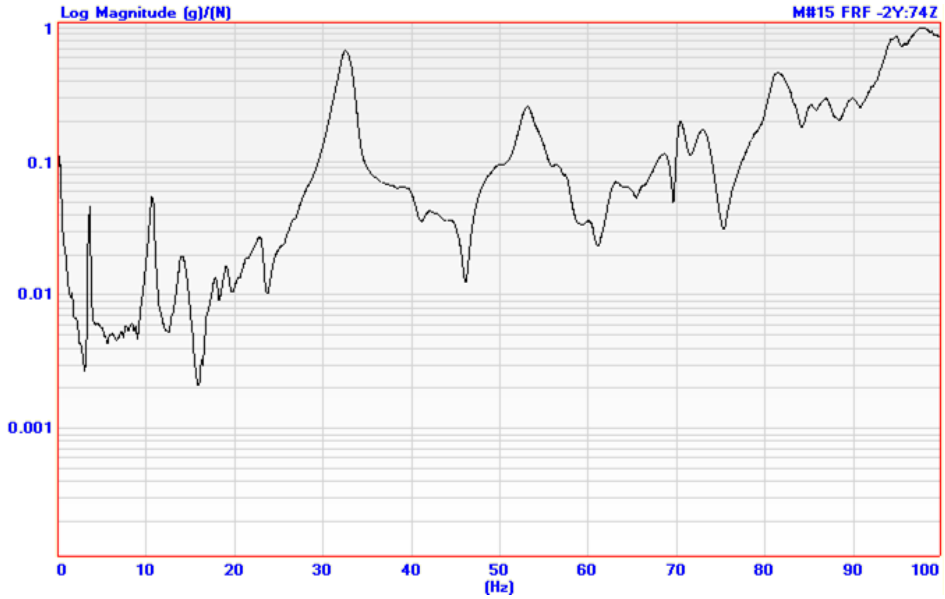

Figure 69: Log magnitude plot of FRF captured from impact test of wing. Note peaks alluding to presence of resonant modes. First out of plane elastic mode is roughly 3Hz.

4.2.2 Boundary Condition

The boundary condition used was a fixed condition were a pseudo-rigid connection between the wing saddle and the test stand was established, as seen in Figure 70. When the aircraft is fully assembled, the two wing halves join together and attach to the wing saddle, to form the wing assembly. This wing saddle is then bolted to the fuselage, and this connection is assumed to be pseudo rigid.

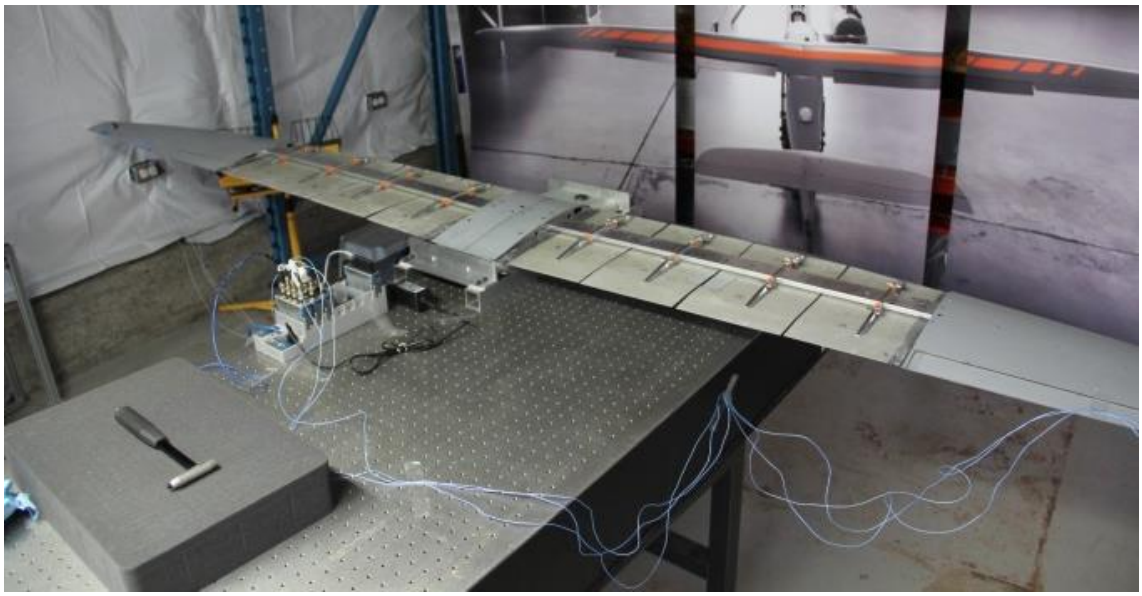

Figure 70: GVT of the cantilever wing for modal characterization using a fixed boundary condition at the wing saddle structure. Note use of 3 single axis accelerometers as fDOF near wing tips.

A rigid aluminum fixture was designed to emulate the portion of the fuselage that the wing saddle bolts on to, and this fixture was bolted to the test stand. The wing saddle was then attached to the fixture. This connection was assumed to be rigid in comparison to the flexibility of the wings. The fixture was bolted to an optical table with vibration damping, to help isolate the test equipment from external vibrations.

4.2.3 Pretest and Candidate Transducer Locations

Prior to testing, appropriate sensor locations were identified. To enable easier correlation between the experimental data and numerical models candidate sensor locations were kept roughly along the profile of the NASTRAN beam model. This included elastic and rigid bodies. Note that at this point some additional rigid body spars were added to allow sensor placements away from the torsional modes node.

As is generally custom with impact testing, the input DOF from the hammer would be roving, and the output accelerometer would be the fDOF. This makes sense as the input

does not require fixturing to the structure, and mass loading from the attached fDOF will be consistent for all captured FRFs.

Focusing on the first 5 elastic modes numerically estimated in the NASTRAN FE model, the normalized modal displacements were compared against each other. A location away from nodes of modes of interest was selected. Note the first 3 out-of-plane, 1st in-plane, and 1st torsional modes (z, x, and q axes) were specifically of interest. Near the wing tip (over top the NASTRAN model nodes 92 on the port wing, and 74 on the starboard wing) was selected. The input DOFs were a selection of more than 60 inputs spread along the rigid composite wing section and the flexible aluminum spar section. This distribution was confirmed using a modal pretest tool inside the FEMTools software suite. In the tool a region of interest is selected for modal testing, a number of measurement DOFs is selected and it determines the optimal location as seen in Figure 71.

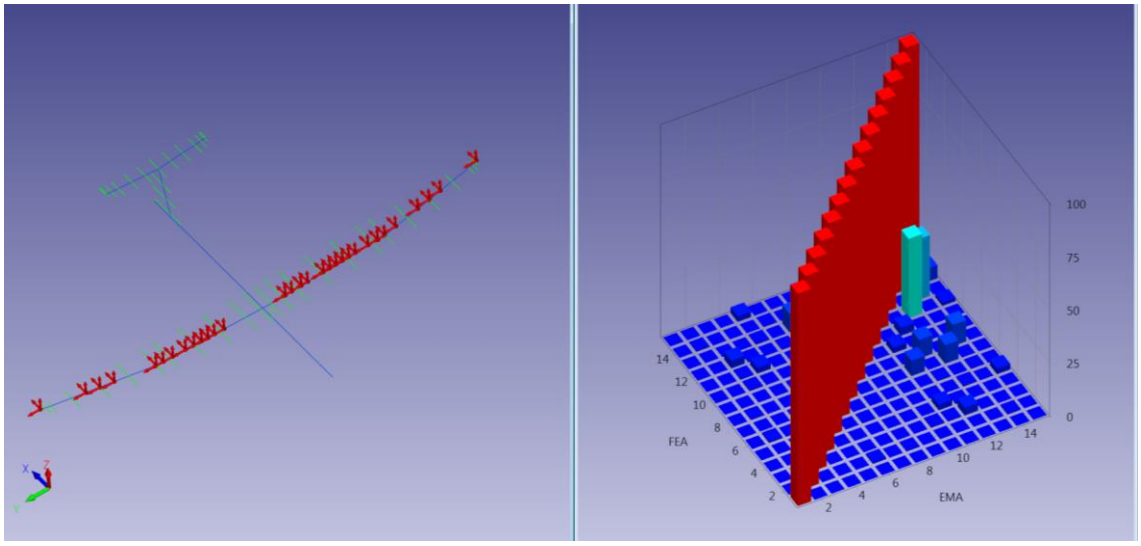

Figure 71: LEFT) NASTRAN FE model with candidate finite number of simulated 3DOF sensors distributed along wing using FEMTools. RIGHT) MAC comparison between first 15 elastic mode shapes directly from NASTRAN solver and first 15 mode shapes reconstructed from candidate sensor locations.

4.2.4 Parameter Extraction

After acquisition of the raw data and FRF calculation, the FRFs for all the measurement DOFs were curve fit using MeScope, by Vibrant Technology. This was done to isolate modes within the FRFs providing,

- Resonant Mode Frequencies
- Mode damping
- Mode Shapes

The results have been compiled into a UFF58 format for comparison against the FEM modal using a FE database and optimisation tool named FEMtools.

4.2.5 RESULTS

Here are series of experimental results are tabulated. These results are the modal peak frequencies for the wing with and without the SPA instrumentation installed (instrumented and uninstrumented). Note that with instrumentation modal frequencies drop in frequency, which is expected given the additional distributed mass. Frequencies shift down roughly 10% depending on the mode. Further correlation and analysis against the FE model is discussed in section 4.3.3.

Table 9: Results from the GVT cantilevered wing test are summarized by modal.

Fixed Cantilever					
Mode #		Instrumented	% Shift	Unsintrumented	% Shift
1	2.8	2.89	2.1	3.05	7.8
2	11.1	12.9	15.8	12.5	12.2
3	15.9	15	5.6	X	X
4	X	17.8	X	18.8	X
5	X	22.7	X	X	X
6	X	37.4	X	39.6	X
7	54.1	55.9	3.2	59.2	9.3
8	64.1	X	X	73.6	14.8
9	91.7	84.1	8.3	X	X
10	112.8	X	X	X	X
11	166.2	X	X	X	X

4.3 FE Model Updating

The FE model was updated and correlated against the static load and ground vibration tests. A mixed strategy of updating component wise was followed. The strategy followed is summarized in Figure 72.

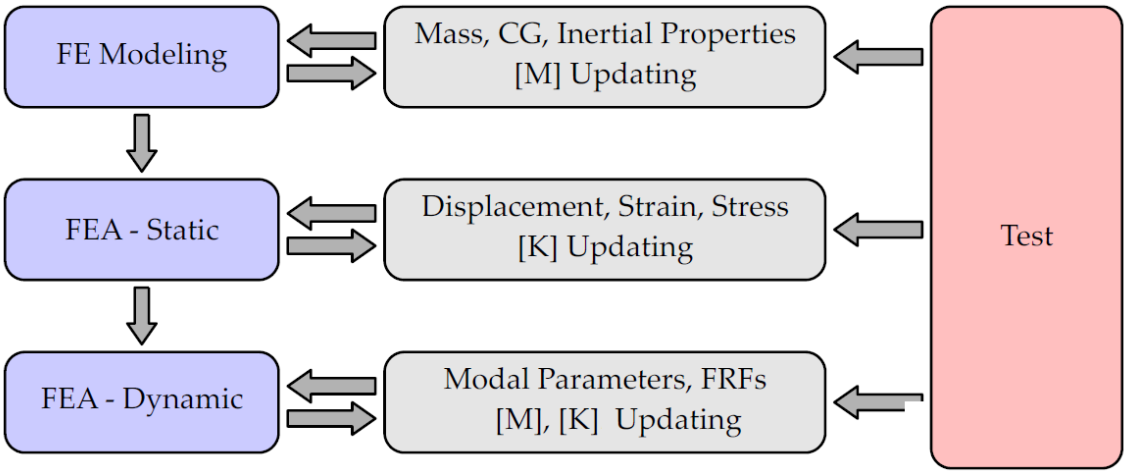

Figure 72: Update strategy applied to FE model.

First the FE model's mass properties were updated from measurements made of the aircraft as built. Next the model's stiffness was updated using static load tests in logical key areas, global groups, and some boundaries conditions to better replicate the test. Finally, Mass/Inertia, and Stiffness were updated using GVT tests.

4.3.1 Mass and Inertia Measurements

Individual components and assemblies from the as built wing were all measured and compared to the FEM model. This procedure was used to verify the resulting mass of the different components and used to ensure the FE model approximation matched the test article. It is preferable to update model parameters directly without need for optimization or tuning when possible.

Figure 73: Winglet being weighed.

Masses for non composite components were checked in the geometry sub-tree in ANSYS MECHANICAL. The composite parts weights were verified individually in the ACP application in the sensor sub-tree.

Figure 74: Mass of rib 4 and lower panel.

Table 10: Final model mass after update/optimization.

FE (KG)	Test(KG)	Difference (%)
2.062	1.970	-4.7

The final mass of the FEM model was close to that of the as built wing with an error less than 5%. Some alteration was made to the geometry with the addition of a mass to represent the aileron surface servo, and the inertia of the point masses representing ribs1-4 was estimated. The inertia of the panels was estimated by taking the Solidworks sub-assembly of the panels and ribs, overriding the mass with the measured value and using the CAD model to estimate the inertia. Some assemblies, such as the lower composite covers with rib seen in Figure 74, will end up with slightly higher inertias as the mass distribution should be more focused around the rib. This parameter will be allowed to change in the dynamic model updates. The upper panel covers will not be included for the updating process, however they should add little error due to their small mass, and consistent material make-up permits reasonable inertia estimating.

4.3.2 Static Load Updating

The static updates where done using a commercial software made by Dynamic Design Solutions by the name of FEMtools [69]. FEMtools comprises of a database of tools designed to parse/interface with FE solvers, as well as load experimental data and correlate them with FE models. It also has a multi variable multi output optimisation module appropriate for making changes to FE models for fitting with experiments. It is primarily marketed as a tool to update FE models with respect to experimental modal data.

The FE model was loaded into FEMtools in cdb format. Note that FEMtools version 3.8 did not natively support static updating using the ANSYS solver (for reference support has been added in version 4, however, the author has not verified its use). FEMtools provided guidance [70] to develop a script, see Appendix I, to apply the loads for the correlation with the experimental deflections. Loads were applied at the nodes described in 3.3.4 Boundary Conditions.

The experimental load data was loaded into FEMtools. Static load results were written into the UFF-file or UFF58 format. This was accomplished manually for 4 points along the spar using the single point load static tests. A tool, node-pairing, was used to link the un-deformed FEM model with the un-deformed measurement points. A useful and recommended tool.

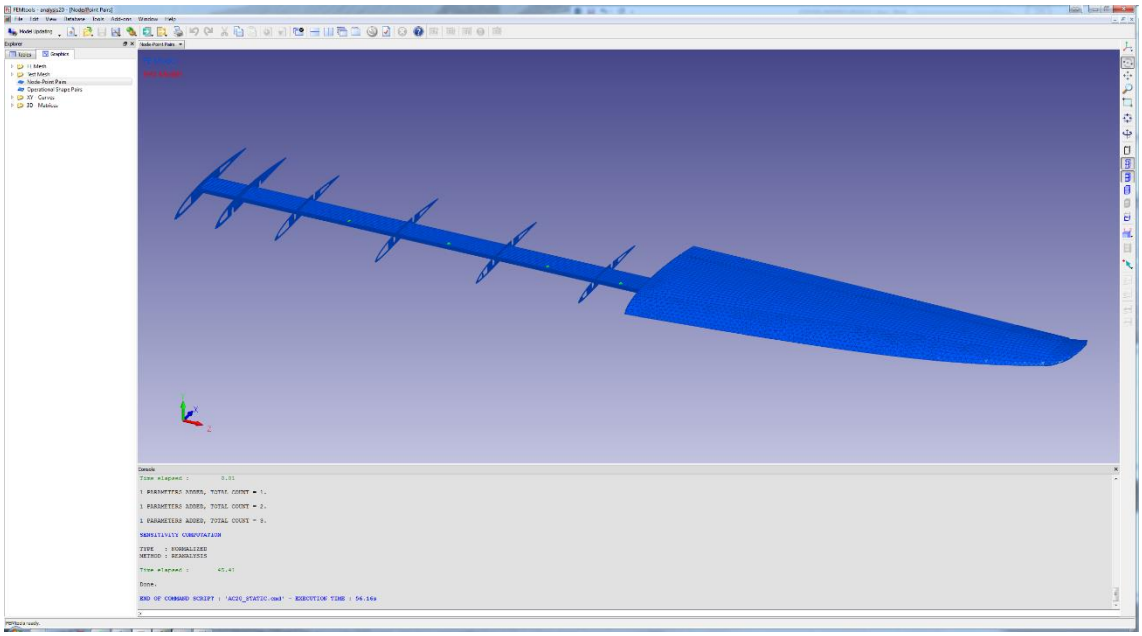

Figure 75: FEM and experimental node pairing.

Response variables were set to be nodes displacements paired with the experimental data. After responses, parameters for changing were set. The individual stiffness for the model named selections Root_Clamp_Inner, Root_Clamp_Outer, Spar, and Spar_Root were selected. A sensitivity analysis confirms that the Spar and Spar_Root parameters cause the greatest change in the responses. Note that the parameters were constrained to a maximum change of no greater than ±10% at the end of the optimisation.

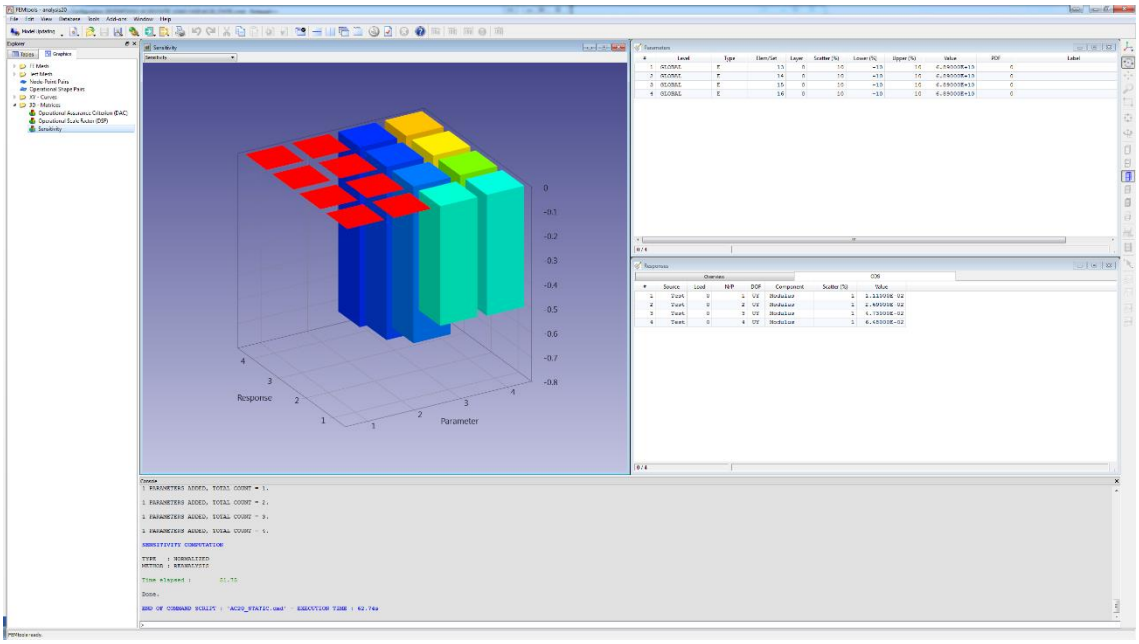

Figure 76: Static sensitivity analysis results.

In the optimizer, the absolute and rate of convergence criteria were set and the model was configured to use reanalysis, meaning the sensitivity matrix was recomputed each iteration with perturbed values as opposed to estimated using backward differences. This method is considered to be more accurate but not as fast [69].

The optimiser converged in 5 iterations, and improved the results fit to within ~5%. These results are summarized in Table 11 and Table 12.

Table 11: Parameters changed for static matching.

#	Level	Type	Elem/Set	Old	Actual	Difference (%)
1	GLOBAL	E	13 (ROOT_INNER)	6.89E+10	6.89E+10	3.83E-09
2	GLOBAL	E	14(ROOT_OUTER)	6.89E+10	6.88E+10	-1.88E-01
3	GLOBAL	E	15 (SPAR)	6.89E+10	6.50E+10	-5.66E+00
4	GLOBAL	E	16(ROOT_SPAR)	6.89E+10	6.20E+10	-1.00E+01

Table 12: Response improvements for static matching.

#	Fea	Test	Difference (%)
1	1.00E-02	1.11E-02	-9.73E+00
2	2.55E-02	2.69E-02	-5.34E+00
3	4.54E-02	4.73E-02	-4.11E+00
4	6.16E-02	6.48E-02	-5.01E+00

For reference, scripting used for the static updates is in Appendix I.

4.3.3 Dynamic Updating

Dynamic optimization was completed similarly to that of the static data with the exception that there were 4 mode shape and peak frequencies which were matched to the model. Most of the steps were the same with a couple variations. One difference was the FEM and experimental shapes had to be paired. This can be done manually, however, because the shapes had unique MAC confidence greater than 90% it was straightforward to match them correctly automatically.

The model configuration used for updating has the hatch covers suppressed. These will be enabled for the final dynamic shapes used.

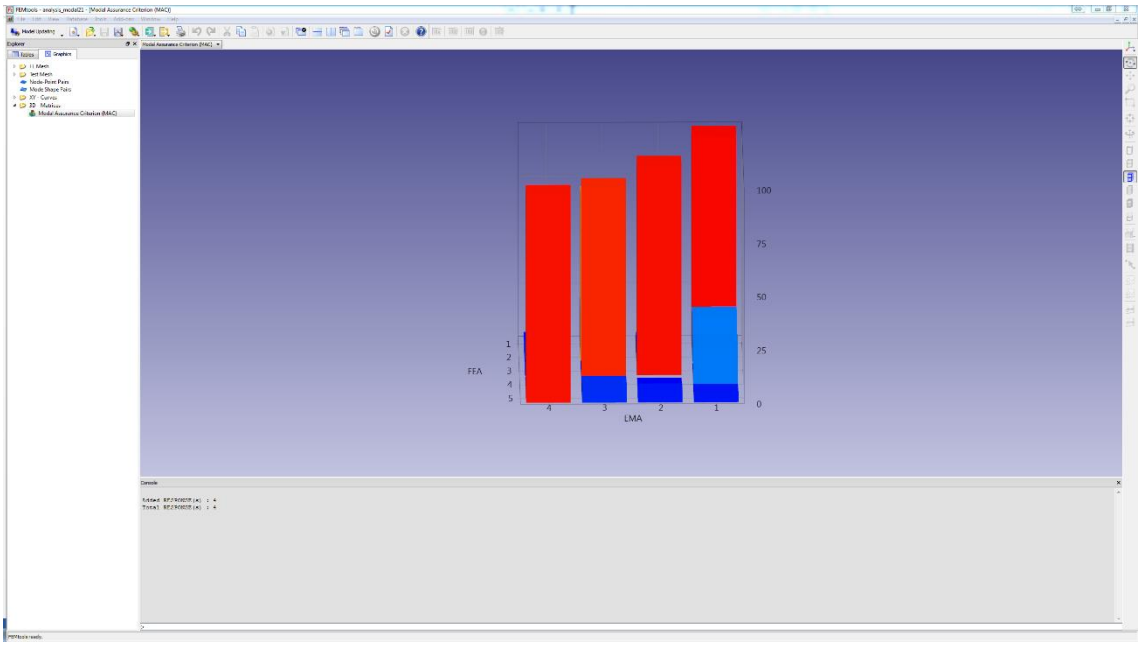

Figure 77: Initial MAC results between FEM and experimental.

The experimental modal data, which was exported from ME'Scope in UFF-file format, required some coordinate transforms to be aligned with the ansys FEM model. FEMtools has some straightforward and easy tools to help reposition the data. This is a manual task, however, once done may be easily scripted for ease in the future, see Appendix 5. After the transformation the applications automatic node-pairing worked flawlessly.

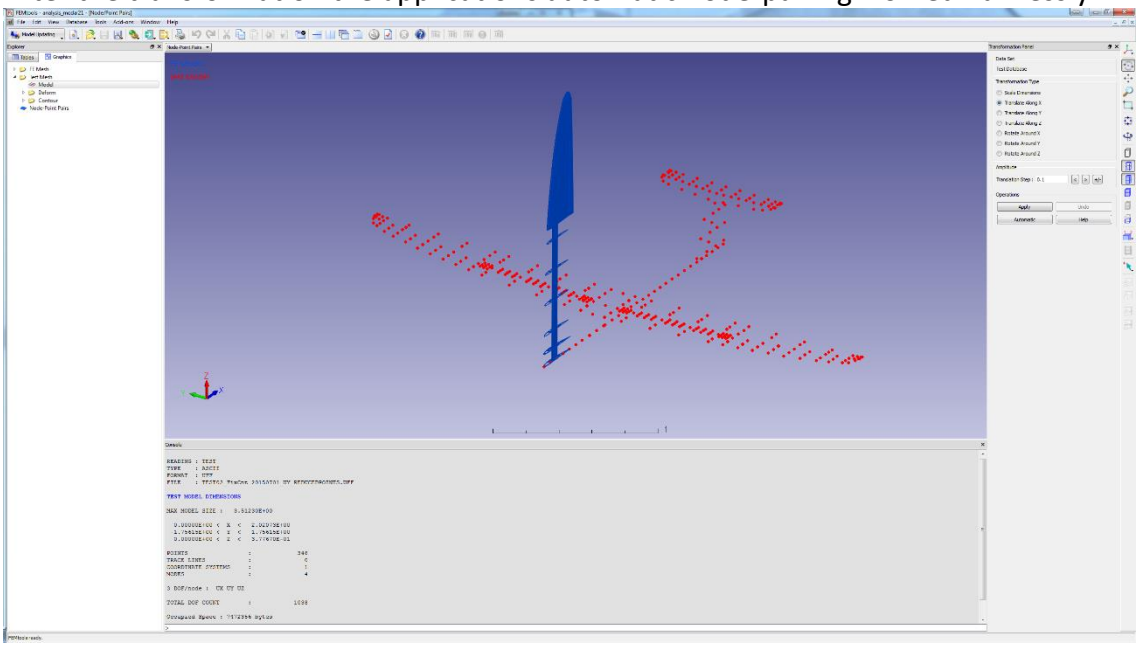

Figure 78: Coordinate transformation of experimental data relative to the FEM prior to node-pairing.

Unlike in the static optimisation, the rib 1-4 inertias Ixx, Iyy, and Izz were selected as parameters to update. The parameters were allowed to change up to ±200%. The responses for analysis were the modal frequencies. The optimiser was configured as before in the static updates.

After the first iteration the peak frequencies were all matching within ~2% with no more than ~5% change in masses and ~20% change in inertia.

Mode shapes were added to the responses with constraints of ±10% change in stiffness. Root_spar stiffness was added to parameters and the inertias were replaced with masses of ribs1-4. Convergence was quick and peak frequencies all matched to within < 1%. The MAC criterion indicated that out-of-plane shapes 1-3 matched to ~ 98% and the torsional mode matched to 94%. The final change in stiffness was rejected in favour of maintaining better static test fits.

Table 13: Final FE model parameter changes.

#	Level	Type	Elem/Set	Old	Actual	Difference (%)
1	GLOBAL	E	18	6.20E+10	6.32E+10	2.00E+00
2	GLOBAL	MG	43	3.00E-02	2.62E-02	-1.26E+01
3	GLOBAL	MG	44	1.30E-01	1.33E-01	2.05E+00
4	GLOBAL	MG	45	1.17E-01	1.27E-01	8.19E+00
5	GLOBAL	MG	46	1.45E-01	1.39E-01	-3.88E+00
6	GLOBAL	MG	47	1.09E-01	8.76E-02	-1.96E+01

Table 14: Final response fit.

#	FE	Test	Difference (%)
1	3.03E+00	3.05E+00	-7.45E-01
2	1.89E+01	1.88E+01	4.21E-01
3	3.93E+01	3.96E+01	-7.24E-01
4	5.92E+01	5.92E+01	-7.11E-02
5	9.89E+01	1.00E+02	-1.11E+00
6	9.77E+01	1.00E+02	-2.27E+00
7	9.41E+01	1.00E+02	-5.90E+00
8	9.71E+01	1.00E+02	-2.95E+00

For reference, scripting used for the dynamic updates is in Appendix J.

4.4 Flight Testing

A series of flight tests were completed with the fully instrumented flexible ASE demonstrator. A total of seven flights with all instrumentation installed and recording were completed with data sets.

Figure 79: Flexible ASE QT1.3 flying over Saanich. Note wing shape while at rest on ground is traced in green overlay.

For flight testing the strains were acquired starting shortly prior to take-off until shortly after touchdown. This data was collected with all the other flight test data for the ASE flexible flight tests. Note that prior to each flight the vehicle was placed on a flat table and the flight data recorder was allowed 10 minutes to run and reach steady state internal temperatures as a best practice, although no appreciable drift was observed. After warmup, the aircraft was verified to be sitting as steady state as possible and the strain measurements were tared to zero. Prior to launch, data collection for all sensors was started. Logging of data was terminated after landing and coming to full rest. Prior to downloading and storing data, system was assessed to verify strain gauges were all functioning properly.

Figure 80: ASE QT1.3 undergoing pre flight assembly checklist. Individual strain gauge harness' are being installed.

Figure 81: ASE QT1.3 on final approach to land.

Chapter 5 – Deformation Measurement Results

5.1 Ground Test Results

In this section the results for deformation measurement by SPA are analyzed against the distributed load static tests. The single point load tests used to update the FE model were kept independent from assessment of deformation measurement. Comparisons were made after having updated the FE model allowing for generation of updated strain and displacement patterns. Note that errors were calculated with equation (21) from section 3.6. For this section, reference deformation (displacement or twist) is in the context of the optical CMM, whereas previously it referred to FE model static simulation deformation.

Wing displacements generally agree well against the reference deformation measurements. Distributed out-of-plane load cases perform best. Reasons for this include focus on strain gauges for measuring this type of motion, and out-of-plane/flap mode shapes with considered boundary conditions are good approximations to deformations seen in tests thus requiring fewer patterns to create a good approximation. The deformed aircraft for static distributed load test 02 is presented in Figure 82. The deformed aircraft results for all tests are available in Appendix K.

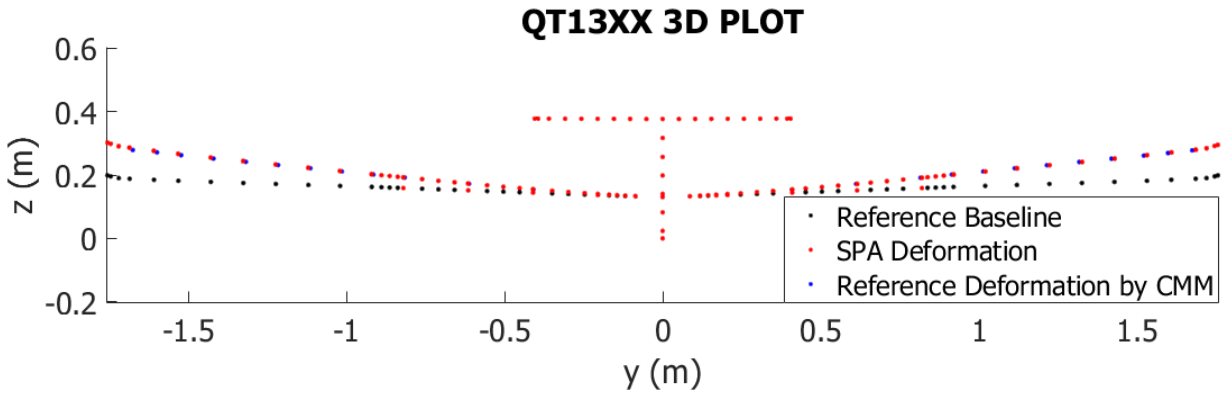

Figure 82: Distributed Load test 02 deformation plot. This case is an out-of-plane/flap load case approximating roughly 0.9g pull-up.

The deformation estimation by SPA demonstrated its lowest errors along the instrumented flexible aluminum spar component of the wings. For both wings, in most cases, error along this portion of the wing is less than 2mm. Error increases in the extrapolated rigid wing sections. There is a trend where the right semi-span of the wing appears to perform better than the left semi-span in particular in extrapolated wing tip position as seen in Table 15. Distributed load test error plots for all tests are presented in Appendix L.

Table 15: Summary of errors measured flexible spar tip and wing tip for left and right wings under different loading conditions.

		Left Wing				Right Wing			
		Error (mm)		Error (%)		Error (mm)		Error (%)	
#	DP Load (g)	Span 930mm	Span 1750mm	Span 930mm	Span 1750mm	Span 930mm	Span 1750mm	Span 930mm	Span 1750mm
0	0	0.0	0.0	0.0	0.0	0.0	0.0	0.0	0.0
1	0.7	-0.4	-2.6	2.6	7.7	0.6	1.2	5.0	3.3
2	0.9	-1.0	-7.0	2.6	7.7	-0.2	-1.7	0.7	2.1
3	1.2	-1.8	-11.0	3.0	7.5	-0.1	-4.7	0.4	3.4
4	1.4	-2.4	-15.7	2.7	7.7	-0.9	-8.8	1.3	4.5
5*	1.7	-	-	-	-	-	-	-	-
6	N/A	3.5	7.5	82.0	82.6	2.8	3.7	54.5	40.9
7	N/A	2.0	-1.7	8.0	2.0	1.9	-2.6	5.0	3.7
8	N/A	2.0	1.6	12.0	4.2	1.1	-1.6	7.0	4.5
9	N/A	0.7	-6.9	2.2	6.7	1.3	-4.9	4.0	4.7

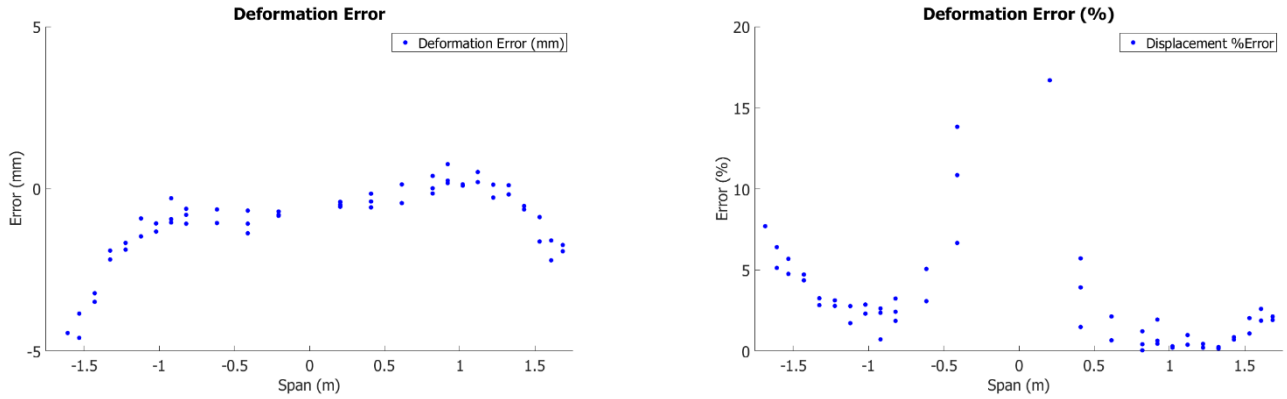

Figure 83: Distributed Load test 02 out-of-plane deformation error for both wing halves. These plots focus on the out-of-plane/flap displacement in the wing. Note good agreement for flexible spar. Error increases with almost linear slope along extrapolated rigid wing portion suggesting joint stiffness update required.

Where the instrumented flexible spar ends and transitions to the rigid wing portion the slope in the error changes. This is shown in Figure 83. This behaviour suggests that the stiffness of the joint between the flexible and rigid components of the wing require further tuning. The single point load static tests and model updating emphasized the flexible wing and its attachment to the aircraft at the saddle. This behaviour is consistent and can likely be improved by revisiting the FE model and focusing on this joint stiffness.

There is a limited amount of twist data generated from these tests. The amount of twist observed through the tests is generally very small, almost within the noise floor of the optical CMM (less than 0.2degrees). Distributed load cases 7 and 8 introduce a combined out-of-plane/flap and torsion load. These tests, although artificial (ie not expected in flight), offer insight in the quality of the twist estimated by SPA. Note twist angle was measured by taking a forward and trailing displacement measurement, the reference distance between them and estimating an angle. Wing twist for test 7 is presented in Figure 84 and the error between reference measurements are plotted in Figure 85. Wing twist and twist error is presented in Appendix M and Appendix N respectively.

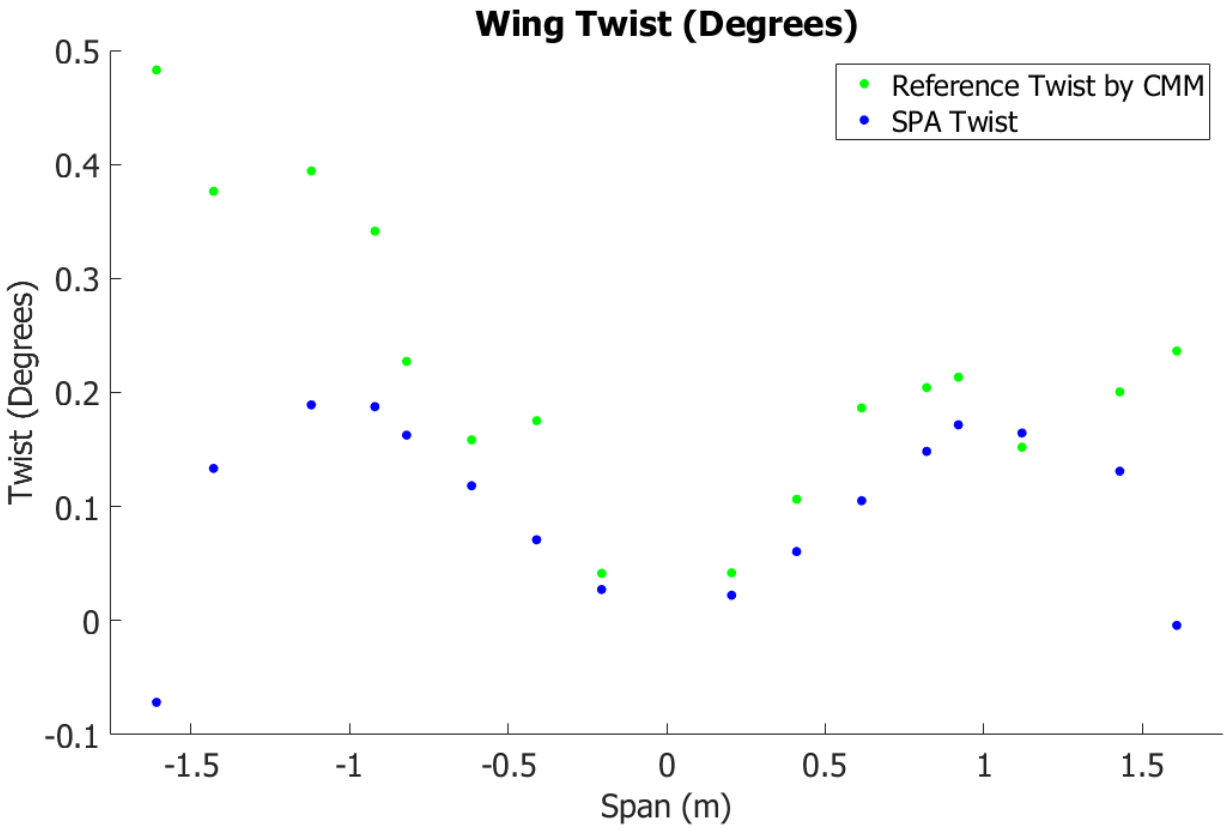

Figure 84: Distributed load test 07 experimental wing twist. Along the instrumented flexible spar, 0 to 0.9 span, the twisting trend matches.

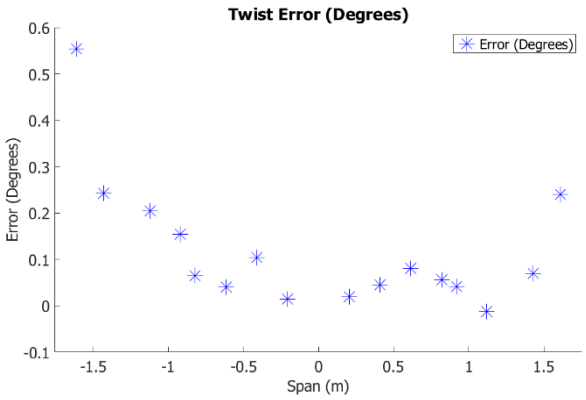

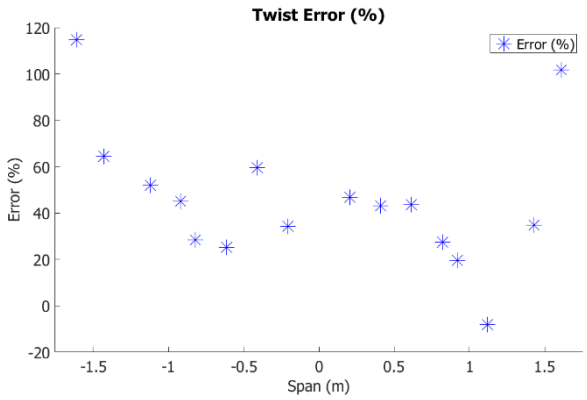

Figure 85: Distributed Load test 07 experimental wing twist errors. This test is a combined out-of-plane/flap and torsion loading case (this artificial condition is not expected in flight). Errors, particularly represented in percent need to be carefully considered due to small angles and noisy reference measurement. The largest twist angles observed are in test 7, followed by test 8. Even the largest twists are less than 0.5 degrees at the wing tip. Twist from the CMM is noisy, but demonstrates trend and order of magnitudes estimated by the SPA method. The instrumented flexible spar portion of the wing (between 0m and 0.9m spanwise) shows good agreement. There is some issue observed in extrapolation of the wing tip twist. Although the twist error, particularly in percentage appear large, the twist angles overall are small, and the reference is relatively noisy and do not present much meaning in this context.

Difference between the experimental measured strain and the least squares modal fit is more apparent as seen in Figure 86 for distributed test 2, and for all distributed tests in Appendix O.

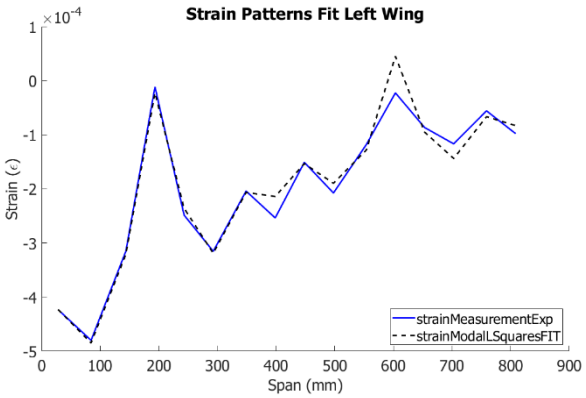

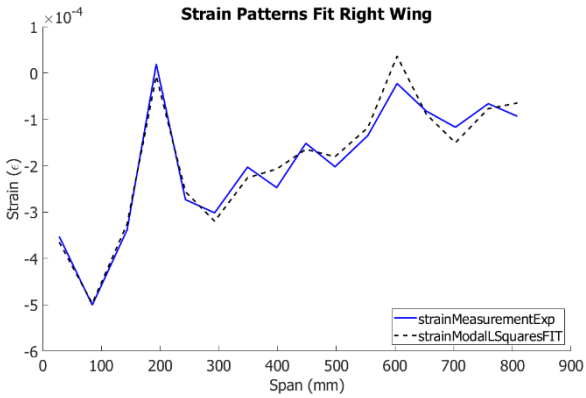

Figure 86: Distributed Load test 02 strain modal fits

Discrepancies in the strain modal responses are likely resultant from a number of factors. Some of these contributions could be

1. Strain Gauge orientation and spatial positioning
2. Strain Gauge discreet measurement larger than modelled
3. Non-linearity's from large deflections
4. Not enough or ill suited mode shapes to fit

Although these conditions contribute to errors, adequate out-of-plane/flap measurement performance is demonstrated for the ASE application. However, opportunity exists for further refinement. Improvements could be potentially accomplished by tuning the individual strain gauge models in the FE model use to derive the mode shapes. Tuning of spatial, and bridge orientation could improve the fit. Further, blending multiple strain measurements in the FE model could better replicate the strain field measured.

Non-linearity from the large deflections could be approached by generating mode shapes at a trim point closer to the expected aircraft flight at steady state. Although this shifts the problem, it would reduce measurement error around the shape most readily seen in flight. Alternatively, the modal shapes could be replaced with shapes expected to be seen in flight. This could be done from simulated flight loads. The FE model could be used to generate the strain and displacement patterns required.

5.2 Flight Testing

Flight testing results were collected however analysis in the scope of this thesis is limited to initial observations. Review of telemetry logs indicate that deformation (both out-of-plane deflection and twist) are within the expected magnitudes observed in the ASWING model. Additionally, qualitative comparison between video captured on the tail of the aircraft using an action camera demonstrates visual matching between SPA and video footage. A still from such a comparison is presented in Figure 87. In this figure the wing appears to have a greater curvature due to camera lens distortion. For future work a more in-depth analysis matching flight test data and ground test data is recommended.

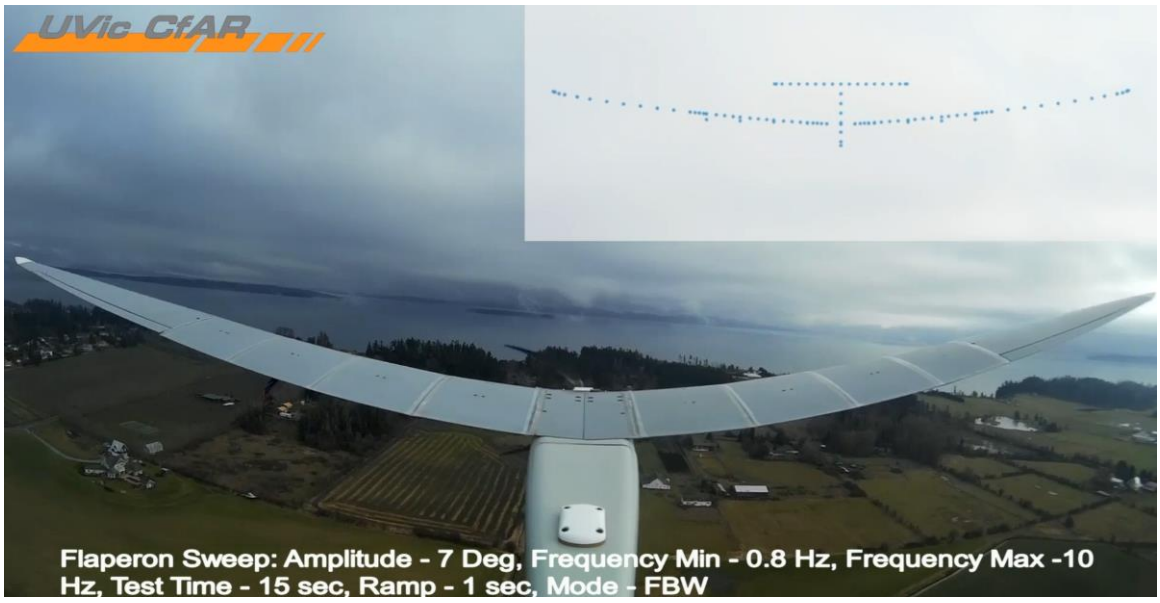

Figure 87: Still taken from a video of a flaperon surfaces chirp conducted as a test point in a flight test in Saanichton British Columbia. In the upper right corner is the wing out-of-plane deformation calculated using the deformation by SPA method.

Chapter 6 - Conclusions and Future Work

The aerospace industry is searching for improved capabilities in efficiency, range, and comfort. Enhanced aerodynamics is a means of furthering this goal, for instance, by increased wing aspect ratio. However, with increases in aspect ratio come new design challenges resulting from aero-elastic and aero-servo-elastic phenomena. Although new computational tools have been suggested, there is a need for experimental data for validation. UVic CfAR set out to design a 20kg ASE demonstrator RPA to explore coupling between aeroelastic modes including coupling between the short period aerodynamic mode and the first out-of-plane elastic mode of the wing. Onboard instrumentation was required to be able to measure the relevant wing deformation in flight. This thesis discusses this implementation and its performance as tested on the ground.

6.1 Accomplishments

A method for measuring the shape of an RPA wing in-flight was required as one of a number of ASE flight test measurements. A number of methods for measuring the wing deformation were explored including different methods of photogrammetry and strain based shape estimation. A strain based technique was selected for integration into the ASE aircraft due to several reasons including its reliability regardless of outdoor lighting, relatively light weight processing requirements for real time applications, and suitable sampling bandwidth. The selected method, sometimes referred to as strain pattern analysis (SPA), utilizes linear combinations of reference patterns or shapes. In this project, modal shapes were used to identify wing deformation.

First a general method for workflow is discussed. The concept of building an FE structural model to derive numerical solutions to use as the reference modal patterns, define sensor locations, and select appropriate mode shapes is discussed on its application to a small RPA. Although this method is not new, to the author's knowledge, it is the first practical application to a reduced scale RPA demonstrator.

Although briefly commented on, the design, and integration of a flight data recorder capable of making all the relevant strain measurements within the size and weight constraints of the RPA is mentioned, as this was challenging. The final system was capable of measuring 32 strain channels (16 strain gauge bridges per wing) simultaneously at 2KHz with time synchronization relative to all other ASE dynamics measurements. Data was successfully recorded for all flexible ASE flights.

The strain gauge spatial installation and orientation was based on a method described previously for use on helicopter rotor blades tested at ONERA. This method of alternating bridges orientation was successful in reducing ambiguity between strain patterns from out-of-plane, in-plane, and torsion mode shapes.

The deformation measurement by SPA method was verified using simulated load cases from the FE model used to generate the numerical strain and displacement mode shapes. This procedure was completed for a variety of load cases.

Experimental testing of the system was completed which included a series of static load tests for FE model validation as well as deformation measurement by SPA method validation. A series of GVT tests were complete for further FE model validation/updating. FE model updating resulted in several tuned parameters with specific focus around the instrumented flexible aluminum spar section of the wing. This later resulted in good performance of the deformation measurements by SPA.

The deformation measurement system was validated against a series of distributed static load tests on the ground. Distributed load cases along the wing demonstrated good out-of-plane measurement performance. A case where only load is applied near the root of the wing resulted in the largest error in part as the mode shapes generated are less suited to approximate the resulting shape. In general errors in out-of-plane displacement at the end of the flexible wing portion can be expected to be less than 5%. The displacement at the tip of the wing can be as great as 11% for the left wing whereas the right wing is 4.7%. This suggest an asymmetry between the left and right wings requiring specifically tuned FE models for each to achieve best results. Twist angles presented in tests were relatively small for accurate comparison against the reference measurement which was quite noisy. Generally, the deformation measurement by SPA technique followed the same twist behaviours as the reference. A twist case, unlikely to be seen in flight, provided some insight into twist measurement robustness.

6.2 Future Work

The work completed here presents another step forward. Applying the deformation by SPA method to a small RPAS in flight testing enabled further study of ASE phenomena. There are many opportunities for further exploration in this topic. The author wishes to touch on several briefly here.

Room exists for improvement of the FE modal used to estimate the mode shapes. Initial focus was to ensure the instrumented flexible portion of the wing shape would have best performance. This did result in good performance, however, it can be seen that there are steady errors in the rigid outboard wing, likely attributable to error in stiffness between the flexible spar and the rigid wing. Additionally, there was apparent asymmetry between the left and right semi-wing spans suggesting a separately tuned FE model could improve the resulting wing deformation estimates for the other wing.

The wing was made to be relatively stiff in-plane, or torsion. As such, more focus was made measuring the out-of-plane deformation. Further validation of this method's ability to measure torsion and in-plane motion would be beneficial. Because boundary condition and pre-load of reference strain/displacement patterns are important in

minimizing estimation error it is suggested that rather than purely using mode shapes, the addition of shapes based on FE static load cases representative of test conditions be investigated.

Originally the deformation by SPA method was selected as a method which could be reliably computed in real-time with minimal disruption and latency within the envelope of a 25KG or less RPA. A real-time implementation was not completed and would be particularly interesting for use as feedback for flight control. Study of load alleviation techniques may benefit.

Another topic of study is the combination of this method with others to provide more robust, higher measurement bandwidth, and sensitivity. A method was recently published describing a deformation/shape estimation Kalman filter where the inputs are camera based photogrammetry and accelerometers [71]. This type of sensor fusion could be accomplished using the deformation by SPA and accelerometer data.

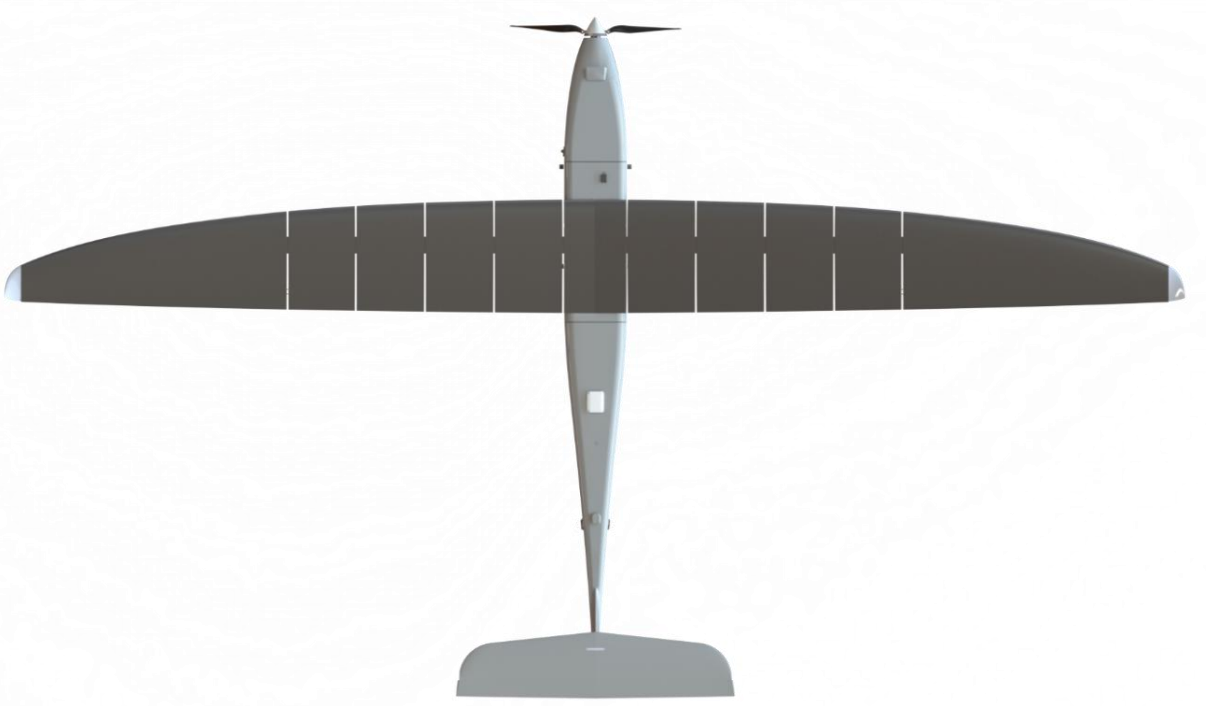

BIBLIOGRAPHY

[1] J. Matlock, S. Warwick, J. Richards, and A. Suleman, “PERFORMANCE EVALUATION OF A UAV HYBRID PROPULSION SYSTEM,” Victoria, 2017.

[2] J. T. Matlock, “Evaluation of Hybrid-Electric Propulsion Systems for Unmanned Aerial Vehicles,” University of Victoria, 2019.

[3] IATA, “IATA Forecast Predicts 8.2 billion Air Travelers in 2037,” 2018. [Online]. Available: https://www.iata.org/en/pressroom/pr/2018-10-24-02/.

[4] Federal Aviation Administration, “FAA Aerospace Forecast Fiscal Years 2019-2039,” 2019.

[5] ICAO, “Destination Green: Driving progress through action on aviation and the environment,” *ICAO J.*, vol. 68, no. 2, pp. 5–8, 2013.

[6] J. E. Green, “Civil aviation and the environmental challenge,” *Aeronaut. J.*, vol. 107, no. 1072, pp. 281–300, 2003.

[7] J. Penner, D. Griggs, D. Lister, D. Dokken, and M. McFarland, “Summary for policymakers: Aviation and the global atmosphere,” 1999.

[8] FAA, “ECONOMIC VALUES FOR FAA INVESTMENT AND REGULATORY DECISIONS, A GUIDE FINAL REPORT,” 2016.

[9] J. Reneaux, “Overview on drag reduction technologies for civil transport aircraft,” *ECCOMAS 2004 - Eur. Congr. Comput. Methods Appl. Sci. Eng.*, no. July, pp. 1–18, 2004.

[10] J. D. Anderson, *Fundamentals of Aerodynamics*, 6th ed. 2017.

[11] A. Abbas, J. de Vicente, and E. Valero, “Aerodynamic technologies to improve aircraft performance,” *Aerosp. Sci. Technol.*, vol. 28, no. 1, pp. 100–132, Jul. 2013.

[12] J. Richards, A. Suleman, R. Canfield, and M. Blair, “Design of a Scaled RPV for Investigation of Gust Response of Joined-Wing Sensorcraft,” in *50th AIAA/ASME/ASCE/AHS/ASC Structures, Structural Dynamics, and Materials Conference*, 2009.

[13] B. Dunbar and L. Gipson, “Down to Earth Future Aircraft | NASA.” [Online]. Available: https://www.nasa.gov/content/down-to-earth-future-aircraft-0. [Accessed: 17-Feb-2020].

[14] M. Bradley, “Boeing: How sweet the future of aviation,” *Boeing*. [Online]. Available: https://www.boeing.com/features/innovation-quarterly/aug2017/feature-technical-sugar.page. [Accessed: 17-Feb-2020].

[15] “NASA - Blended Wing Body Fact Sheet.” [Online]. Available:

https://www.nasa.gov/centers/langley/news/factsheets/FS-2003-11-81-LaRC.html. [Accessed: 17-Feb-2020].

[16] F. Afonso, J. Vale, É. Oliveira, F. Lau, and A. Suleman, “A review on non-linear aeroelasticity of high aspect-ratio wings,” *Progress in Aerospace Sciences*, vol. 89. 2017.

[17] T. E. Noll, M. E. Perez-Davis, S. D. Ishmael, G. C. Tiffany, and M. Gaier, “Investigation of the Helios Prototype Aircraft Mishap,” 2004.

[18] C. E. S. Cesnik, P. J. Senatore, W. Su, E. M. Atkins, and C. M. Shearer, “X-HALE: A Very Flexible Unmanned Aerial Vehicle for Nonlinear Aeroelastic Tests,” *AIAA*, vol. 50, no. 12, 2012.

[19] J. J. Ryan and J. T. Bosworth, “Current and Future Research in Active Control of Lightweight, Flexible Structures Using the X-56 Aircraft,” in *52nd Aerospace Sciences Meeting*, 2014.

[20] J. Richards, “An Experimental Investigation of a Joined Wing Aircraft Configuration Using Flexible , Reduced Scale Flight Test Vehicles,” University of Victoria, 2014.

[21] C. D. Regan and C. V Jutte, “Survey of Applications of Active Control Technology for Gust Alleviation and New Challenges for Lighter-weight Aircraft,” no. April, p. 19, 2012.

[22] P. Knott, C. Loecker, S. Algermissen, and R. Sekora, “Vibration Control and Structure Integration of Antennas on Aircraft – Research in NATO SET-131,” *IEEE*, no. Eucap, pp. 2651–2654, 2013.

[23] M. Urcia and D. Banks, “Structurally integrated phased arrays,” *IEEE Aerosp. Conf. Proc.*, 2011.

[24] J. Richards, A. Suleman, T. Aarons, and R. Canfield, “Multidisciplinary Design for Flight Test of a Scaled Joined Wing SensorCraft,” *13th AIAA/ISSMO Multidiscip. Anal. Optim. Conf.*, Sep. 2010.

[25] H. Schippers, J. H. Van Tongeren, P. Knott, T. Deloues, P. Lacomme, and M. R. Scherbarth, “Vibrating antennas and compensation techniques Research in NATO/RTO/SET 087/RTG 50,” *IEEE Aerosp. Conf. Proc.*, 2007.

[26] A. Burner, G. Fleming, and J. Hoppe, “Comparison of Three Optical Methods for Measuring Model Deformation,” *38th Aerosp. Sci. Meet. Exhib.*, no. January, 2000.

[27] J. Mura, “A Photogrammetric-Based Method for the Measurement of Static Deflections of an RPA Wing,” University of Rome, 2017.

[28] A. W. Burner, W. A. Lokos, and D. A. Barrows, “In-flight aeroelastic measurement technique development,” in *SPIE*, 2003, no. 3, p. 186.

[29] A. W. Burner and T. Liu, “Videogrammetric Model Deformation Measurement Technique,” *J. Aircr.*, vol. 38, no. 4, pp. 745–754, Jul. 2001.

[30] A. W. Burner, W. A. Lokos, and D. A. Barrows, “Aeroelastic Deformation : Adaptation of Wind Tunnel Measurement Concepts to Full-Scale Vehicle Flight Testing,” 2005.

[31] G. a. Fleming and S. a. Gorton, “Measurement of rotorcraft blade deformation using projection moire interferometry,” 1998, vol. 3411, pp. 514–527.

[32] V. M. Deangelis and R. Fondale, “Electro-optical flight deflection measurement system,” in *Society of Flight Test Engineers*, 1987, pp. 22–1 to 22–14.

[33] W. L. Ko, W. L. Richards, and V. T. Tran, “Displacement Theories for In-Flight Deformed Shape Predictions of Aerospace Structures,” 2007.

[34] V. T. F. W. L. Ko, W. L. Richards, “Applications of KO Displacement Theory to the Deformed Shape Predictions of the October 2009,” 2009.

[35] J. Bakalyar and C. Jutte, “Validation Tests of Fiber Optic Strain-Based Operational Shape and Load Measurements,” in *AIAA*, 2012.

[36] A. R. Parker, A. Piazza, and W. L. Richards, “Fiber-optic sensing system: Overview, development and deployment in flight at NASA,” *2015 IEEE Avion. Veh. Fiber-Optics Photonics Conf.*, vol. 2, pp. 71–73, 2015.

[37] U. S. Chan, Patrick (NASA Armstrong Flight Research Center, Edwards, CA, “Fiber Optics Sensing System (FOSS) at NASA Armstrong Flight Research Center (AFRC): Summary and Recent Deployments,” 2018.

[38] C. V Jutte, W. L. Ko, C. A. Stephens, J. A. Bakalyar, W. L. Richards, and A. R. Parker, “Deformed Shape Calculation of a Full-Scale Wing Using Fiber Optic Strain Data from a Ground Loads Test,” *NASA*, no. December, 2011.

[39] D. R. Gaukroger and C. J. W. Hassal, “Measurement of Vibratory Displacements of a Rotating Blade,” *Vertica*, vol. 2, pp. 111–120, 1978.

[40] W. G. Bousman, “Estimation of Blade Airloads from Rotor Blade Bending Moments Estimation of Blade Airloads from Rotor Blade Bending Moments,” no. August, p. 24, 1987.

[41] G. C. Foss and E. D. Haugse, “Using Modal Test Results to Develop Strain to Displacement Transformations,” *IMAC*, vol. 1, pp. 112–118, 1995.

[42] P. Bogert, E. Haugse, and R. Gehrki, “Structural Shape Identification From Experimental Strain Using a Modal Transformation Technique,” *44th AIAA/ASME/ASCE/AHS/ASC*, vol. 1–7, no. 2003–1626, 2003.

[43] A. Skafte, M. L. Aenlle, and R. Brincker, “A general procedure for estimating dynamic displacements using strain measurements and operational modal

analysis," *Smart Mater. Struct.*, vol. 25, no. 2, Jan. 2016.

[44] S. Warwick, M. Bras, J. Richards, and A. Suleman, "Measurement of Aeroelastic Wing Deflections Using Modal Shapes and Strain Pattern Analysis," in *AIAA Scitech 2019 Forum*, 2019.

[45] S. Keil, *Technology and Practical Use of Strain Gages: With Particular Consideration of Stress Analysis Using Strain Gages*. Wiley, 2017.

[46] "Strain gauge," *Wikipedia*, 2020. [Online]. Available: https://en.wikipedia.org/wiki/Strain_gauge. [Accessed: 11-Jan-2011].

[47] K. O. Hill, Y. Fujii, D. C. Johnson, and B. S. Kawasaki, "Photosensitivity in optical fiber waveguides: Application to reflection filter fabrication," *Appl. Phys. Lett.*, vol. 32, no. 10, pp. 647–649, May 1978.

[48] L. Melo, G. Burton, S. Warwick, and P. M. Wild, "Experimental Investigation of Long-Period Grating Transition Modes to Monitor CO 2 in High-Pressure Aqueous Solutions," *J. Light. Technol.*, vol. 33, no. 12, pp. 2554–2560, 2015.

[49] K. Hsu, A. Csipkes, and T. Jin, "Small-Diameter Thin FBGs Ideally Suited for Embedded Sensing in Composites," pp. 17–20.

[50] W. L. Richards, D. G. Lee, A. Piazza, A. K. Stewart, and G. P. Carman, "Characterization of embedded fiber optic sensors in advanced composite materials for structural health monitoring," 2004, vol. 5390, p. 505.

[51] Y. Fan and M. Kahrizi, "Characterization of a FBG strain gage array embedded in composite structure," *Sensors Actuators A Phys.*, vol. 121, no. 2, pp. 297–305, Jun. 2005.

[52] J. A. Guemes and J. M. Menéndez, "Response of Bragg grating fiber-optic sensors when embedded in composite laminates," *Compos. Sci. Technol.*, vol. 62, no. 7–8, pp. 959–966, 2002.

[53] M. C. Emmons, G. P. Carman, K. P. Mohanchandra, and W. L. Richards, "Characterization and birefringence effect on embedded optical fiber Bragg gratings," *Proc. SPIE*, vol. 7295, no. April 2009, pp. 72950C-72950C–11, 2009.

[54] A. Brandt, *NOISE AND VIBRATION ANALYSIS SIGNAL ANALYSIS AND*. West Sussex: Wiley, 2010.

[55] S. C. Chapra and R. P. Canale, *Numerical Methods for Engineers*, 5th ed. McGraw Hill, 2006.

[56] C. Lanczos, "An iteration method for the solution of the eigenvalue problem of linear differential and integral operators," *J. Res. Natl. Bur. Stand. (1934).*, vol. 45, no. 4, p. 255, Oct. 1950.

[57] I. U. OJALVO and M. NEWMAN, "Vibration modes of large structures by an

automatic matrix-reductionmethod," *AIAA J.*, vol. 8, no. 7, pp. 1234–1239, Jul. 1970.

[58] J. W. Cooley and J. W. Tukey, "An Algorithm for the Machine Calculation of Complex Fourier Series," *Math. Comput.*, vol. 19, no. 90, p. 297, Apr. 1965.

[59] P. Avitabile, *Modal Testing: A Practitioner's Guide*. 2017.

[60] J. Carregado, S. Warwick, J. Richards, F. Engelsen, and A. Suleman, "Static and Dynamic Characterization of a Flexible Scaled Joined Wing UAV," *Adv. Aircr. Spaceraft Sci.*, vol. 6, no. 2, p. 116, 2019.

[61] M. H. Richardson and D. L. Formenti, "Global Curve Fitting of Frequency Response Measurements using the Rational Fraction Polynomial Method," 1985.

[62] M. Drela, "ASWING," *Massachusetts Institute of Technology*. [Online]. Available: http://web.mit.edu/drela/Public/web/aswing/. [Accessed: 17-Feb-2020].

[63] M. Drela, "Integrated simulation model for preliminary aerodynamic, structural, and control-law design of aircraft," in *40th Structures, Structural Dynamics, and Materials Conference and Exhibit*, 1999.

[64] "ASM.MATWEB: ALUMINUM 6061-T6." [Online]. Available: http://asm.matweb.com/search/SpecificMaterial.asp?bassnum=ma6061t6. [Accessed: 12-Mar-2017].

[65] SAE, "Composite Materials Handbook Volume 2 . Polymer Matrix Composites Material Properties," *J. Mech. Work. Technol.*, vol. 2, no. 2F, p. 126, 2012.

[66] A. C. Inc., "ACP Composites Inc," 2017. [Online]. Available: https://store.acpsales.com/.

[67] N. Tourjansky and E. Széchényi, "The Measurement of Blade Deflections," *Eighteenth Eur. Rotorcr. Forum*, p. 13, 1992.

[68] N. Mocho, "Design of A Ground Vibration Test Certification System For Unmanned Air Vehicles," Technico Lisboa, 2015.

[69] FEMtools, "FEMtools: Model Updating Theoretical Manual," *Dyn. Des. Solut. NV, Belgium, www.femtools.com*, 2014.

[70] E. Dascotte, "Custom FEMtools ANSYS STATIC DRIVER," 2017.

[71] A. Kotikalpudi, D. K. Schmidt, C. D. Regan, and P. J. Seiler, "Real-time Shape Estimation for Flexible Unmanned Air Vehicle via Kalman Filtering," in *AIAA Scitech 2020 Forum*, 2020.

Appendix A - Composite Component Layup Schedule

						1	2	3	4	5
Laminate Layer	Reinforced Wing	Thick Skins	Non Thick Skins	Fuse		TIP RIB	RIGID SECTION	TIP JOINT	FLEXIBLE SECTION	ROOT JOINT
Layer 1	Duratech	Duratech	Duratech	Duratech		Duratech	Duratech	Duratech	Duratech	Duratech
Layer 2	3.4 oz glass	3.4 oz glass	3.4 oz glass	8.9 oz glass		3.4 oz glass	3.4 oz glass	3.4 oz glass	3.4 oz glass	3.4 oz glass
Layer 3	6 oz uni carbon	3.4 oz glass	3.4 oz glass	5oz kevlar		6 oz uni carbon	6 oz uni carbon	6 oz uni carbon	1/8 Foam Core	5.7 oz Woven Carbon
Layer 4	5.7 oz Woven Carbon	1/8 Foam Core	3.4 oz glass	1/8 Foam Core		5.7 oz Woven Carbon	1/8 Foam Core	6 oz uni carbon	3.4 oz glass	5.7 oz Woven Carbon
Layer 5		3.4 oz glass		3.4 oz glass		3.4 oz glass	3.4 oz glass	5.7 oz Woven Carbon		6 oz uni carbon
Layer 6								3.4 oz glass		6 oz uni carbon
Layer 7										5.7 oz Woven Carbon
Layer 8										3.4 oz glass
Layer 9										
Layer 10	Bonding Gap	Bonding Gap				Bonding Gap	Bonding Gap	Bonding Gap	Bonding Gap	Bonding Gap
Thickness (mm)	**1.652**	**4.611**	**0.436**	**3.909**		**1.746**	**4.724**	**1.954**	**4.516**	**2.348**
Density (g/mm^3)	6.15E-04	1.90E-04	1.67E-03	3.30E-04		6.79E-04	2.18E-04	7.72E-04	1.57E-04	9.03E-04
Areal Weight (g/m^2)	**1015**	**878**	**726**	**1290**		**1185**	**1031**	**1508**	**708**	**2121**

Appendix B - ANSYS FE Model Workspace

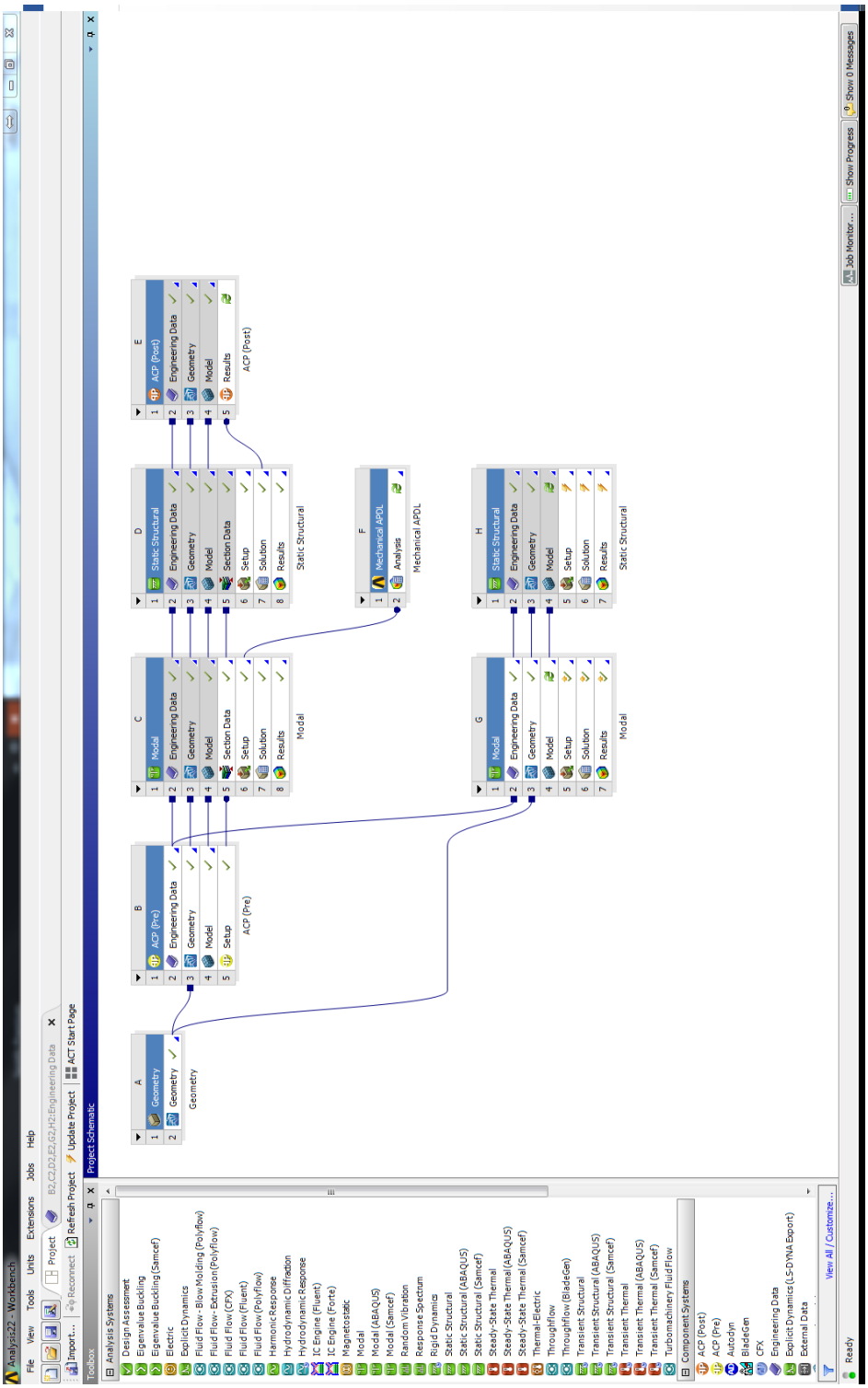

Appendix C - ANSYS APDL STATIC POST PROCESSING

```
!  Commands inserted into this file will be executed immediately after the ANSYS
/POST1 command.

!  Active UNIT system in Workbench when this object was created:  Metric (mm, kg,
N, s, mV, mA)
!  NOTE:  Any data that requires units (such as mass) is assumed to be in the
consistent solver unit system.
!            See Solving Units in the help system for more information.
!Analysis 7
!Version 1.0
!RESUME

irlf,-1
ALLSEL,ALL,ALL

!!!!!!!!!!!!!!!!!!!!!! CLEAR RESULTS !!!!!!!!!!!!!!!!!!!
/DELETE,strainStatic_TOP,txt
/DELETE,strainStatic_X1_TOP,txt
/DELETE,strainStatic_X2_TOP,txt
/DELETE,strainStatic_BOTTOM,txt
/DELETE,strainStatic_X1_BOTTOM,txt
/DELETE,strainStatic_X2_BOTTOM,txt
/DELETE,dispStatic,txt
/DELETE,dispStaticROT,txt
/DELETE,nodeLocations_MEASUREMENTLOCATIONS,txt
!/DELETE,dispStatic_MEASUREMENTLOCATIONS,txt

rsys, 12


set,first
! strainStatic_TOP.txt Output
!cmsel,s,,ELEM
cmsel,s,strainLocations_TOP
ESLN,S
SHELL, TOP

etable,cx,cent,x
etable,cy,cent,y
```

```
etable,cz,cent,z
etable,epsx,epel,x
etable,epsy,epel,y
etable,epsz,epel,z
etable,tauyz,epel,xz


/PAGE,100000,100000,100000,100000
/HEADER,OFF,OFF,ON,ON,OFF,OFF
/FORMAT,,,17,9
/output,strainStatic_TOP,txt,,append
pretab,cx,cy,cz,epsx,epsy,epsz,tauyz
/out

!!!!!!!!!!!!!!!!!!!! Strain Centerline Bottom !!!!!!!!!!!!!!!!!!
set,first
! strainStatic_BOTTOM.txt Output
!cmsel,s,,ELEM
cmsel,s,strainLocations_BOT
ESLN,S
SHELL, BOT

etable,cx,cent,x
etable,cy,cent,y
etable,cz,cent,z
etable,epsx,epel,x
etable,epsy,epel,y
etable,epsz,epel,z
etable,tauyz,epel,xz


/PAGE,100000,100000,100000,100000
/HEADER,OFF,OFF,ON,ON,OFF,OFF
/FORMAT,,,17,9
/output,strainStatic_BOTTOM,txt,,append
pretab,cx,cy,cz,epsx,epsy,epsz,tauyz
/out

!!!!!!!!!!!!!!!!!!!!!!! Disp ALL !!!!!!!!!!!!!!!!!!!!!!
set,first
! dispStatic.txt output file
nsel,all
```

```
/PAGE,100000,100000,100000,100000
/HEADER,OFF,OFF,ON,ON,OFF,OFF
/FORMAT,,,17,9

/output,dispStatic,txt,,append
prnsol,U,sum
/out

set,first
! dispStaticROT.txt output file
nsel, all
/PAGE,100000,100000,100000,100000
/HEADER,OFF,OFF,ON,ON,OFF,OFF
/FORMAT,,,17,9
/output, dispStaticROT,txt,,append
prnsol,ROT,SUM
/out

!!!!!!!!!!! Disp ALL MEASUREMENT NODES STATIC !!!!!!!!!!
rsys, 0

set,first
! dispStatic.txt output file
cmsel,s,GROUNDTEST_STATICLOAD_MEASUREMENT
/PAGE,100000,100000,100000,100000
/HEADER,OFF,OFF,ON,ON,OFF,OFF
/FORMAT,,,17,9
/output,dispStatic_MEASUREMENTLOCATIONS,txt,,append
prnsol,U,sum
/out

cmsel,s,GROUNDTEST_STATICLOAD_MEASUREMENT
/PAGE,100000,100000,100000,100000
/HEADER,OFF,OFF,OFF,OFF,OFF,OFF
/FORMAT,,,17,9
/output,nodeLocations_MEASUREMENTLOCATIONS,txt
NLIST,ALL, , ,XYZ,NODE,NODE,NODE
/out
```

Appendix D - ANSYS APDL MODAL POST PROCESSING

```
!  Commands inserted into this file will be executed immediately after the ANSYS
/POST1 command.

!  Active UNIT system in Workbench when this object was created:  Metric (mm, kg,
N, s, mV, mA)
!  NOTE:  Any data that requires units (such as mass) is assumed to be in the
consistent solver unit system.
!           See Solving Units in the help system for more information.
!RESUME

/DELETE,strainModes_TOP,txt
/DELETE,strainModes_BOTTOM,txt
/DELETE,dispModes,txt
/DELETE,nodeLocations,txt
/DELETE,elementNodes,txt
/DELETE,dispModesROT,txt

dsys, 12

nsel,all
/PAGE,100000,100000,100000,100000
/HEADER,OFF,OFF,OFF,OFF,OFF,OFF
/FORMAT,,,17,9
/output,nodeLocations,txt
NLIST,ALL, , ,XYZ,NODE,NODE,NODE
/out

esel,all
/PAGE,100000,100000,100000,100000
/HEADER,OFF,OFF,OFF,OFF,OFF,OFF
/FORMAT,,,17,9
/output,elementNodes,txt
ELIST,ALL, , ,XYZ
/out

cmsel,s,strainLocations_TOP
ESLN,S
/PAGE,100000,100000,100000,100000
/HEADER,OFF,OFF,OFF,OFF,OFF,OFF
```

```
/FORMAT,,,17,9
/output,elementNodes_TOP,txt
ELIST,ALL, , ,XYZ
/out

cmsel,s,strainLocations_BOT
ESLN,S
/PAGE,100000,100000,100000,100000
/HEADER,OFF,OFF,OFF,OFF,OFF,OFF
/FORMAT,,,17,9
/output,elementNodes_BOT,txt
ELIST,ALL, , ,XYZ
/out

rsys, 12
!!!!!!!!!!!!!!!!!!!! StrainMode Centerline Top!!!!!!!!!!!!!!!!!!!!
! Create Output for strainModes_TOP.txt and dispModes.txt
! cmsel,s,,ELEM
cmsel,s,strainLocations_TOP
ESLN,S
SHELL, TOP
set,first
*do,index,1,25,1
        ! cmsel,s,,ELEM
        cmsel,s,strainLocations_TOP
        ESLN,S
        SHELL, TOP
        etable,cx,cent,x
        etable,cy,cent,y
        etable,cz,cent,z
        etable,epsx,epel,x
        etable,epsy,epel,y
        etable,epsz,epel,z
        etable,tauxy,epel,xz

        /PAGE,100000,100000,100000,100000
        /HEADER,OFF,OFF,OFF,OFF,OFF,OFF
        /FORMAT,,,17,9
        /output,strainModes_TOP,txt,,append
        pretab,cx,cy,cz,epsx,epsy,epsz,tauxy
        /out
```

```
        ! Displacement Mode Shapes Output!!!!!!
        nsel,all
        /PAGE,100000,100000,100000,100000
        /HEADER,OFF,OFF,OFF,OFF,OFF,OFF
        /FORMAT,,,17,9
        /output,dispModes,txt,,append
        prnsol,U,sum
        /out

        ! Displacement Mode Shape Rotations Output!!!!!!
        nsel,all
        /PAGE,100000,100000,100000,100000
        /HEADER,OFF,OFF,OFF,OFF,OFF,OFF
        /FORMAT,,,17,9
        ! dispModesROT.txt output file
        nsel, all
        /output, dispModesROT,txt,,append
        prnsol,ROT,SUM
        /out
        set,next
*enddo

!!!!!!!!!!!!!!!!!!!!! StrainMode Centerline BOTTOM!!!!!!!!!!!!!!!!!!!!!!
! Create Output for strainModes_TOP.txt and dispModes.txt
! cmsel,s,,ELEM
cmsel,s,strainLocations_BOT
ESLN,S
SHELL, BOT
set,first
*do,index,1,25,1
        ! cmsel,s,,ELEM
        cmsel,s,strainLocations_BOT
        ESLN,S
        SHELL, BOT
        etable,cx,cent,x
        etable,cy,cent,y
        etable,cz,cent,z
        etable,epsx,epel,x
        etable,epsy,epel,y
        etable,epsz,epel,z
        etable,tauxy,epel,xz
```

```
        /PAGE,100000,100000,100000,100000
        /HEADER,OFF,OFF,OFF,OFF,OFF,OFF
        /FORMAT,,,17,9
        /output,strainModes_BOTTOM,txt,,append
        pretab,cx,cy,cz,epsx,epsy,epsz,tauxy
        /out
        set,next
*enddo
```

Appendix E - ASE MEASURANDS

Struct Name	Variable Name	Description	Unit	Sample Rate
AFTU				
	FlightTestID	Vector of n x 3 size that describes the test ID. First colum is Flight Number, second is Sortie Number, and the third is the Test Number. This Test ID will correspond to a line in the AFTU Test Card for theflight, where n is the number of tests in the flight	N/A	N/A
	FlightTestTimeStartStop	Vector of n x 2 size that describes the start and end time of each test in in nanoseconds since 12am UTC January 1st, 2014, where n is the number of tests in the flight.	nanoseconds	
	FlightTestIndexStartStop	Vector of n x 2 size that describes the start and end row index of each test, where n is the number of tests in the flight.		
	FlightTestDuration	Vector of n x 1 size that describes the test duration of each test, where n is the number of test in the flight.	seconds	
SerialDataAirDataBoom				
	Sample	Vectr of n x 1 size tha describes the sample number. Increments by one for every sample		2000Hz (resampled)
	Airspeed	Vectr of n x 1 size tha describes the airspeed of the aircraft in m/s, where n is the number of samples in the flight	m/s	2000Hz (resampled)
	AoA	Vectr of n x 1 size tha describes Angle of Attack of the aircraft in degrees, where n is the number of samples in the flight.	degrees	2000Hz (resampled)
	AoS	Vectr of n x 1 size that describes Angle of Slip of the aircraft in degrees, where a positive number corresponds to right slip.	degrees	2000Hz (resampled)
	A	Vectr of n x 1 size that describes Pressure Altitude of the aircraft in meters.	meters	2000Hz (resampled)
	Ps	Vectr of n x 1 size that describes Static Pressure.	degrees	2000Hz (resampled)
	Pt	Vectr of n x 1 size that describes Total Pressure.	degrees	2000Hz (resampled)

	TimeStamp	Vector of n x 1 size that describes the time of the corresponding sample in nanoseconds since 12am UTC January 1st, 2014, where n is the number of samples in the flight.	nanoseconds	2000Hz (resampled)
SerialDataDSMXBinary				
	Data	Vector of n x 16 size that describes the raw data from the RF reciever which corresponds to control surface inputs to the aircraft. This gest converted to SerialDataDSMXCommands, which make it human readable. n is the number of samples in the flight.		2000Hz (resampled)
SerialDataDSMXCommands				
	AileronRollDSMX	Vector of n x 1 size that describes either the commanded aileron deflection (when in manual mode), or commanded bank angle (when in fly-by-wire mode) from the reciever to the autopilot. A positive commanded aileron deflection coresponds to aileron commands that roll the aircraft right. A positve commanded bank angle results in the aircraft rolling right. n is the number of samples in the flight.	degrees	2000Hz (resampled)
	ElevatorPitchDSMX	Vector of n x 1 size that describes either the commanded elevator deflection (when in manual mode), or commanded pitch angle (when in fly-by-wire mode) from the reciever to the autopilot. A positive commanded elevator deflection coresponds to elevator commands that increases lift in the tail, causing the aircraft to pitch down. A positve commanded pitch angle results on the aircraft pitching up. n is the number of samples in the flight.	degrees	2000Hz (resampled)
	RudderDSMX	Vector of n x 1 size that describes the commanded rudder deflection from the reciever to the autopilot. A positive commanded rudder deflection coresponds to rudder	degrees	2000Hz (resampled)

		commands that yaw the aircraft right. n is the number of samples in the flight.		
	FlapDSMX	Vector of n x 1 size that describes the commanded flaperon deflection from the reciever to the autopilot. Flaperons are when the ailerons are used as flaps by superimposing a symetric deflection in both ailerons. A positive commanded flap deflection coresponds to both ailerons dropping and increasing the lift in the wing. n is the number of samples in the flight.	degrees	2000Hz (resampled)
	ThrottleDSMX	Vector of n x 1 size that describes the commanded throttle position between zero and one hundred percent from the reciever to the autopilot. n is the number of samples in the flight.	%	2000Hz (resampled)
	AutopilotModeDSMX	Vector of n x 1 size that describes the commanded autopilot mode. "0" corresponds to open-loop and "1" corresponds to closed-loop. n is the number of samples in the flight.	N/A	2000Hz (resampled)
	TimeStamp	Vector of n x 1 size that describes the time of the corresponding sample in nanoseconds since 12am UTC January 1st, 2014, where n is the number of samples in the flight.	nanoseconds	2000Hz (resampled)
SerialDataVectorNav				
	Yaw	Vector of n x 1 size that describes the processed yaw angle of the the aircraft with respect to north, as calculated by the IMU, where n is the number of samples in the flight.	Degree	2000Hz (resampled)
	Pitch	Vector of n x 1 size that describes the processed pitch angle of the aircraft with respect to the ground plane as calculated by th IMU, where n is the number of samples in the flight.	Degree	2000Hz (resampled)

	Roll	Vector of n x 1 size that describes the processed roll angle of the aircraft with respect to the ground plane, as calculated by the IMU, where n is the number of samples in the flight.	Degree	2000Hz (resampled)
	MagX			2000Hz (resampled)
	MagY			2000Hz (resampled)
	MagZ			2000Hz (resampled)
	AccelX	Vector of n x 1 size that describes the acceleration of the aircraft in the X-direction, where n is the number of samples in the flight.	m/s^2	2000Hz (resampled)
	AccelY	Vector of n x 1 size that describes the acceleration of the aircraft in the Z-direction, where n is the number of samples in the flight.	m/s^2	2000Hz (resampled)
	AccelZ	Vector of n x 1 size that describes the acceleration of the aircraft in the Y-direction, where n is the number of samples in the flight.	m/s^2	2000Hz (resampled)
	GyroX	Vector of n x 1 size that describes the angular rate of the aircraft in the X-axis of the IMU, where n is the number of samples in the flight.	rad/s	2000Hz (resampled)
	GyroY	Vector of n x 1 size that describes the angular rate of the aircraft in the Y-axis of the IMU, where n is the number of samples in the flight.	rad/s	2000Hz (resampled)
	GyroZ	Vector of n x 1 size that describes the angular rate of the aircraft in the Z-axis of the IMU, where n is the number of samples in the flight.	rad/s	2000Hz (resampled)
	TimeSincePPS	Vector of n x 1 size that describes the time since the last rising edge of the PPS signal from the GPS, where n is the number of tests in the flight.	nanoseconds	2000Hz (resampled)
	TimeStamp	Vector of n x 1 size that describes the time of the corresponding sample in nanoseconds since 12am UTC January 1st, 2014, where n is the number of samples in the flight.	nanoseconds	2000Hz (resampled)

TimeDataAccelerometer				
	A1.Data	Vector of n x 1 size that describes the acceleration of accelarometer "1" in the direction perpendicular to the spar where it is applied, where n is the number of samples in the flight.	m/s^2	2000Hz
	A2.Data	Vector of n x 1 size that describes the acceleration of accelarometer "2" in the direction perpendicular to the spar where it is applied, where n is the number of samples in the flight.	m/s^2	2000Hz
	A3.Data	Vector of n x 1 size that describes the acceleration of accelarometer "3" in the direction perpendicular to the spar where it is applied, where n is the number of samples in the flight.	m/s^2	2000Hz
	A4.Data	Vector of n x 1 size that describes the acceleration of accelarometer "4" in the direction perpendicular to the spar where it is applied, where n is the number of samples in the flight.	m/s^2	2000Hz
	A5.Data	Vector of n x 1 size that describes the acceleration of accelarometer "5" in the direction perpendicular to the spar where it is applied, where n is the number of samples in the flight.	m/s^2	2000Hz
	A6.Data	Vector of n x 1 size that describes the acceleration of accelarometer "6" in the direction perpendicular to the spar where it is applied, where n is the number of samples in the flight.	m/s^2	2000Hz
	A7.Data	Vector of n x 1 size that describes the acceleration of accelarometer "7" in the direction perpendicular to the spar where it is applied, where n is the number of samples in the flight.	m/s^2	2000Hz
	A8.Data	Vector of n x 1 size that describes the acceleration of accelarometer "8" in the direction perpendicular to the spar where it is applied, where n is the number of samples in the flight.	m/s^2	2000Hz
TimeDataActuatorCommands				
	Aileron_Left	Vector of n x 1 size describing the the commanded surface angle	degrees	2000Hz (resampled)

		to the Left Aileron. A positive value induces positve lift in the surface. n is the number of samples in the flight.		
	Aileron_Right	Vector of n x 1 size describing the the commanded surface angle to the Right Aileron. A positive value induces positve lift in the surface. n is the number of samples in the flight.	degrees	2000Hz (resampled)
	Elevator	Vector of n x 1 size describing the the commanded surface angle to the Elevator. A positive value induces positve lift in the surface. n is the number of samples in the flight.	degrees	2000Hz (resampled)
	Rudder	Vector of n x 1 size describing the the commanded surface angle to the Rudder. A positive value induces positve lift in the surface. n is the number of samples in the flight.	degrees	2000Hz (resampled)
	ESC	Vector of n x 1 size describing the the commanded output of the Electronic Speed Controller (ESC), between 0% and 100%. n is the number of samples in the flight.	%	2000Hz (resampled)
TimeDataActuatorFeedback				
	Aileron_Left	Vector of n x 1 size describing the the feedback angle from the actuator of the Left Aileron. A positive value induces positve lift in the surface. n is the number of samples in the flight.	degrees	2000Hz
	Aileron_Right	Vector of n x 1 size describing the the feedback angle from the actuator of the Right Aileron. A positive value induces positve lift in the surface. n is the number of samples in the flight.	degrees	2000Hz
	Elevator_Left	Vector of n x 1 size describing the the feedback angle from the actuator of the Left Elevator A positive value induces positve lift in the surface. n is the number of samples in the flight.	degrees	2000Hz

	Elevator_Right	Vector of n x 1 size describing the the feedback angle from the actuator of the Right Elevator. A positive value induces positve lift in the surface. n is the number of samples in the flight.	degrees	2000Hz
	Flap_Left	Not used in Flexible Aircraft		
	Flap_Right	Not used in Flexible Aircraft		
	Rudder	Vector of n x 1 size describing the the feedback angle from the actuator of the Rudder. A positive value inducesa moment that yaws the aircraft to the right. n is the number of samples in the flight.	degrees	2000Hz
TimeDataFPGATimeStamp				
	TimeStamp	Vector of n x 1 size that describes the time of the corresponding sample in nanoseconds since 12am UTC January 1st, 2014, where n is the number of samples in the flight.	nanoseconds	2000Hz
TimeDataPPS				
	Data	Vector of n x 1 size that describes the stae of the PPS signal from the GPS, where n is the number of samples in the flight. "1" denotes High, and "0" denotes low	N/A	2000Hz
TimeDataStrain_LeftWing				
		Vector of n x 16 size that describes the strain for each Strain Bridge in the Left Wing, where n is the number of samples in the flight.	micro strain	2000Hz
TimeDataStrain_RightWing				
		Vector of n x 16 size that describes the strain for each Strain Bridge in the Right Wing, where n is the number of samples in the flight.		2000Hz
UAVCalibration				
	Version	The version of calibration used for the autopilot		N/A
	Aileron_Left	Vector of 10 x 3 size that describes surface mapping of the Left Aileron. The first column correponds to PWM values in milliseconds sent to the left Aileron actuator. The middle		N/A

		column corresponds to the surface angle. The right column corresponds to the feedback voltage of the actuator at that angle.	
	Aileron_Right	Vector of 10 x 3 size that describes surface mapping of the Right Aileron. The first column correponds to PWM values in milliseconds sent to the left Aileron actuator. The middle column corresponds to the surface angle. The right column corresponds to the feedback voltage of the actuator at that angle.	N/A
	Elevator_Left	Vector of 10 x 3 size that describes surface mapping of the Left Elevator. The first column correponds to PWM values in milliseconds sent to the left Aileron actuator. The middle column corresponds to the surface angle. The right column corresponds to the feedback voltage of the actuator at that angle.	N/A
	Elevator_Right	Vector of 10 x 3 size that describes surface mapping of the Right Elevator. The first column correponds to PWM values in milliseconds sent to the left Aileron actuator. The middle column corresponds to the surface angle. The right column corresponds to the feedback voltage of the actuator at that angle.	N/A
	Rudder	Vector of 10 x 3 size that describes surface mapping of the Rudder. The first column correponds to PWM values in milliseconds sent to the left Aileron actuator. The middle column corresponds to the surface angle. The right column corresponds to the feedback voltage of the actuator at that angle.	N/A
	Flap_Left	N/A	N/A
	Flap_Right	N/A	N/A
	ESC	Vector of 10 x 2 size that describes surface mapping of the Electronic Speed Controller (ESC). The first column correponds to	N/A

		PWM values in milliseconds sent to the ESC. The last column corresponds to the Throttle Percentage.		
	AileronLimit_Max	Maximum commanded Aileron deflection	degrees	N/A
	ElevatorLimit_Max	Maximum commanded Elevator deflection	degrees	N/A
	RudderLimit_Max	Maximum commanded Rudder deflection	degrees	N/A
	FlapLimit_Max	Maximum commanded Flap deflection	degrees	N/A
	ESCLimitMax	Maximum commanded Throttle position	%	N/A
	PitchLimit_Max	Maximum commanded Pitch angle	degrees	N/A
	RollLimit_Max	Maximum commanded Roll angle	degrees	N/A
	AileronLimit_Min	Minimum commanded Aileron deflection	degrees	N/A
	ElevatorLimit_Min	Minimum commanded Elevator deflection	degrees	N/A
	RudderLimit_Min	Minimum commanded Rudder deflection	degrees	N/A
	FlapLimit_Min	Minimum commanded Flap deflection	degrees	N/A
	ESCLimit_Min	Minimum commanded Throttle position	%	N/A
	PitchLimit_Min	Minimum commanded Pitch angle	degrees	N/A
	RollLimit_Min	Minimum commanded Roll angle	degrees	N/A
	AileronDSMX_Middle	The mid-span signal from the DSMX reciever for the Aileron in Manual and FBW modes		N/A
	ElevatorDSMX_Middle	The mid-span signal from the DSMX reciever for the Elevator in Manual and FBW modes		N/A
	RudderDSMX_Middle	The mid-span signal from the DSMX reciever for the Rudder in Manual and FBW modes		N/A
	ESCDSMX_Bottom	The mid-span signal from the DSMX reciever for the Electronic Speed Coontroller in Manual and FBW modes		N/A
	Aileron_Piccolo_Trim	Aileron surface trim value in Piccolo in FBW mode	degrees	N/A
	Elevator_Piccolo_Trim	Elevator surface trim value in Piccolo in FBW mode	degrees	N/A
	Throttle_Piccolo_Trim	Throttle surface trim value in Piccolo in FBW mode	%	N/A
	Rudder_Piccolo_Trim	Rudder surface trim value in Piccolo in FBW mode	degrees	N/A
	Flap_Piccolo_Trim	Flap surface trim value in Piccolo in FBW mode	degrees	N/A

Appendix F - Strain Gauge Circuit Reference

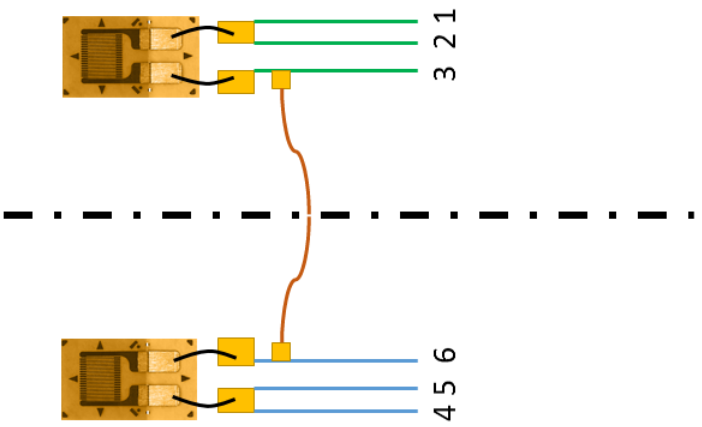

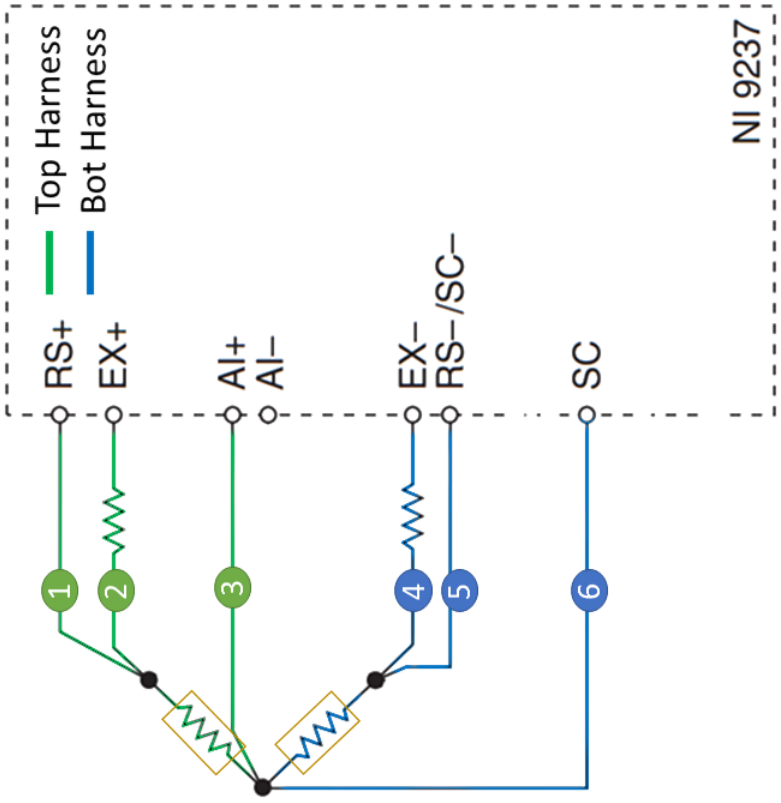

Appendix G - Strain Gauge Installation Drawings

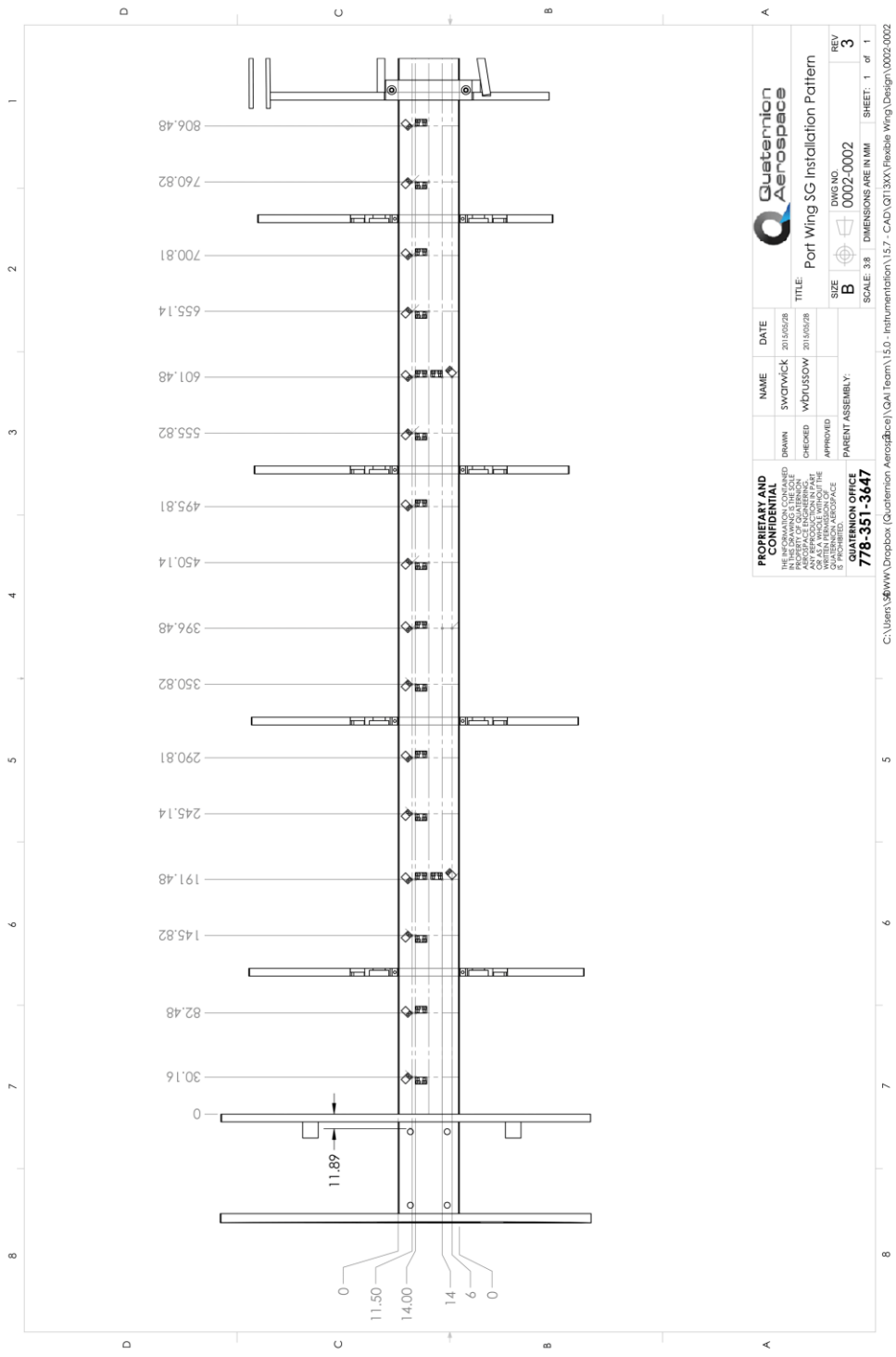

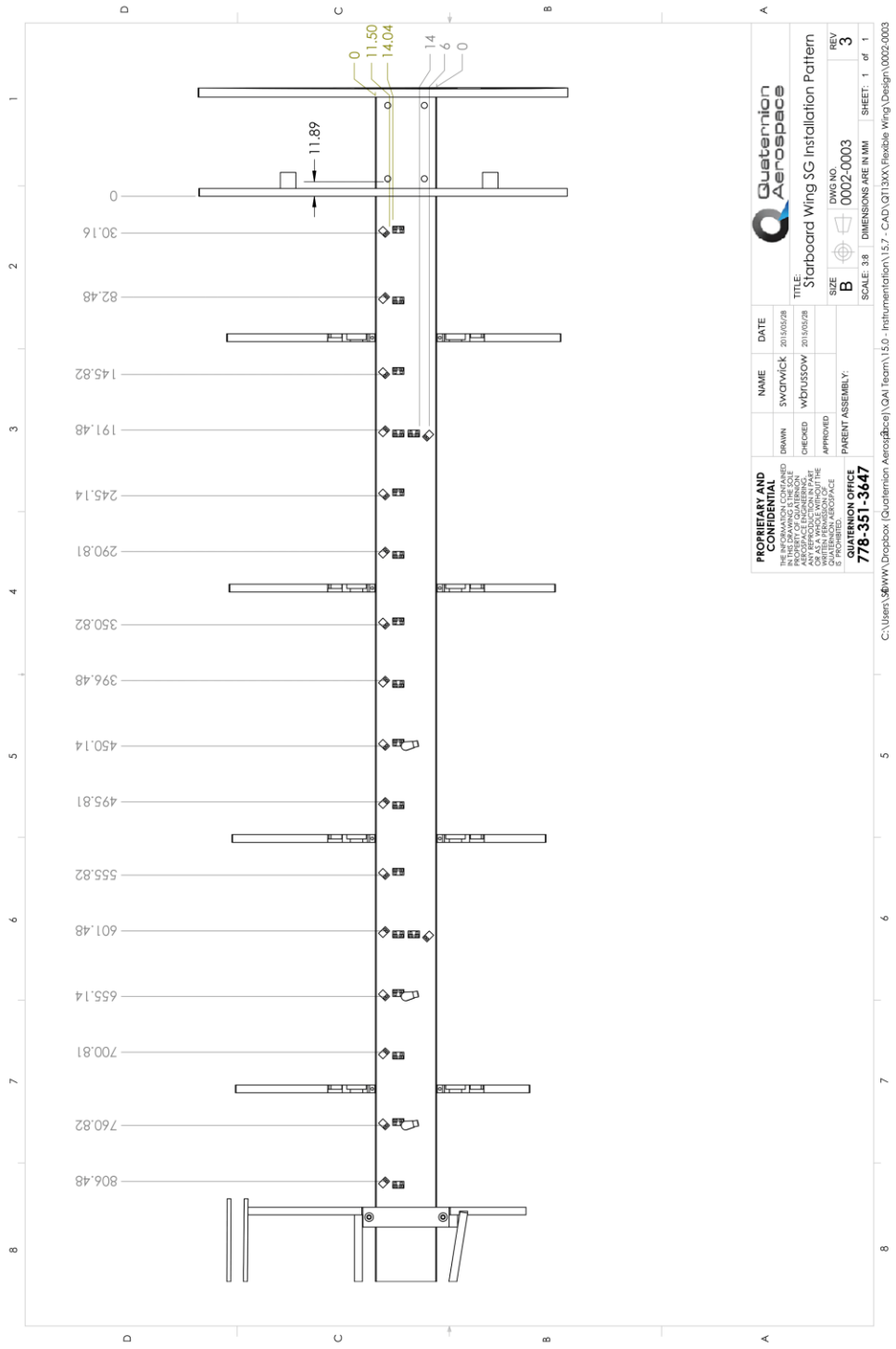
0
11.50
14.04
14
6
0
11.89
0
30.16
82.48
145.82
191.48
245.14
290.81
350.82
396.48
450.14
495.81
555.82
601.48
655.14
700.81
760.82
806.48
PROPRIETARY AND CONFIDENTIAL
THE INFORMATION CONTAINED IN THIS DRAWING IS THE SOLE PROPERTY OF QUATERNION AEROSPACE ENGINEERING. ANY REPRODUCTION IN PART OR AS A WHOLE WITHOUT THE WRITTEN PERMISSION OF QUATERNION AEROSPACE IS PROHIBITED.
QUATERNION OFFICE
778-351-3647
NAME
DATE
DRAWN
swartwick
2015/05/28
CHECKED
wbrussow
2015/05/28
APPROVED
PARENT ASSEMBLY:
Quaternion Aerospace
TITLE:
Starboard Wing SG Installation Pattern
SIZE
B
DWG NO.
0002-0003
REV
3
SCALE: 3/8
DIMENSIONS ARE IN MM
SHEET: 1 of 1
C:\Users\SB\WW\Dropbox (Quaternion Aerospace)\QAI Team\15.0 - Instrumentation\15.7 - CAD\QT13XX\Flexible Wing\Design\0002-0003

Appendix H- EXAMPLE SPA APPLICATION WRITTEN IN MATLAB

```
%% Load Flight Test Data with Strain Measurements, and Load SPA parameters
ExpStrainStatic_RAW_LW=load(eFDR_LOG_FlightData,TimeDataStrain_LeftWing);
ExpStrainStatic_RAW_RW=load(eFDR_LOG_FlightData,TimeDataStrain_RightWing);
load ('SPA_DELIVERY_ESA_20151110.mat');

ExpStrainStatic_RAW_LW = ExpStrainStatic_RAW_LW.Data;
ExpStrainStatic_RAW_RW = ExpStrainStatic_RAW_RW.Data;

%% Apply Gravity Deformation of spar Bias
ExpStrainStatic_LW=ExpStrainStatic_RAW_LW+(transpose(…
QT1302WingCalibrationBIAS(:,SemiWing)*1000000));
ExpStrainStatic_RW=ExpStrainStatic_RAW_RW+(transpose(…
QT1302WingCalibrationBIAS(:,SemiWing)*1000000));

%% Unit changes to match output from Ansys
ExpStrainStatic_LW = 2.*ExpStrainStatic_RW/1000000;
ExpStrainStatic_RW = 2.*ExpStrainStatic_LW/1000000;

%% Strain Calibration added to improve fit (some variability between spars)
ExpStrainStatic_LW = ExpStrainStatic_LW+b_eps_SPAR1;
ExpStrainStatic_RW = ExpStrainStatic_RW+b_eps_SPAR1;

%% Rename variables for clarity
eps_LW= ExpStrainStatic_LW;
eps_RW= ExpStrainStatic_RW;

%% Reduce the number of Mode shapes to those in Table 2
PhiD_Nastran0_LW=PhiD_Nastran0_LW (:,:,ReducedModesforAnalysis);
PhiD_Nastran0_RW=PhiD_Nastran0_RW (:,:,ReducedModesforAnalysis);
PhiS=PhiS(:,ReducedModesforAnalysis);

%% for loop to allow SPA operation on each individual time
step sampled
for i=1:length(ExpStrainStatic_LW;)

%% Transpose Experimental Strain for input in Least Squares method lsqlin
eps_LW= transpose(ExpStrainStatic_LW(i,:));
eps_RW= transpose(ExpStrainStatic_RW(i,:));

%% Perform least squares fit to solve Equation(5) for q
```

```
[q_LW, resnorm, residual] = lsqlin(PhiS, eps_LW);
[q_RW, resnorm, residual] = lsqlin(PhiS, eps_RW);
```

Appendix I - FEMTOOLS STATIC SCRIPTS

```
'--------------------------------------------------------------------------
' Custom ANSYS driver
'--------------------------------------------------------------------------
Sub Main()

  sAnsysBas = Ft_LocateScript("ansys.bas")
  sAnsysIni = Left(sAnsysBas, Len(sAnsysBas)-3) & "ini"
  sExecutable = ReadIni("LOCAL_NT", "exec", sAnsysIni)
' sExecutable = "C:\Program Files\Ansys Inc\v170\ANSYS\bin\winx64\ANSYS170.exe"
  sFlags    = "-b"
  sCdbName  = "tmp"
  sCdbFile  = sCdbName & ".cdb"
  sRstFile  = sCdbName & ".rst"
  sRunFile  = sCdbName & ".run"
  sOutFile  = sCdbName & ".out"

  Ft_Command "backup load"
  Ft_Command "clear load"
  Ft_Export "fem", "ansys", sCdbFile ' export current model, without loads
  Ft_Command "restore load"

  Kill sRunFile
  Kill sOutFile
  Open sRunFile For Output As #1
    Print #1, "/BATCH"
    Print #1, "/NERR,1"
    Print #1, "/NOPR"
```

```
        Print #1, "/FILNAM," & sCdbName
        Print #1, "/PREP7"
        Print #1, "SHPP,OFF" ' Disable element shape control
        Print #1, "/INPUT," & sCdbName & ",cdb"
        ' Define Load cases and Analysis Type
        ' Print #1, "FDELE, ALL, ALL"         ' Clear All Existing Forces
        Print #1, "F, 4084, FY, 15.7"      ' Define Nodal Force
           Print #1, "F, 4174, FY, 15.7"      ' Define Nodal Force
        Print #1, "ANTYPE,STATIC"           ' Set Static Analysis Type
        ' Done
        Print #1, "FINISH"
        Print #1, "/SOLU"
        Print #1, "OUTRES,ERASE"
        Print #1, "OUTRES,ALL,NONE"
        Print #1, "OUTRES,NSOL,ALL" ' Only write nodal displacements to .rst
        Print #1, "OUTPR,ERASE"
        Print #1, "OUTPR,ALL,NONE" ' No text output
        Print #1, "SOLV"
        Print #1, "FINISH"
        Print #1, "/EOF"
      Close #1
      sCmd = """" & sExecutable & """ " & sFlags & " -i " & sRunFile & " -o " & sOutFile
      Ft_Exec sCmd, 1                    ' launch Ansys with run_file
      Ft_Import "displacement", "ansys.bin", sRstFile ' import modes from rst_file
output


   End Sub
   '--------------------------------------------------------------------------
   ' CLOSE Custom ANSYS driver
```

```
'--------------------------------------------------------------------------


# Script to compute static displacements sensitivity using ANSYS re-analysis

clear all

# import model (featuring node forces and ANTYPE, STATIC)
input fem format ansys file ANALYSIS22.cdb

# set custom static solver
# set solver ansys_static.bas
set solver 'ANSYS_STATIC_LINEAR.bas'

# define load case (currently needed by static command) and solve
define load 1 "test case"
static

# Parameter and FEM response definition
#response displacement fem 1 node 1 3 dof ux scatter 1
#response displacement fem 1 node 2 4 8 dof uy scatter 1
#response displacement fem 1 node 4207 6619 7215 dof uy scatter 1
input test format uff file TEST07-N2-AC20.unv

define response displacement all dof uy

pair node 4697 7090 7680 8280 with point 1 2 3 4

pair displacement sequential
```

```
extract response
#parameter local type ky element 910032 scatter 100

# ROOT CLAMP INNER 13 (NO USING IT NOW)
#parameter global type E set 13 scatter 10 lower -10 upper 10
# ROOT CLAMP OUTER 14
parameter global type E set 14 scatter 10 lower -10 upper 10
# SPAR 15
parameter global type E set 15 scatter 10 lower -10 upper 10
# SPAR_ROOT 16
parameter global type E set 16 scatter 10 lower -10 upper 10

# sensitivity analysis (using reanalysis with custom solver)

#set sensitivity method reanalysis
#set sensitivity perturbation 1
#sensitivity normalized

# display sensitivity matrix

#matrix sensitivity
```

Appendix J - FEMTOOLS DYNAMIC SCRIPTS

```
# Script to compute modal sensitivity using ANSYS re-analysis

clear all

input fem format ansys file ANALYSIS_MODAL22.cdb

# set dynamic solver
set solver ANSYS
compute mass stiffness
dynamic vector 5 fmin 1

input test format uff file 'TEST02_FixCnt 20150701_UY_REDUCEDPOINTS.UFF'
transform test tx -0.556
transform test tz -0.13
transform test rx -87.9
transform test ty  0.005

pair node all tolerance 0.02

set correlation deviation 50
set correlation displacement 0.7
set correlation dof uy

pair mode all mac 85
```

Appendix K- Experimental Validation 3D Deformation Plots

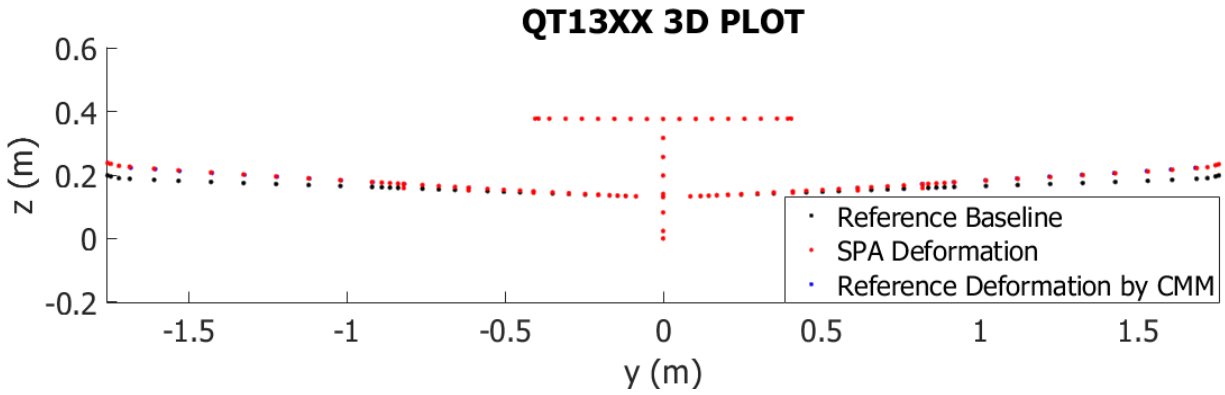

Figure 88: Distributed Load test 01 deformation plot

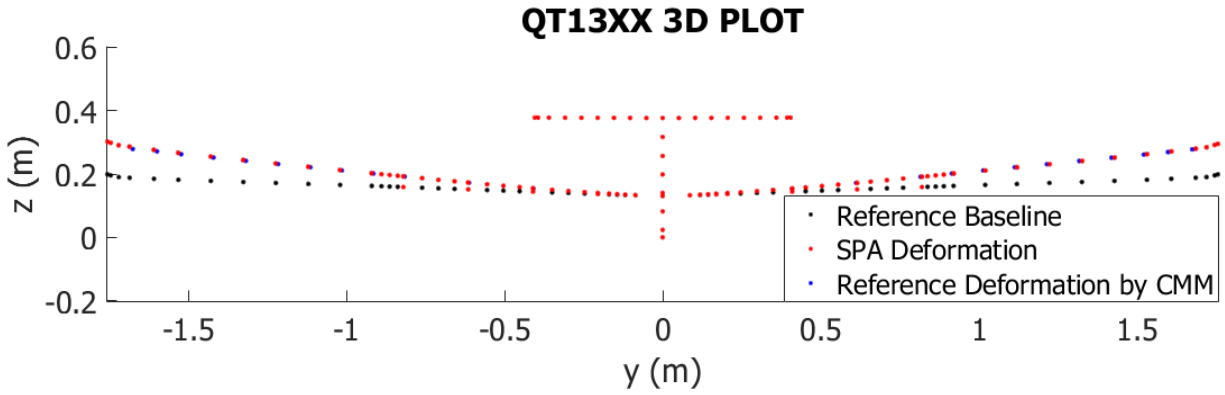

Figure 89: Distributed Load test 02 deformation plot

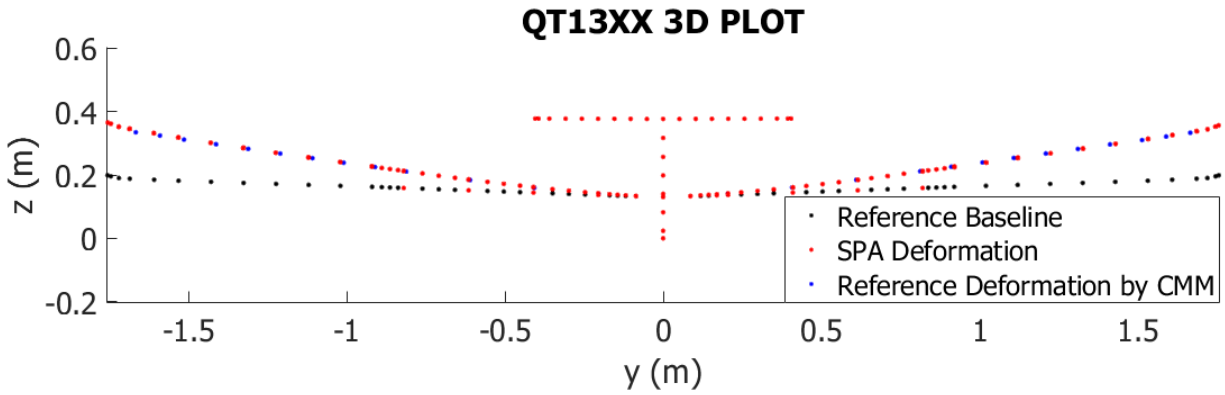

Figure 90: Distributed Load test 03 deformation plot

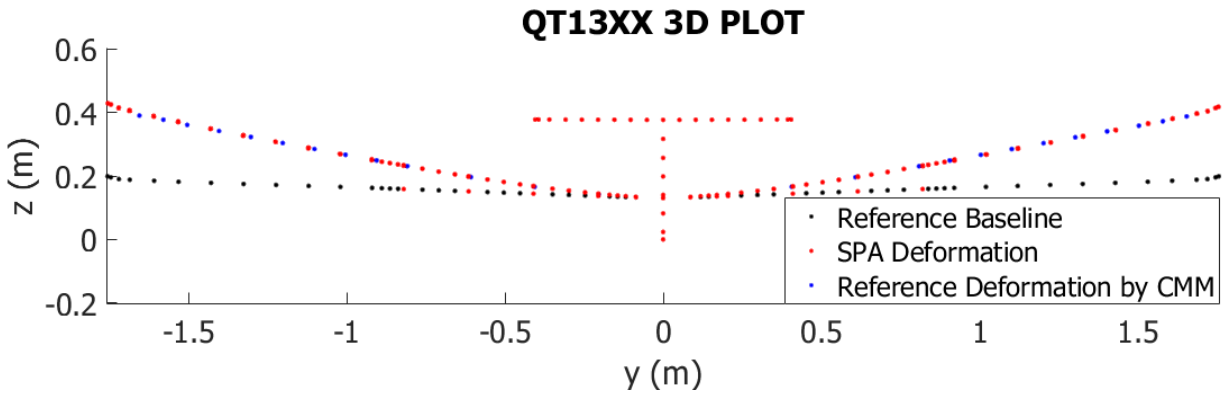

Figure 91: Distributed Load test 04 deformation plot

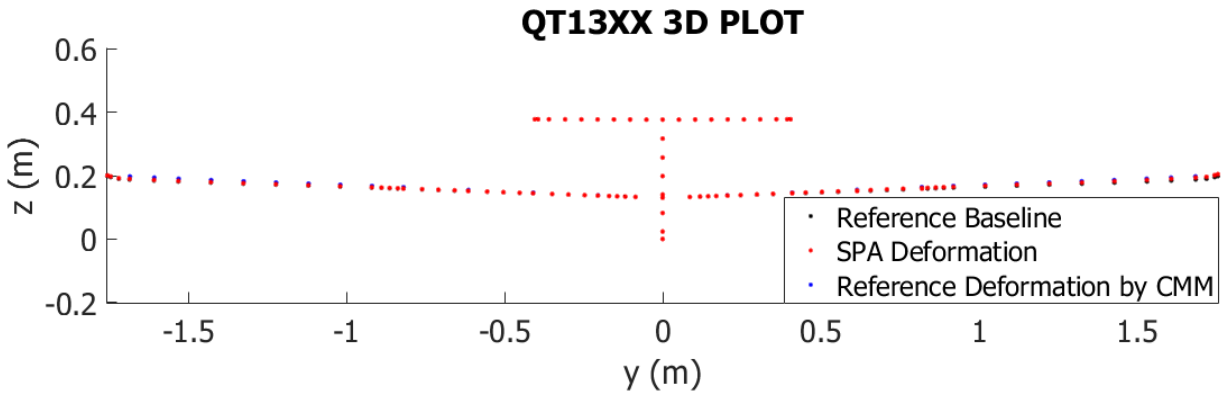

Figure 92: Distributed Load test 06 deformation plot

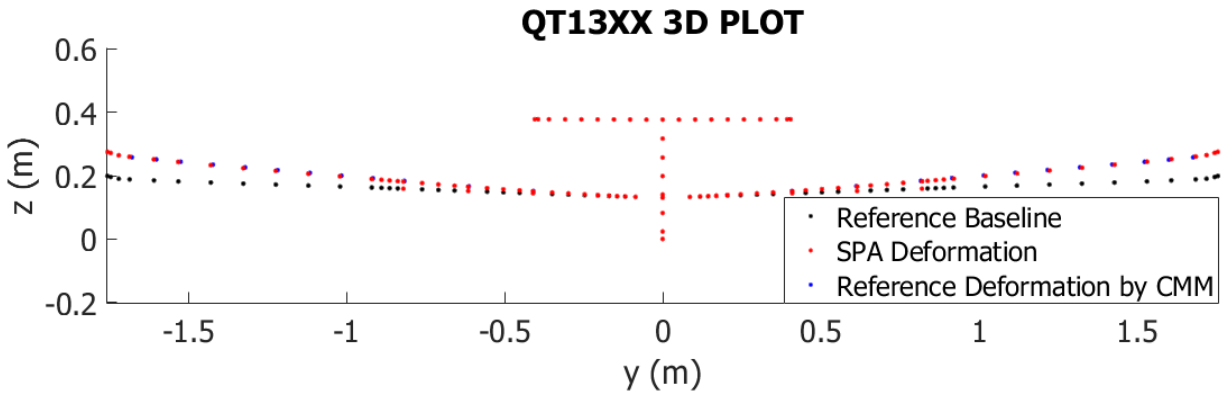

Figure 93: Distributed Load test 07 deformation plot

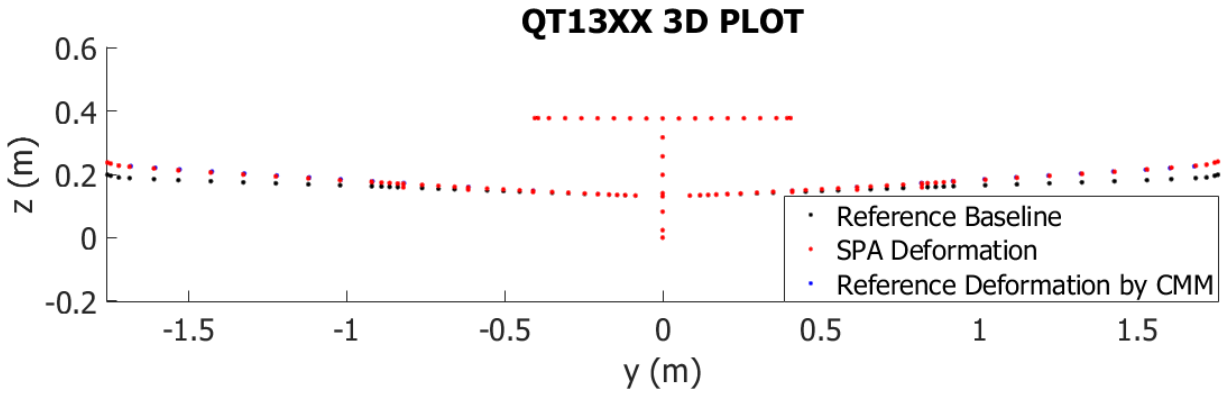

Figure 94: Distributed Load test 08 deformation plot

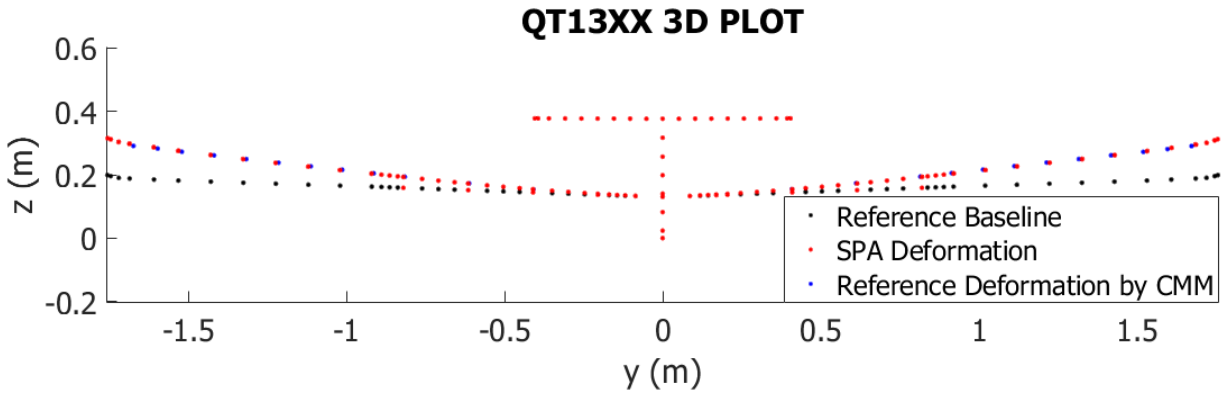

Figure 95: Distributed Load test 09 deformation plot

Appendix L - Experimental Validation Deformation Errors

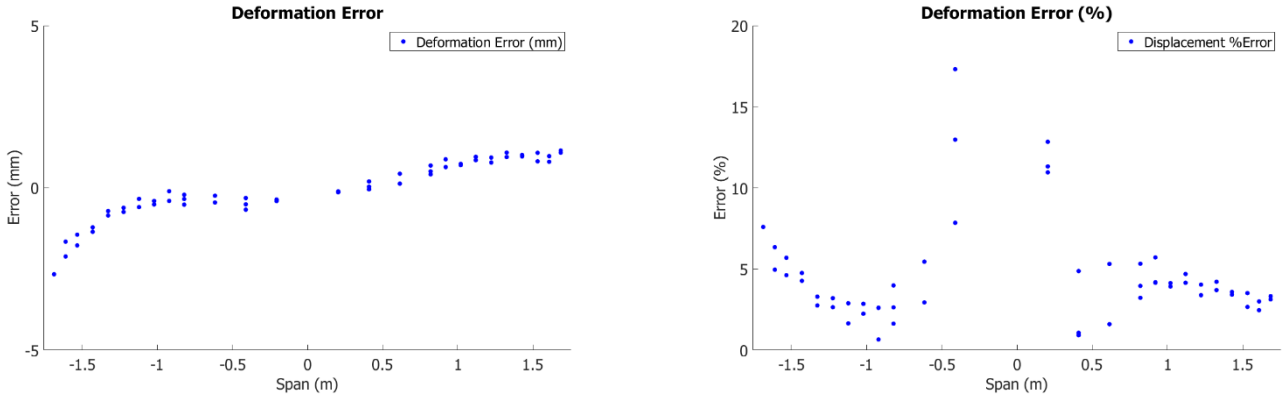

Figure 96: Distributed Load test 01 out-of-plane deformation error for both wing halves.

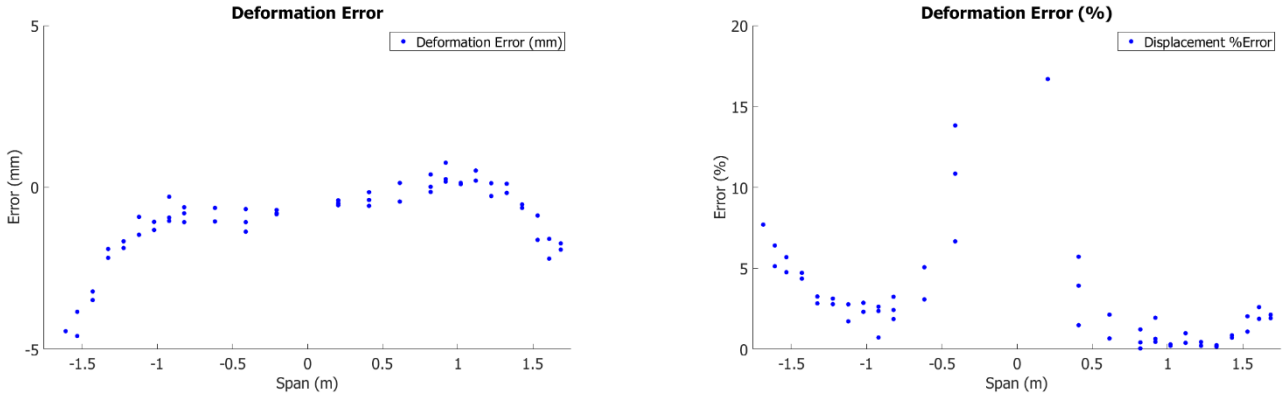

Figure 97: Distributed Load test 02 out-of-plane deformation error for both wing halves.

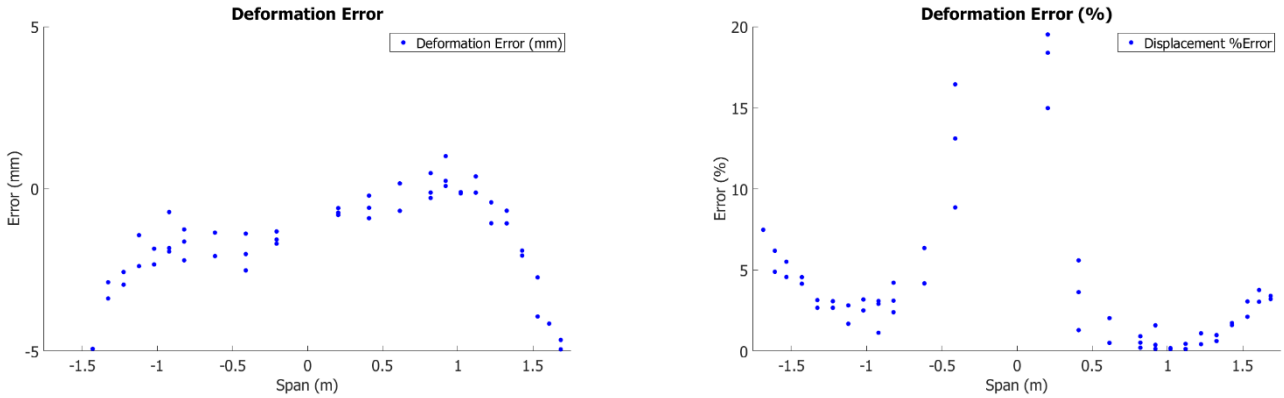

Figure 98: Distributed Load test 03 out-of-plane deformation error for both wing halves.

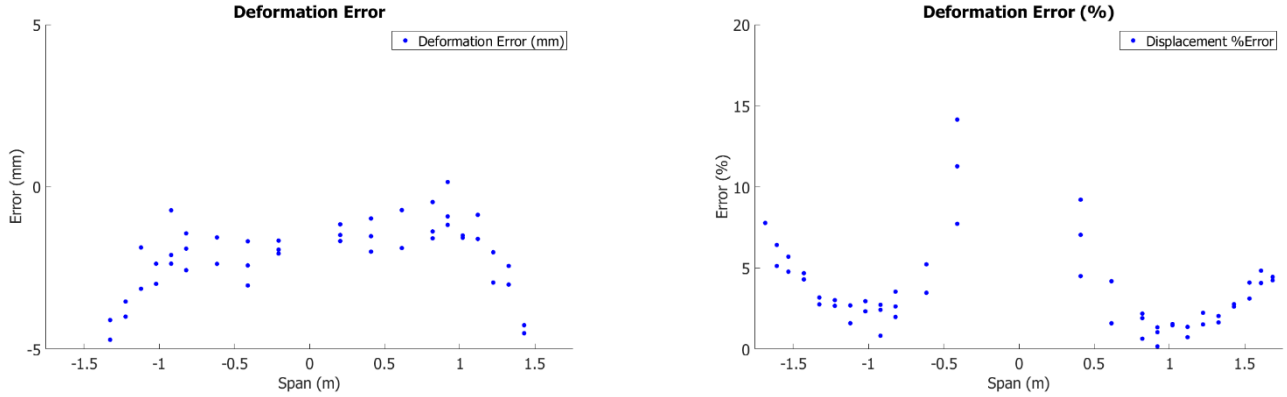

Figure 99: Distributed Load test 04 out-of-plane deformation error for both wing halves.

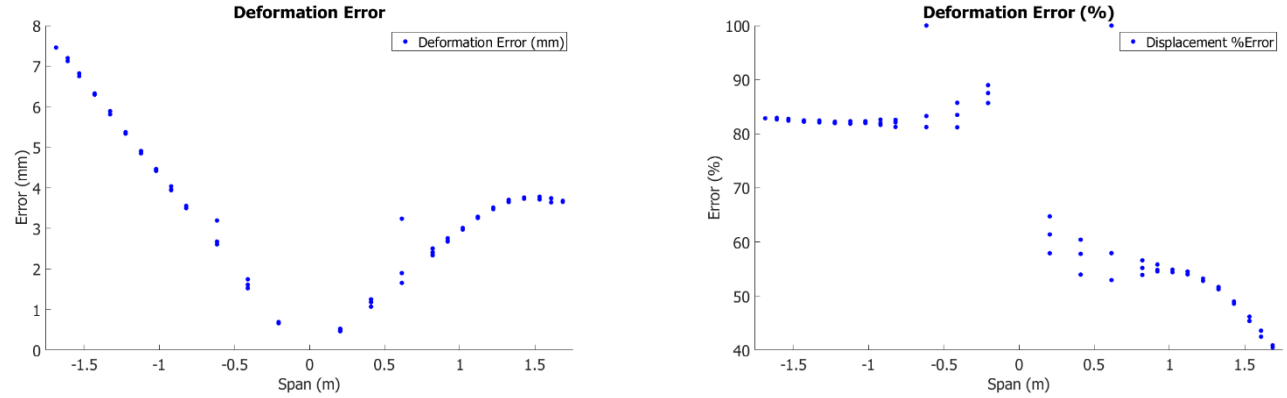

Figure 100: Distributed Load test 06 out-of-plane deformation error for both wing halves.

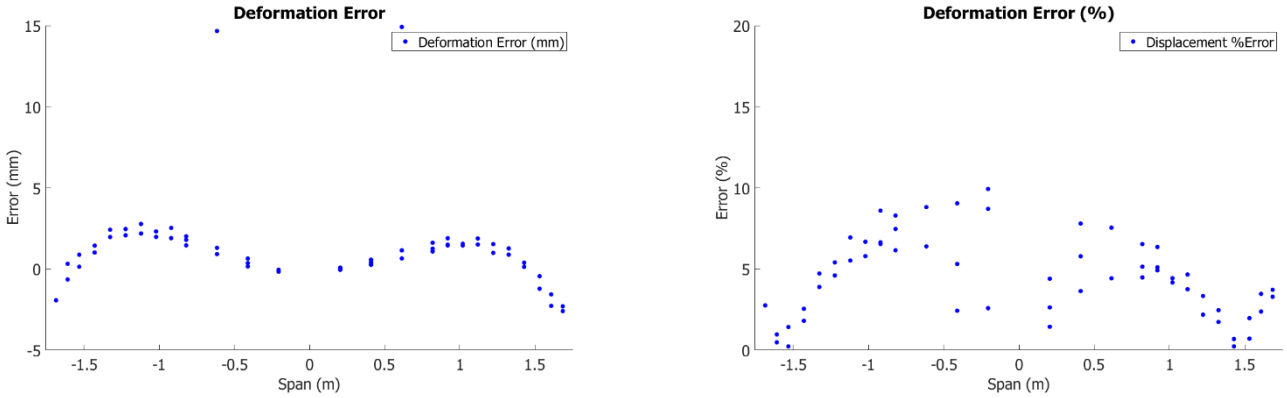

Figure 101: Distributed Load test 07 out-of-plane deformation error for both wing halves.

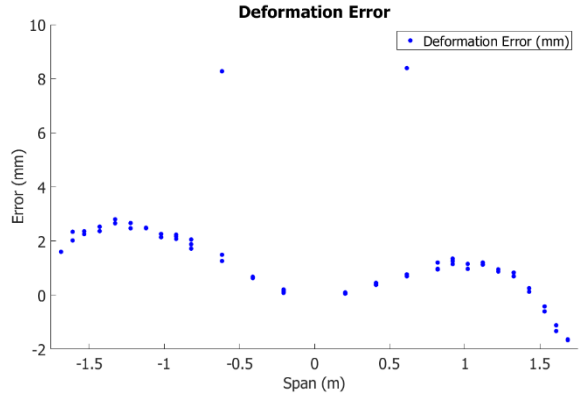

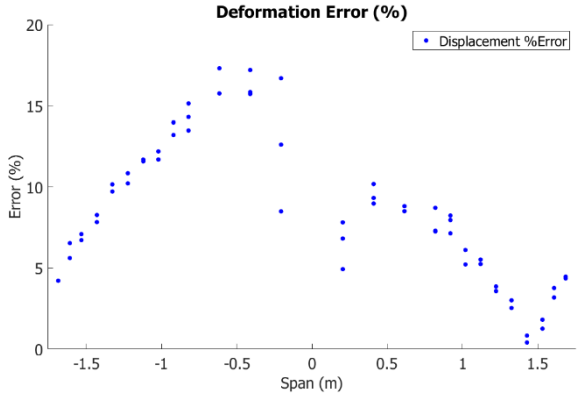

Figure 102: Distributed Load test 08 out-of-plane deformation error for both wing halves.

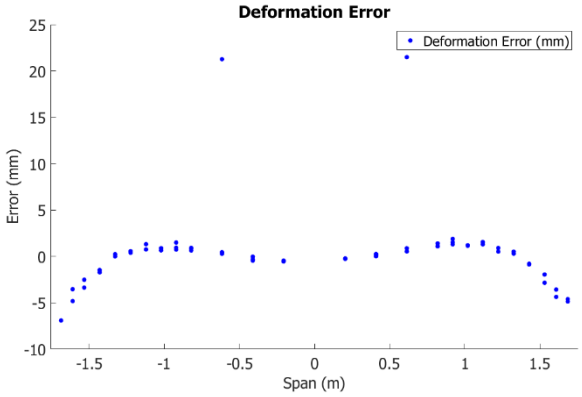

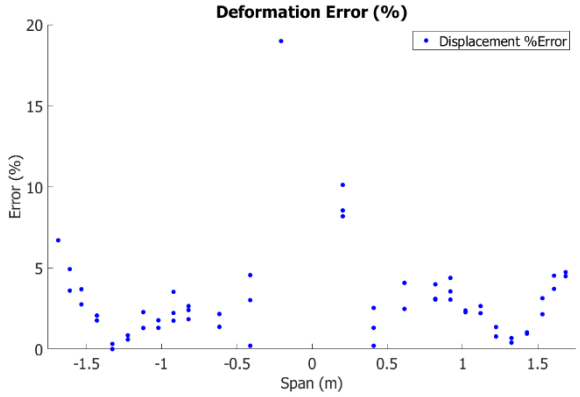

Figure 103: Distributed Load test 09 out-of-plane deformation error for both wing halves.

Appendix M - EXPERIMENTAL VALIDATION TWIST

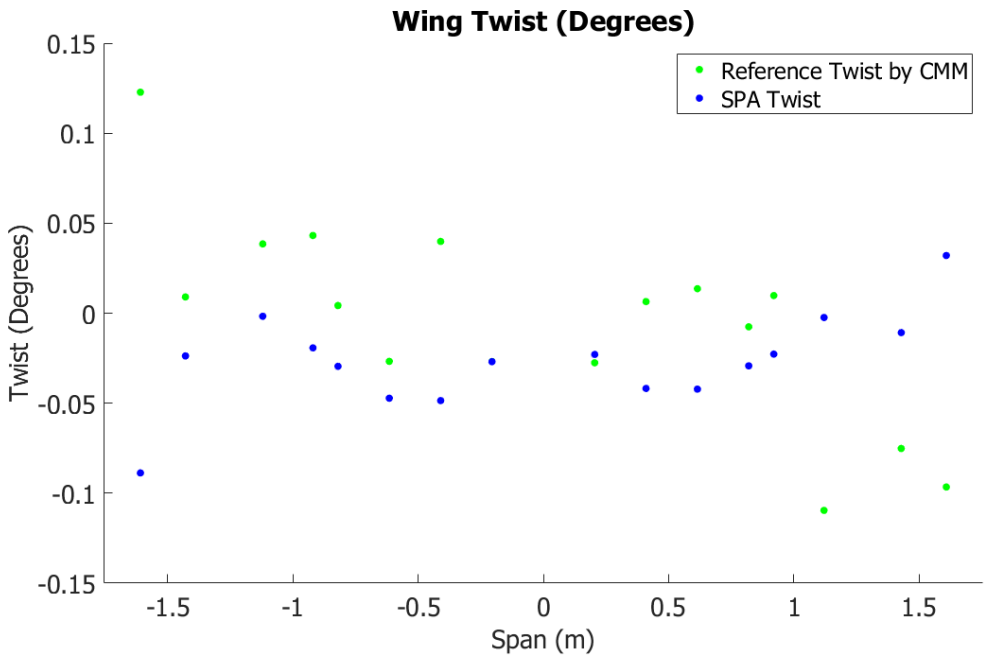

Figure 104: Distributed Load test 01 experimental wing twist.

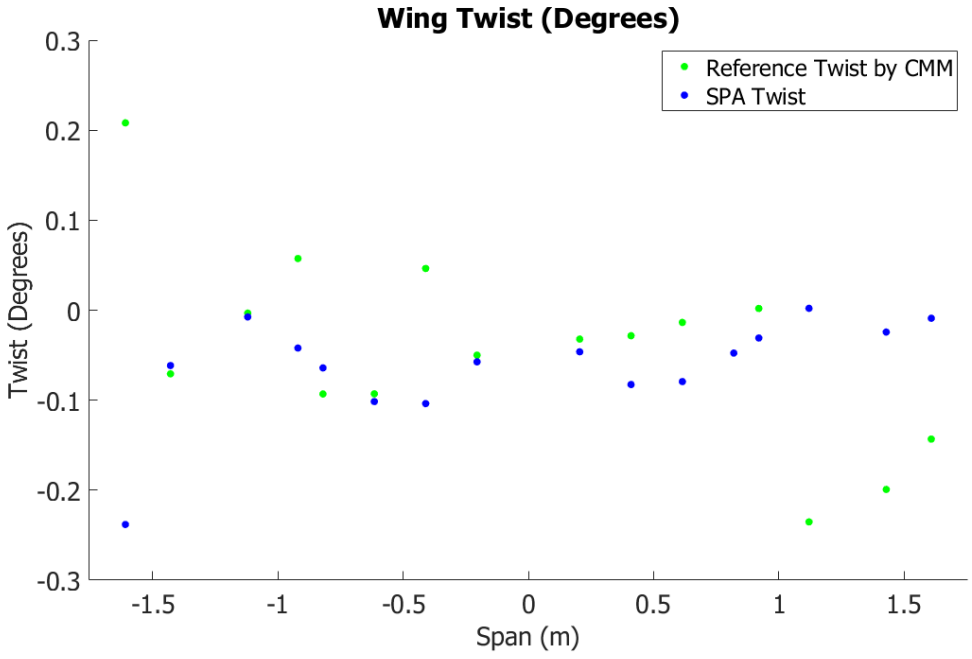

Figure 105: Distributed Load test 02 experimental wing twist.

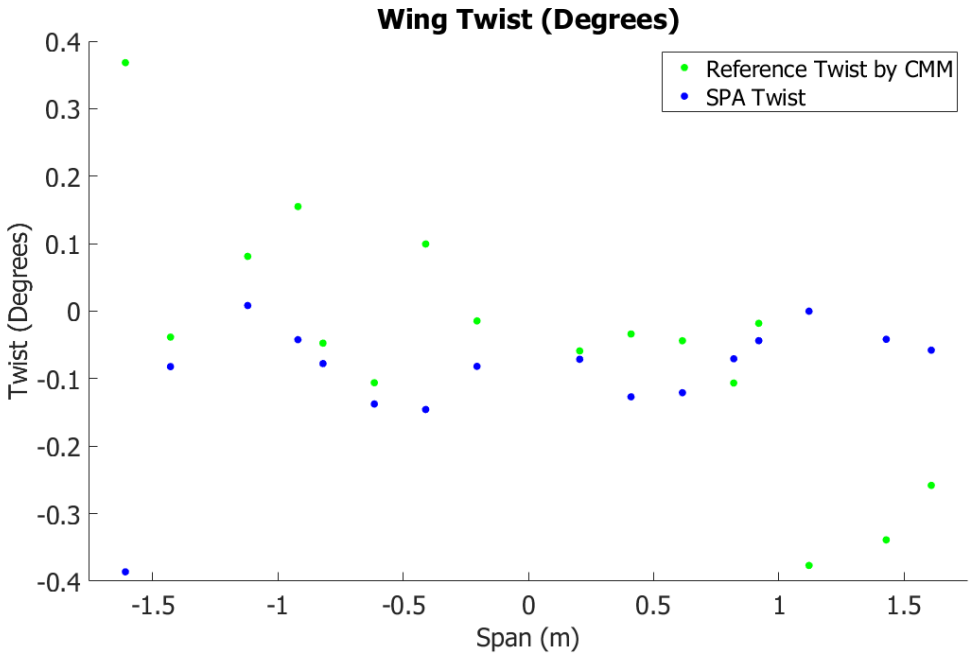

Figure 106: Distributed Load test 03 experimental wing twist.

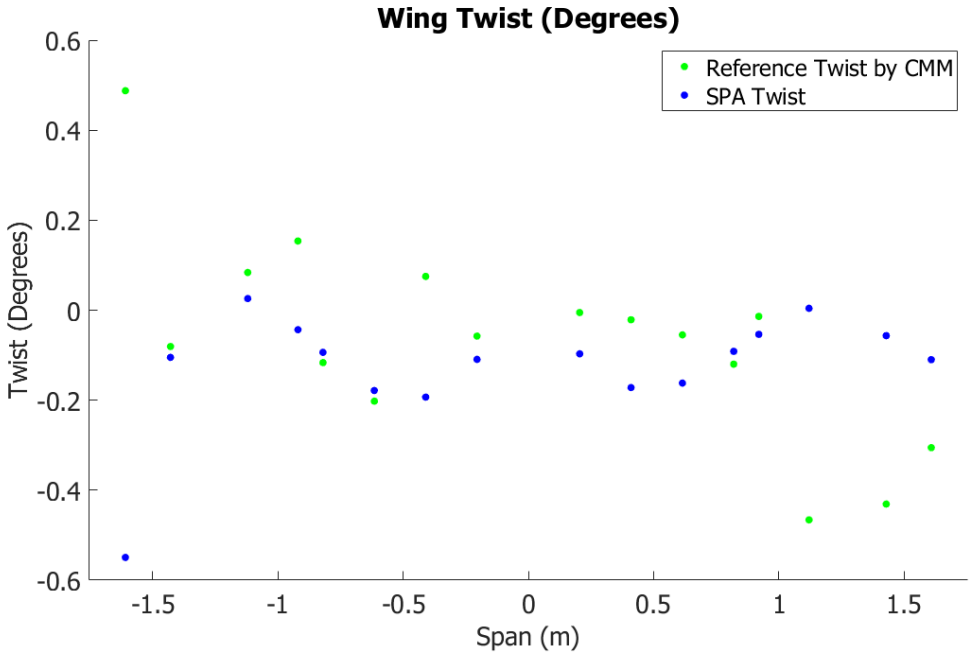

Figure 107: Distributed Load test 04 experimental wing twist.

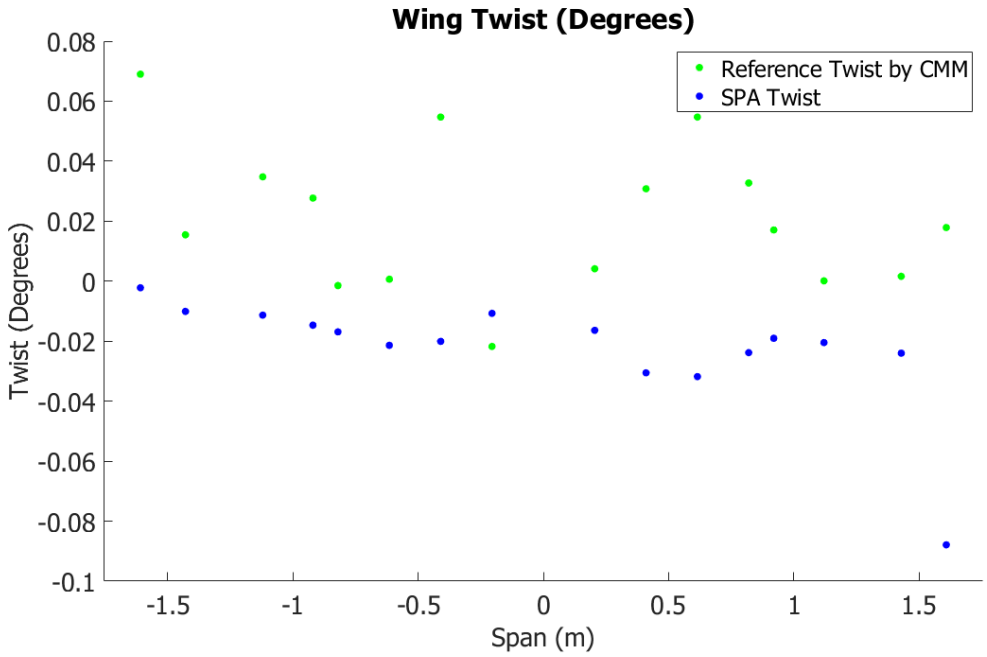

Figure 108: Distributed Load test 06 experimental wing twist.

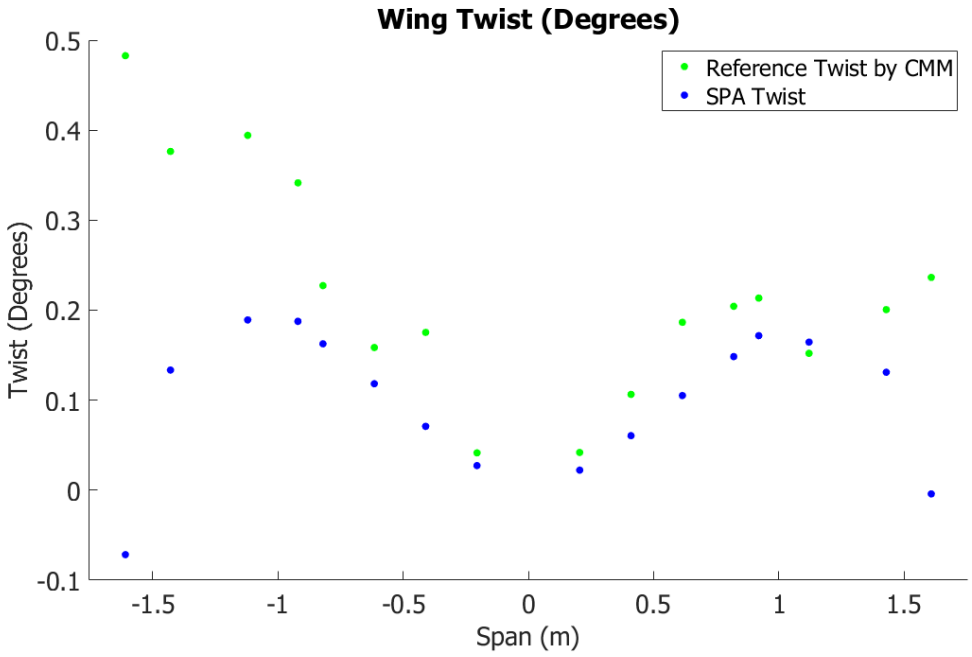

Figure 109: Distributed Load test 07 experimental wing twist.

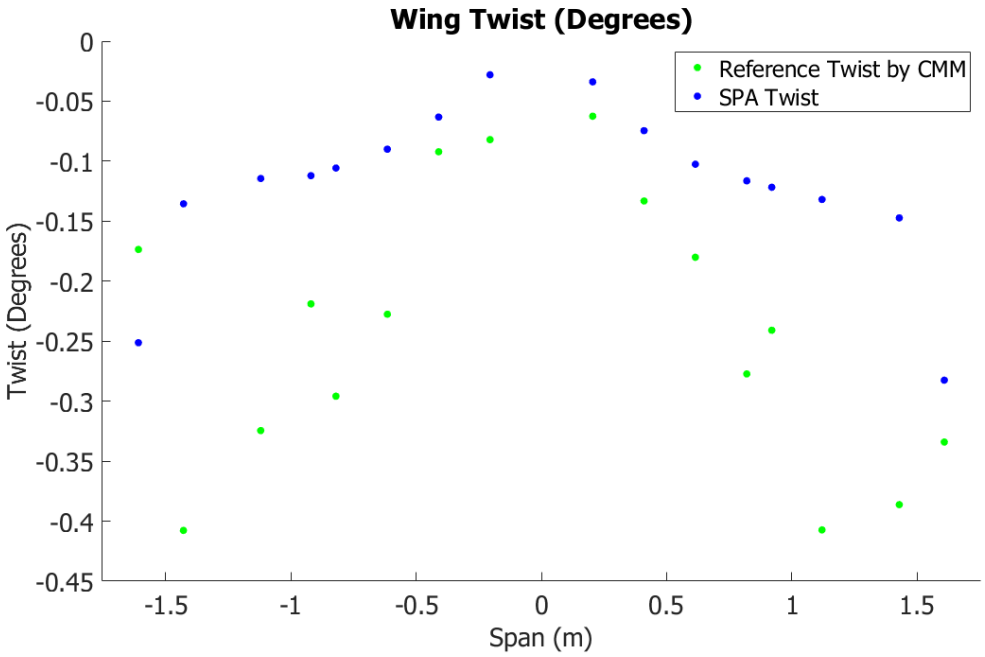

Figure 110: Distributed Load test 08 experimental wing twist.

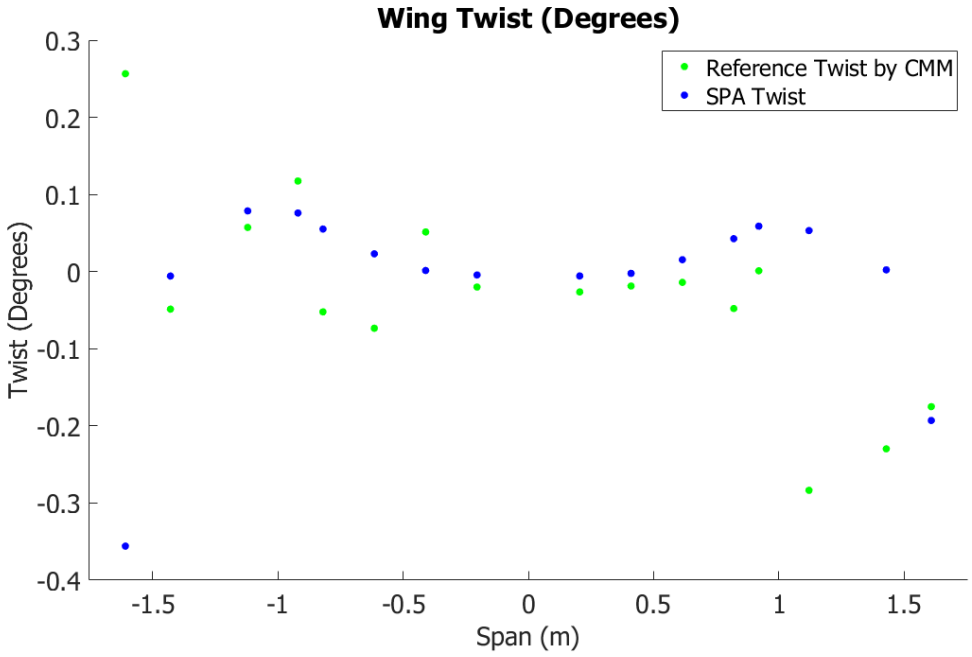

Figure 111: Distributed Load test 09 experimental wing twist.

Appendix N - EXPERIMENTAL VALIDATION TWIST ERRORS

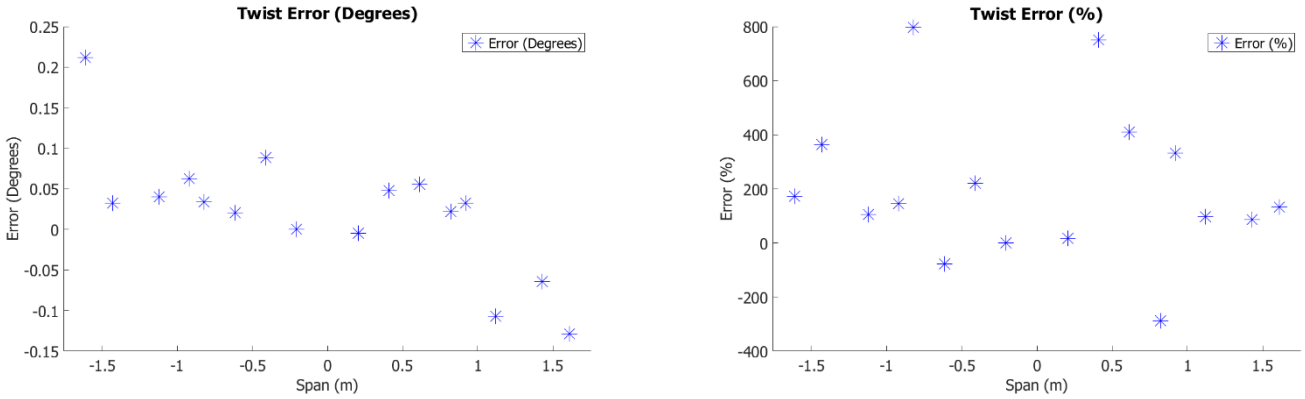

Figure 112: Distributed Load test 01 experimental wing twist errors.

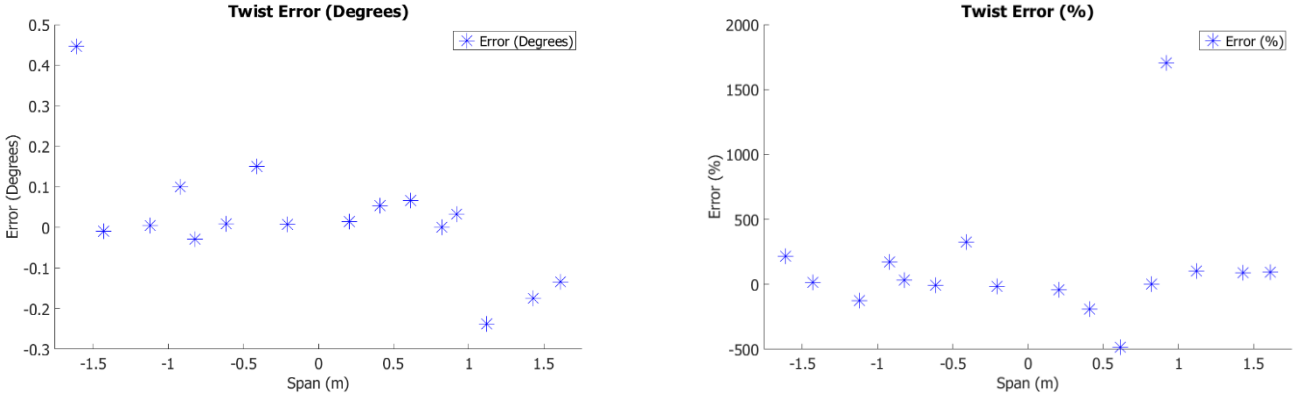

Figure 113: Distributed Load test 02 experimental wing twist errors.

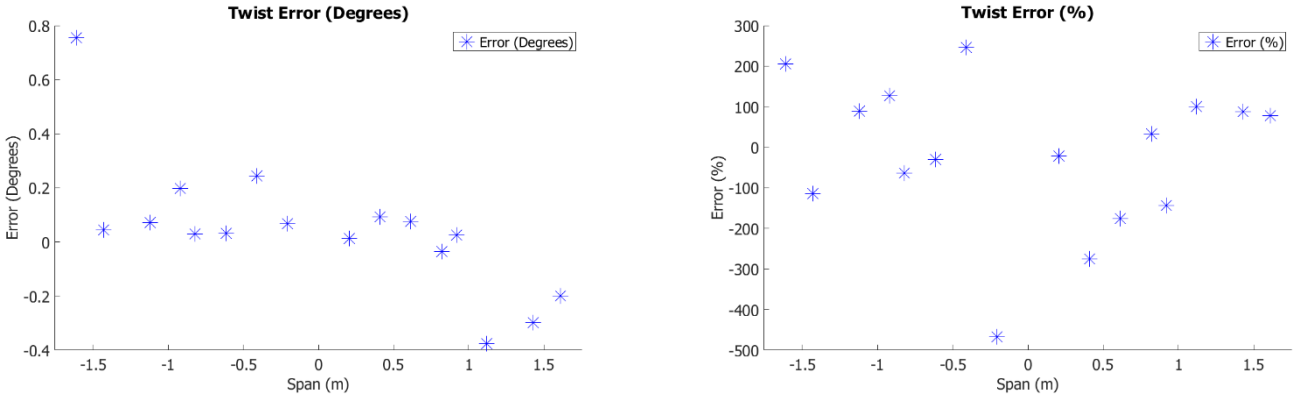

Figure 114: Distributed Load test 03 experimental wing twist errors.

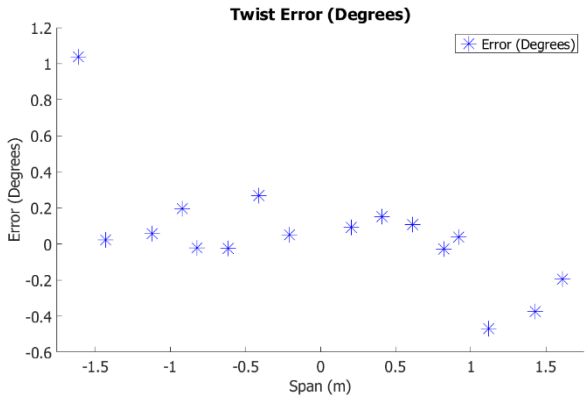

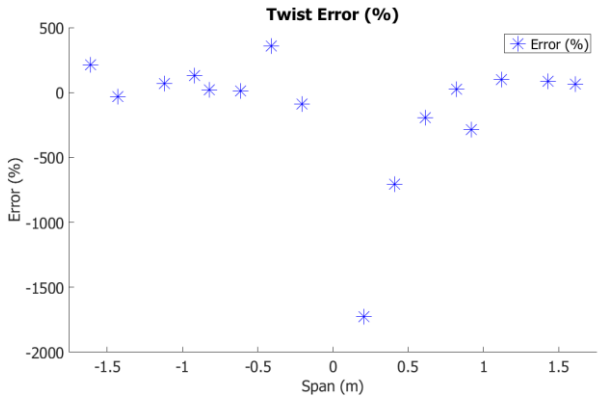

Figure 115: Distributed Load test 04 experimental wing twist errors.

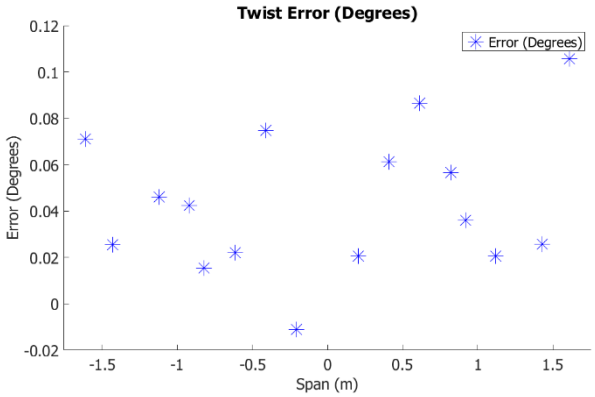

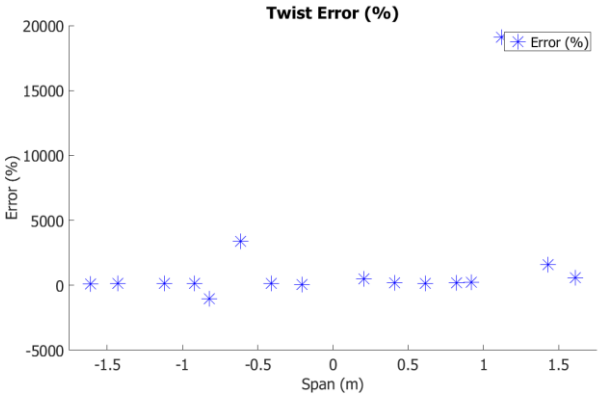

Figure 116: Distributed Load test 06 experimental wing twist errors.

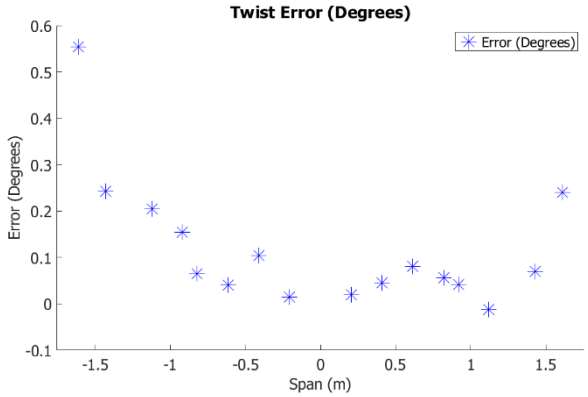

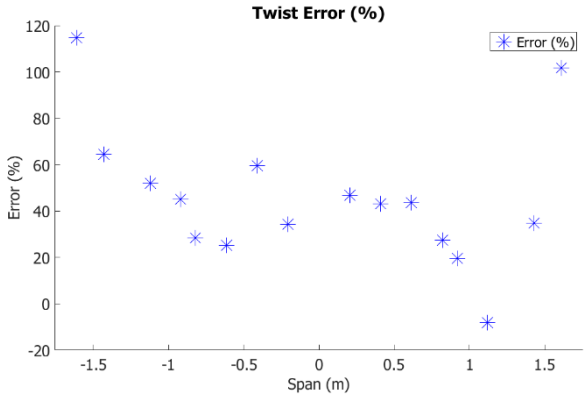

Figure 117: Distributed Load test 07 experimental wing twist errors.

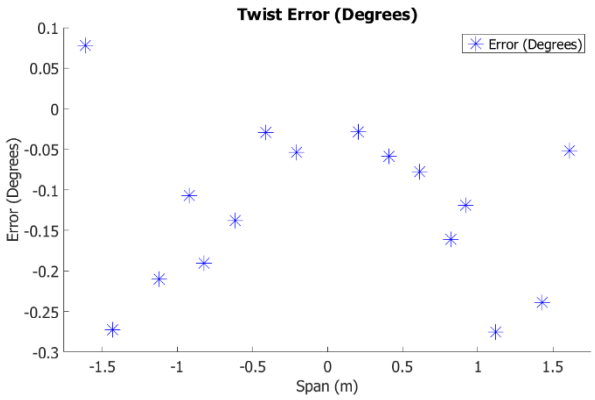

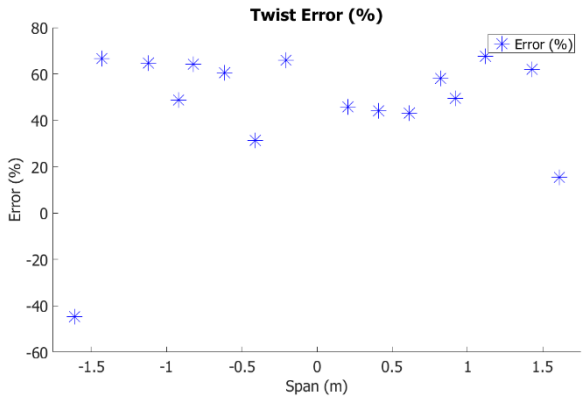

Figure 118: Distributed Load test 08 experimental wing twist errors.

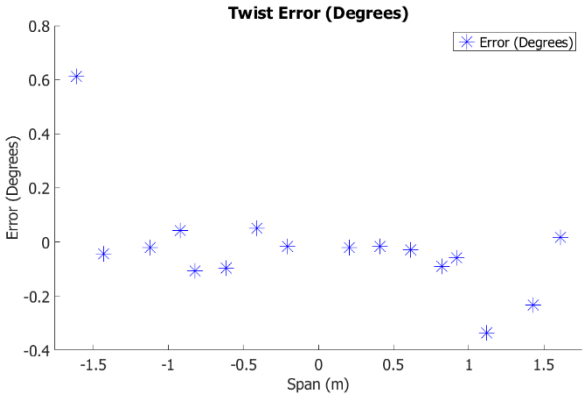

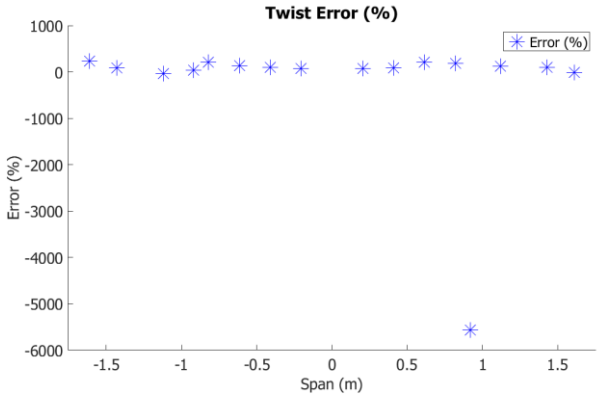

Figure 119: Distributed Load test 09 experimental wing twist errors.

Appendix O - Experimental Validation Strain Modal Least Squares Fits

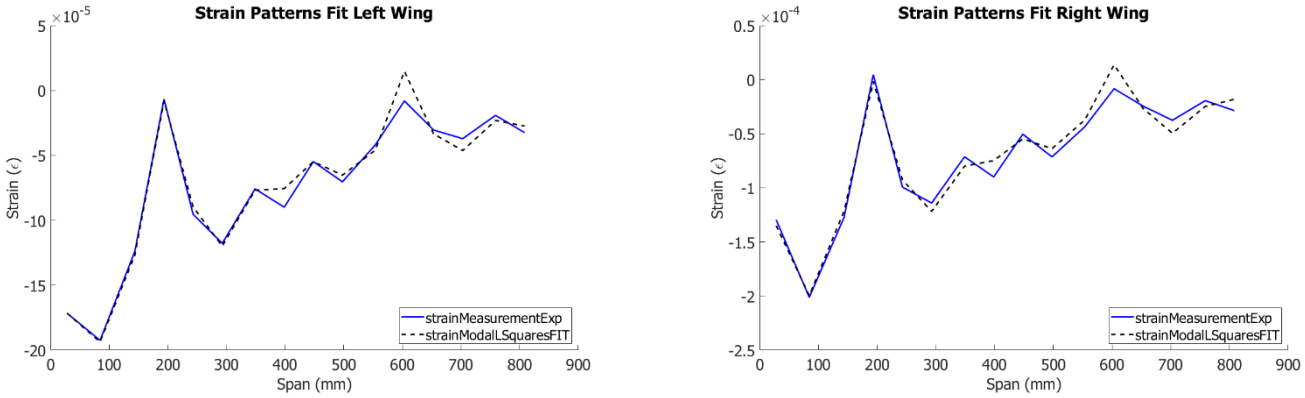

Figure 120: Distributed Load test 01 strain modal fits

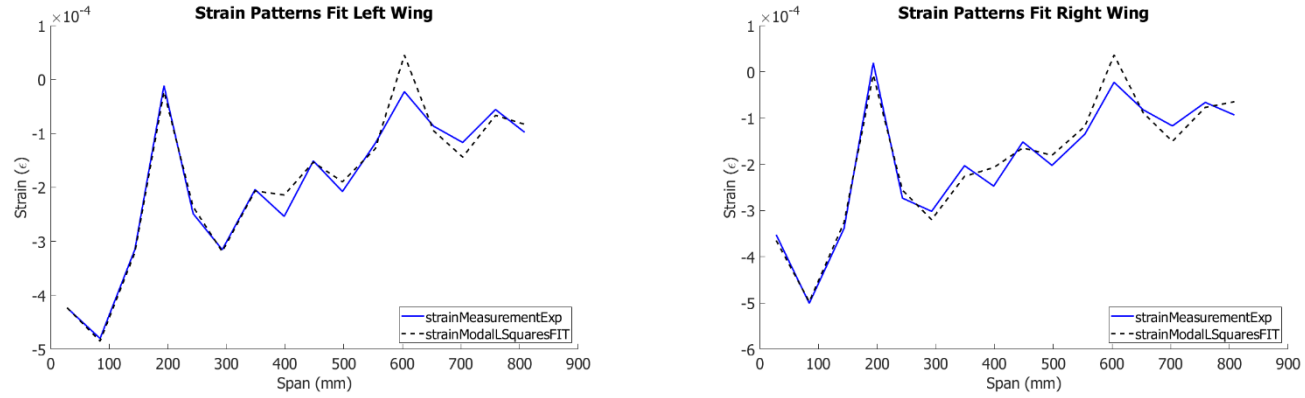

Figure 121: Distributed Load test 02 strain modal fits

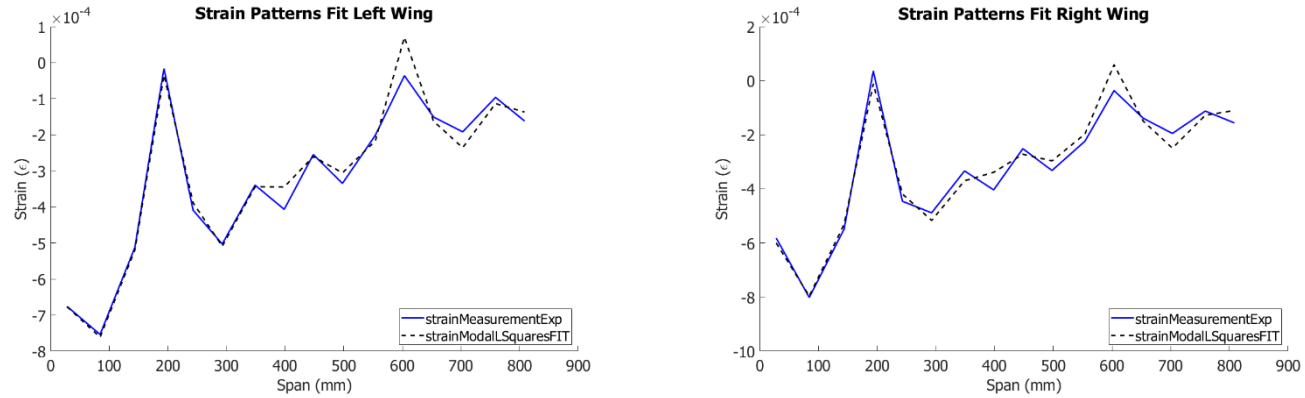

Figure 122: Distributed Load test 03 strain modal fits

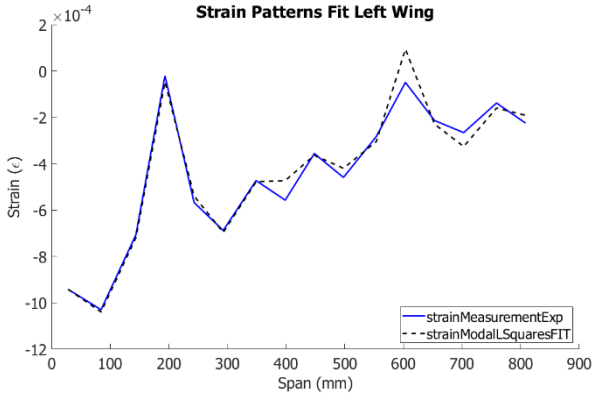

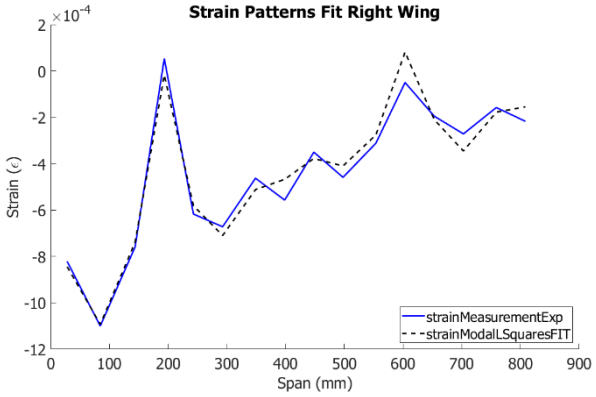

Figure 123: Distributed Load test 04 strain modal fits

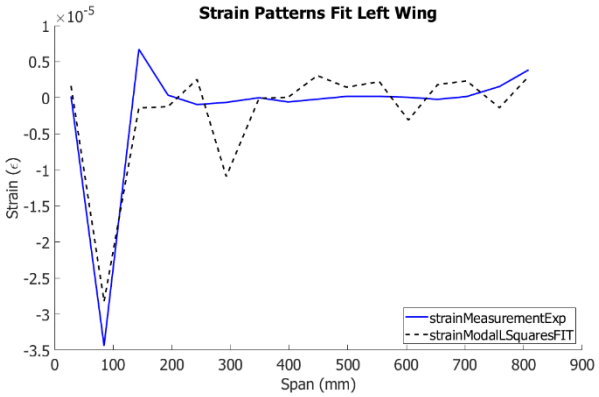

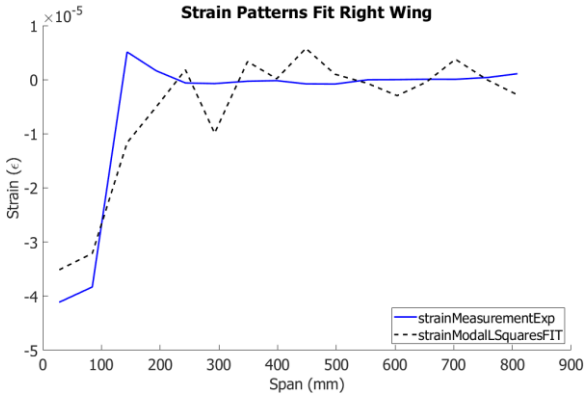

Figure 124: Distributed Load test 06 strain modal fits

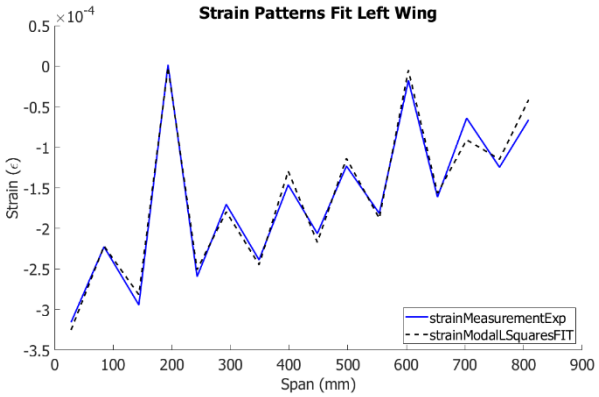

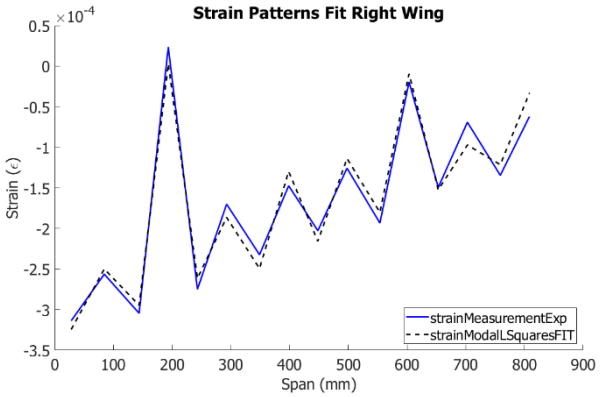

Figure 125: Distributed Load test 07 strain modal fits

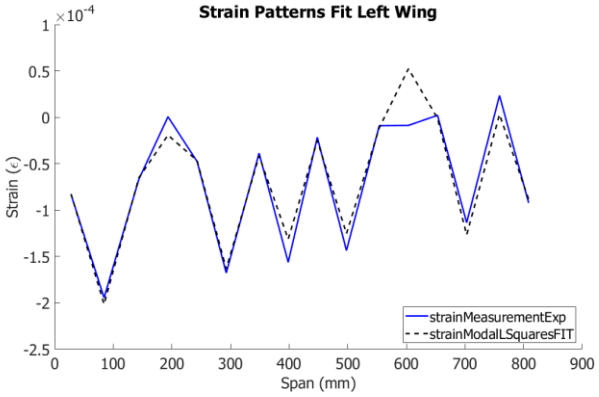

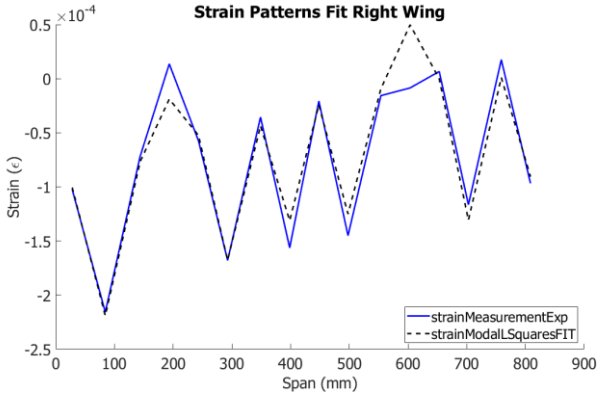

Figure 126: Distributed Load test 08 strain modal fits

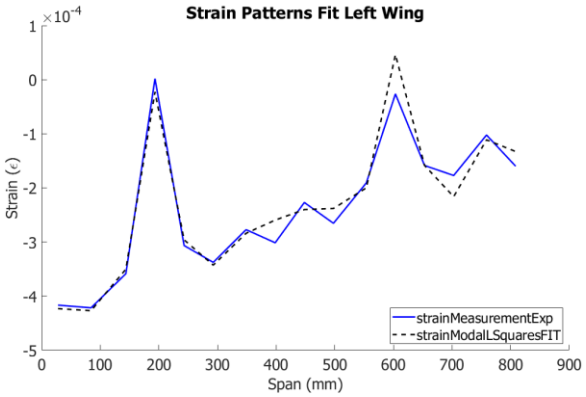

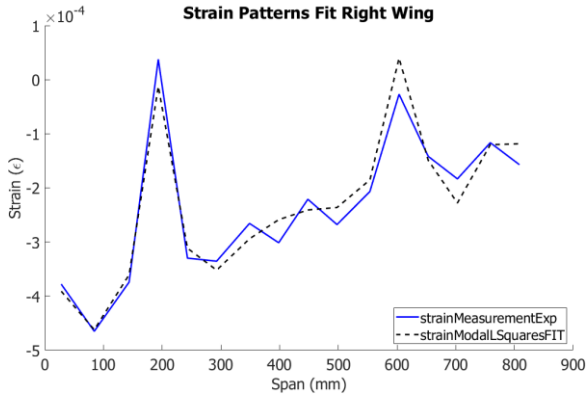

Figure 127: Distributed Load test 09 strain modal fits